2011

Low Noise And Low Repetition Rate Semiconductor-based Mode-locked Lasers

Dimitrios Mandridis
University of Central Florida

STARS Citation

Mandridis, Dimitrios, "Low Noise And Low Repetition Rate Semiconductor-based Mode-locked Lasers" (2011). *Electronic Theses and Dissertations, 2004-2019*. 1867.
https://stars.library.ucf.edu/etd/1867

LOW NOISE AND LOW REPETITION RATE SEMICONDUCTOR-BASED MODE-LOCKED LASERS

by

DIMITRIOS MANDRIDIS
B.A. and M.Sc. National Technical University of Athens 2004
M.Sc. University of Central Florida 2007

A dissertation submitted in partial fulfillment of the requirements
for the degree of Doctor of Philosophy
in the College of Optics and Photonics
at the University of Central Florida
Orlando, Florida

Summer Term
2011

Major Professor: Peter J. Delfyett

ABSTRACT

The topic of this dissertation is the development of low repetition rate and low noise semiconductor-based laser sources with a focus on linearly chirped pulse laser sources. In the past decade chirped optical pulses have found a plethora of applications such as photonic analog-to-digital conversion, optical coherence tomography, laser ranging, etc. This dissertation analyzes the aforementioned applications of linearly chirped pulses and their technical requirements, as well as the performance of previously demonstrated chirped pulse laser sources. Moreover, the focus is shifted to a specific application of the linearly chirped pulses, time-stretched photonic analog-to-digital conversion (TS ADC). The challenges of surpassing the speeds of current electronic converters are discussed, while the need for low noise linearly chirped pulse lasers becomes apparent for the realization of TS ADC.

The experimental research addresses the topic of low noise chirped pulse generation in three distinct ways. First, a chirped pulse (Theta) laser with an intra-cavity Fabry-Pérot etalon and a long-term referencing mechanism is developed that results in the reduction of the pulse-to-pulse energy noise. Noise suppression of >15 times is demonstrated. Moreover, an optical frequency comb with spacing equal to the repetition rate (≈100 MHz) is generated using the etalon, resulting in the first reported demonstration of a system operating in the sub-GHz regime based on semiconductor gain. The path for the development of the Theta laser was laid by the precise characterization of the etalon used in this laser cavity design. A narrow linewidth laser is used in conjunction with an acousto-optic modulator externally swept for measuring the etalon's free spectral range with a sub-Hz precision, or 10 parts per billion. Furthermore, the measurement of the etalon long-term drift and birefringence lead to the development of a modified intra-cavity Hänsch-Couillaud locking mechanism for the Theta laser. Moreover, an external feed-forward system was demonstrated that aimed at increasing the temporal/spectral uniformity of the optical pulses. A complete characterization of the system is demonstrated.

On a different series of experiments, the pulses emitted by an ultra-low noise but high repetition rate mode-locked laser were demultiplexed resulting in a low repetition rate pulse train. Experimental investigation of the noise properties of the laser proved that they are preserved during the demultiplexing process. The noise of the electrical gate used in this experiment is also investigated which led into the development of a more profound understanding of the electrical noise of periodical pulses and a mechanism of measuring their noise.

The appendices in this dissertation provide additional material used for the realization of the main research focus of the dissertation. Measurements of the group delay of the etalon used in the Theta laser are presented in order to demonstrate the limiting factors for the development of this cavity design. The description of a balancing routine is presented, that was used for expanding the dynamic range of intra-cavity active variable delay. At last, the appendix presents the calculations regarding the contribution of various parameters in the limitations of analog-to-digital conversion.

This work is dedicated to my family for all the support.

& ι

ACKNOWLEDGEMENTS

I would like to thank my advisor, Prof. Peter Delfyett who guided me towards my PhD thesis. I would also like to especially thank my mentors from the Ultrafast Photonics group, Dr. Franklyn Quinlan, Dr. Sarper Ozharar, Dr. Shinwook Lee and Prof. Sangyun Gee. Also, I have to thank my friends and collaborators from the group that contributed with their help, ideas and patience to my work; Ibrahim Ozdur, Charles Williams, Josue Davila-Rodriguez, Marcus Bagnell and Anthony Klee.

TABLE OF CONTENTS

LIST OF FIGURES

LIST OF ACRONYMS/ABBREVIATIONS

ADC	Analog-to-Digital Conversion
AM	Amplitude Modulation
ASE	Amplified Spontaneous Emission
CFBG	Chirped Fiber Bragg Grating
CFF	Cavity Fundamental Frequency
CPA	Chirped Pulse Amplification
CW	Continuous Wave
DAC	Digital-to-Analog Converter
dB	Decibel
dBc	Decibel relative to the carrier
dBm	Decibel relative to 1 mW
DCF	Dispersion Compensating Fiber
DFB	Distributed Feedback
DFT	Discrete Fourier Transform
EDFA	Erbium Doped Fiber Amplifier

ENOB	Effective Number of Bits
$\mathscr{F}$	Finesse
FC-FDML	Frequency Comb Fourier Domain MLL
FDML	Fourier Domain MLL
FOPO	Fiber Optical Parametric Amplifier
FSR	Free Spectral Range
HC	Hänsch-Couillaud
IM	Intensity Modulator
LNO	Low Noise Oscillator
MLL	Mode-Locked Laser
MPN	Mode Partition Noise
OCT	Optical Coherence Tomography
OFDR	Optical Frequency Domain Reflectometry
OPS	Optical Fiber Shifter
PDH	Pound-Drever-Hall
PG	Pattern Generator

PM	Phase Modulation
PSD	Power Spectral Density
RF	Radio Frequency
RMS	Root Mean Square
RSOD	Rapid Scanning Optical Delay
SCOWA	Slab-Coupled Optical Waveguide Amplifier
SMF	Single Mode Fiber (usually SMF-28e)
SNR	Signal-to-Noise Ratio
SSB	Single Sideband
TD-OCT	Time-domain Optical Coherence Tomography
TS	Time Stretch
t-λ	Time-to-Wavelength
WDM	Wavelength Division Multiplexing
WPE	Wall-Plug Efficiency
X-CPA	eXtreme Chirped Pulse Amplification

CHAPTER 1: SWEPT PULSE GENERATION AND APPLICATIONS

1.1 Introduction to Frequency Swept Pulses

As introduced by Kolner [1], a duality exists between the paraxial Gaussian optics equations and the dispersion of narrow-band pulses. This implies that quadratic phase is the temporal analog of a thin lens in space, which effectively introduces spatial quadratic phase. Accordingly, time lenses can be implemented by using the interplay of dispersion and diffraction.

The equations described in [1] present an in-depth investigation of the time lens effect. However, in the limit of large linear dispersion (quadratic phase) the equations are simplified and linear time-to-wavelength (t-λ) mapping is observed. t-λ mapping results into a temporal intensity profile of the stretched pulses that follows the pulse spectral intensity profile. In the t-λ mapping regime, stretching (compressing) using linear dispersion elements results into the magnification (shrinking) of temporal signals encoded on the chirped pulses.

In the past decade, multiple applications have emerged that make use of the time-lens or t-λ mapping, as will be discussed in this section. For most of the applications of t-λ, discussed in this work, dispersion is provided by long lengths of single mode fiber (SMF), while dispersion compensating fiber (DCF) is used for providing complimentary dispersion. However, some experimental demonstrations are based on chirped fiber Bragg grating (CFBG) technology. The main advantage of using CFBGs is that due to their artificially engineered dispersion properties, large differential spectral delay can be attained in short travel length. However, the CFBGs performance is somewhat limited due to fabrication imperfections, as discussed in the Appendix.

The repetition rate range for t-λ applications is 10-100 MHz, which is selected for two reasons. Since the nominal spectral bandwidth of laser sources lies in the 5-50 nm regime, linear t-λ mapping is attained for stretched pulses in the nanosecond range. Repetition rates in the order of 10 GHz, which correspond to laser periods of 100 ps, are not sufficiently long for the linear t-λ mapping to take effect. Moreover, most of the chirped-pulse applications use the pulses as a carrier onto which information is encoded. Multiple information bins are recorded within each chirped pulse and the information is retrieved using real time data acquisition. Since modern oscilloscopes operate at the few GHz bandwidth regime, 10^2-10^3 information bins per pulse correspond to pulse repetition rates of 10-100 MHz.

Pulsed laser sources with repetition rates on the order of 100 MHz are common, since they are easily attained by meter-long laser resonators. Solid state or fiber gain media are usually found on meter-long lasers. On the other hand, semiconductor-based lasers tend to operate at the multi-GHz repetition rates, corresponding to millimeter-long resonators. Short cavities and fast repetition rates from semiconductor gain is a consequence of the electron-hole pair recombination lifetimes, which are in the nanosecond range [2]. While using solid state and fiber gain media to address the 100 MHz regime of laser repetition rates is advantageous, semiconductor media can be preferred for some applications due to their properties.

Semiconductor based lasers have a small footprint, are rugged, temperature stable, power efficient, and inexpensive, when massively produced. However, conventional linear or ring cavity designs cannot be used in conjunction with semiconductor gain media in the 100 MHz repetition rate regime, due to their fast carrier recombination lifetime. This dissertation describes the work conducted towards the development of low repetition rate and low noise semiconductor-based lasers with chirped pulses.

As an introduction, some systems that either use or can benefit from uniform-intensity linearly-chirped optical pulses at 100 MHz are discussed in the following section. Chapter 1 contains a review of applications for extremely chirped pulses and a literature review on the generation of chirped pulses.

Chapter 2 describes in detail one of the most appealing applications of linearly chirped pulses; a specific implementation of photonic-assisted analog-to-digital conversion technique. The benefits of linearly chirped, time filling optical pulses are theoretically analyzed.

Chapter 3 contains the student’s experimental work. The work focuses on three distinct approaches for the generation of the low-noise and low repetition rate semiconductor-based laser sources.

1.2 Frequency Chirped Pulse Applications

1.2.1 Serial time-encoded amplified microscope

A recent application of temporally stretched time-filling uniform intensity pulses is the serial time-encoded amplified microscope (STEAM) [3]. This technique aims at surpassing the speed of CCD or CMOS array detectors, commonly used in imaging, that are limited by the charge extraction times to frame rates in the order of <100 kHz.

In STEAM, the linearly chirped pulses are spatially dispersed in a two dimensional array, resulting in a 2-D matrix of wavelength components that act as the pixels of the imaging system. The effect of the t-λ mapping is used in the conversion of the spectrally encoded image to serialized temporal image, as seen in Figure 1.1. A single "pixel" photodetector is used as a serialized detector in conjunction with a computer algorithm that reconstructs the spectrally encoded image. The repetition rate of the pulsed laser defines the frame rate of the imager. A demonstrated system with a ~6 MHz frame rate showed an improvement over the commonly used detectors of 1,000. Since the total number of frames acquired depends on the memory of the real time oscilloscope used, faster repetition rates will increase the frame rate of movies captured in the same total times. An extensive analysis of the operation parameters and limitations for the STEAM is found in [4].

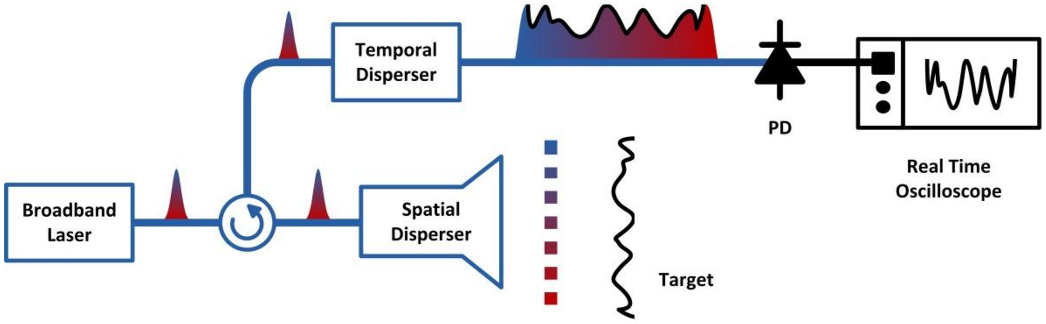

Figure 1.1: Schematic of 1-D serial time-encoded amplified microscope. Adapted from [3].

1.2.2 Time Lens Processing and MW signal analyzer

Saperstein et al. have demonstrated a microwave signal analyzer based on the time lens concept [5]. In this scheme, t-λ mapping from an ultra-fast mode-locked laser (MLL) is attained using long SMF, while a microwave signal is subsequently imposed on the chirped pulses. The pulses are recompressed using the complimentary dispersion of a DCF to result in a reverse Fresnel transformation of the microwave signal. The frequency of the signal can be mathematically extracted using this system. This technique can benefit from X-CPA combined with advanced CFBG technology [6].

1.2.3 Frequency domain reflectometry

Optical coherence tomography (OCT) is a non-destructive testing technique that can be applied to in-vivo testing of sub-surface of biological tissue. OCT measures the depth-varying reflectivity of the sample. In the simplest embodiment of OCT, time-domain OCT (TD-OCT), a low coherence interferometric setup is used, where the reference arm of the interferometer is scanned [7, 8]. This variation of OCT is relatively slow, with speeds in the order of 1 kHz for a single axial scan due to the sweeping speed of system mechanical components.

Instead of having a swept temporal delay, optical frequency domain reflectometry (OFDR) uses a frequency swept optical source [9, 10]. A schematic of a typical OFDR system is shown in Figure 1.2. A frequency chirped source is used in a fiberized interferometer implementation with a fixed reference path. A dual-balanced photodetector is used to suppress background and laser noise. In OFDR, no moving mechanical parts are used and the depth scanning is effectively performed by the optical frequency sweep. The image is extracted by performing a discrete Fourier transform (DFT) on the acquired signal. Unbound from the inertia of moving parts, OFDR can attain high speed axial scans in the tens of kHz range. 3-D imaging has been demonstrated in 0.28 s [11], where a 256x128x256 pixel volume was recorded. Depths in the order of 15 mm with resolution of ~20 μm have been demonstrated [10].

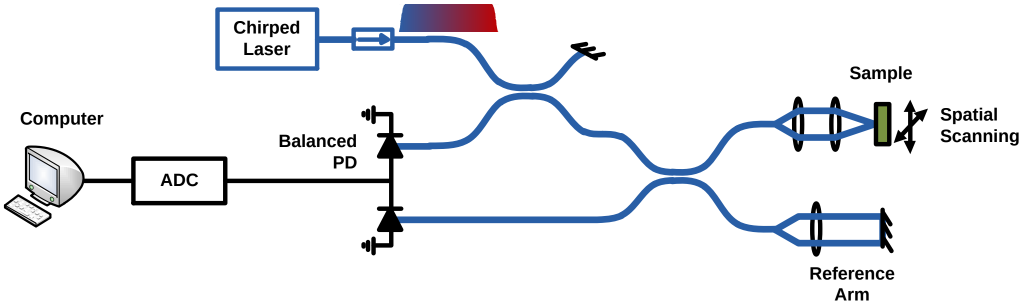

Figure 1.2: Schematic of OFDR OCT. ADC, analog-to-digital converter; PD, photodetector. Adapted from [9, 10].

Due to the Fourier domain properties of OFDR, the defining parameters for this technique are the optical frequency sweep bandwidth, which defines spatial resolution, the instantaneous coherence length (or linewidth), which affects the depth dynamic range, and the sweep rate, which defines the frame rate. In general, high power, increased sweep rate, broad bandwidth, and short instantaneous linewidth sources are desired. The swept laser sources used in OFDR, as well as in other chirped pulse applications, are discussed in section 1.3, while a novel laser architecture that addresses most of the OFDR challenges is presented in section 3.2

1.2.4 Photonic-Assisted Time-Stretched ADC

Another application that has been demonstrated in the last ten years is an implementation of photonic ADC. Since developing a laser source suitable for this technique has been a major goal of the student’s work, the topic of ADC and specifically photonic-assisted time-stretched ADC is discussed in detail in Chapter 2.

1.3 Swept Pulse Generation

1.3.1 Dispersed ultrafast laser pulses

The most straightforward method for generating frequency swept optical pulses is by dispersing the output of ultra-short pulse lasers. The dispersion is provided by either optical fiber or CFBGs. The advantage of using CFBGs over long fiber spools is the preservation of the coherence of the laser due to the short propagation distance. However, modulation on the group delay of CFBGs leads in deviation from linearity of the dispersion, as is discussed in the Appendix.

Ultra-short pulses are usually generated with non-uniform spectral density and therefore cannot fill their period with uniform temporal intensity without overlap. Feed-forward systems that equalize the temporal intensity profiles of the pulses have been demonstrated [12] [13] and are one of the foci of the experimental work conducted for this dissertation. The student’s work on the subject is presented in section 3.5.

1.3.2 RF-tuned, high-dispersion lasers

In a different approach, laser sources are used to directly generate frequency swept pulses. All swept laser source architectures comprise of some type of an active driving mechanism, as ultra-long chirped pulses via passive mechanisms have not been demonstrated.

One of the laser architectures for attaining frequency swept pulse trains combines the use of group delay dispersion with radio frequency (RF) sweep. The laser repetition rate is an integer multiple of the cavity mode spacing (f), which for ring cavities is given by: $f = {}^{c}\!\big/_{n(\lambda)\cdot L}$, where c is the speed of light, n is the cavity effective refractive index, L is the path length, and λ denotes wavelength. In highly dispersive cavities the refractive index varies strongly across the bandwidth supported by the gain medium. Thus, for a fixed cavity length and a linearly swept RF frequency drive, the above equation is satisfied for different spectral components [14]. Therefore, linear RF sweep translates into an optical frequency sweep. A schematic of this laser architecture is presented in Figure 1.3 (a).

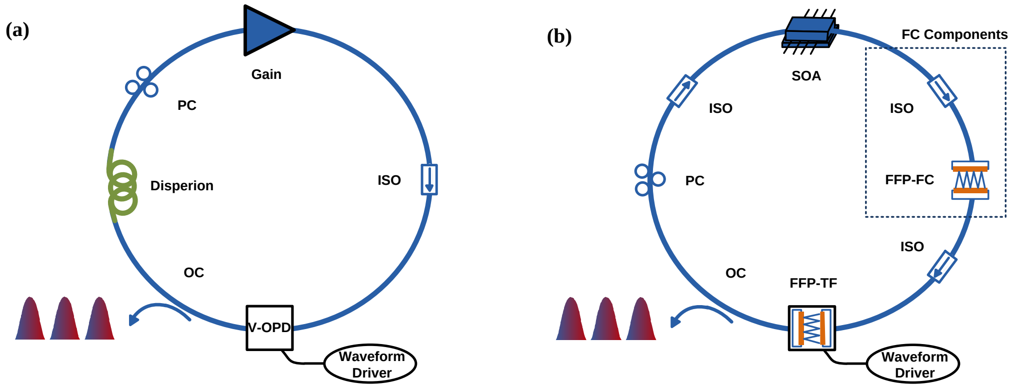

Figure 1.3: (a) RF-tuned, high-dispersion frequency swept laser schematic adapted from [14]. (b) Fourier domain mode-locked laser (FDML) schematic adapted from [15]. The components in the dotted box are added for a specific implementation [16]. PC, polarization controller; ISO, isolator; V-OPD, variable optical path length delay; OC, output coupler; SOA, semiconductor optical amplifier; FFP-FC, frequency comb fiber Fabry-Pérot; FFP-TF, fiber Fabry-Pérot tunable filter.

As discussed in [14], the bandwidth of the semiconductor based swept pulses is inversely proportional to the laser cavity dispersion and the sweep is linear in wavelength. The demonstrated swept pulse bandwidth is in the order of 100 nm. However, the pulses do not fill the period of the laser and the sweep rates are in the order of 200 kHz. The sweep rate is limited by the dispersion element and from the availability of linearly swept RF sources. A system using solely fiberized components based on the same concept was recently demonstrated [17]. In that scheme a fiber optical parametric oscillator (FOPO) is used, resulting in similar results for the operation bandwidth and sweep rates.

1.3.3 Fourier domain mode locking

The Fourier domain mode-locked laser (FDML) is another actively driven laser architecture having swept pulse output, a schematic of which is shown in Figure 1.3 (b). This approach was first demonstrated by Yun et al. in 1998 for the generation of a swept source to interrogate fiber grating sensors at a sub-Hz frame rate [18]. A ring laser cavity with semiconductor gain is developed containing a fiberized Fabry-Pérot etalon. By design, the free spectral range (FSR) of the etalon must be larger than the attained optical frequency sweep and the etalon resonance wavelength must be voltage tuned. A piezo-electric actuator is used to tune the etalon’s transmission frequency. Since the laser’s narrowband gain window is swept in time, the laser output is frequency swept. The first demonstration of this architecture having a broadband sweep showed a bandwidth of 120 nm centered at 1300 nm with a linewidth in the 10 GHz regime and a sweep rate in the order of few tens of kHz [15]. The sweep of the laser does not fill the laser period and is nonlinear in frequency. Thus, a secondary system is developed to synchronize the frequency sweep with experimentally acquired time data.

An extensive analysis of this type of swept laser architecture reveals two regimes of operation; when the etalon sweep is slow enough such that lasing has sufficient time to build-up from amplified spontaneous emission (ASE), and the case where the sweep is faster than that time [11]. In the latter case, the regenerative operation of the laser is suppressed, the output power is reduced and the laser linewidth is broad. In the slow sweep rate case, each laser component reaches quasi-saturation and the linewidth of the laser is improved. As calculated by the model presented in [11], even for the rapid sweep limit the attained sweep rates are at a rate of ~30 kHz for the cavity parameters usually used. Faster rates cannot be attained due to the mechanical nature of piezo-electric sweep and would also result into a linear degradation of the energy per pulse. Recently, researchers have expanded the swept pulse bandwidth to ~160 nm by combining two semiconductor optical amplifiers in parallel with peak gain at 1.3 μm and 1.5 μm [19].

In a more recent implementation of the FDML architecture called frequency comb (FC-FDML), a second etalon with a narrower FSR is inserted in the laser [16]. This effect makes the output of the laser sweep have quantized frequency steps, instead of the continuous sweep of the conventional FDML design. The sensitivity of the OCT experiment demonstrated is improved and the OCT system is simplified since the laser provides a temporal-to-wavelength calibration output. Nonetheless, the pulse chirp is nonlinear and faster sweep rates would have reduced average power.

1.3.4 Rotating element lasers

A different approach, which also incorporates mechanically controlled elements, is based on gratings. The rapid scanning optical delay (RSOD) was first demonstrated by Tearney et al. [20], and it incorporates a grating and a mirror rotating relative to each other. Either the mirror or the grating of the mirror-grating system is mounted on a rotating galvanometer. Different angles between the grating and the mirror result in different relative path length, or time delay, and thus a frequency swept output is attained. In a more recent implementation, a linear cavity architecture is used with semiconductor gain resulting in 16 kHz sweep rates and spectral bandwidth in the order of 90 nm [21]. This architecture has been commercialized into a product demonstrating comparable performance [22].

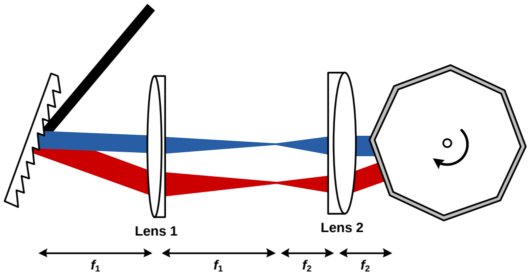

Figure 1.4: Swept source based on a grating a rotating element (prism). Adapted from [23].

In a similar approach, a 4-f setup is used, as shown in Figure 1.4. The axis of a mechanically rotating reflecting element is positioned at the focal point of the rear lens [23]. Semiconductor gain is used in a ring cavity design resulting in a ~80 nm bandwidth, which is limited to a ~16 kHz sweep rate due to the inertia of the rotating parts and the laser build-up time. This approach is offered as a product by a different vendor [24].

CHAPTER 2: PRINCIPLES OF ANALOG-TO-DIGITAL CONVERSION

2.1 Introduction to Analog-to-Digital Conversion

Analog signals are the signals that are experienced in the macroscopic natural world and they consist of time varying *continuous* values of some parameter, for example light or sound intensity [25]. On the other hand, a digital signal is a *discrete in time* signal, meaning that the varying parameter does not change values in a continuous fashion, but instead changes values in discrete steps; it remains constant for a specific time interval and shifts to a different value in a non-continuous way. The difference between an analog and a digital signal can be seen in Figure 2.1.

When operating on a signal, there is great advantage in the signal being in a digital form. That is because a digital signal can be amplified and processed without the addition of almost any noise, while an analog signal suffers from noise, dispersion and nonlinear effects added upon it in every procedure performed. Digital signals travel the distance to receivers virtually distortion-free, which is the key technology allowing data links to exhibit Bit Error Rates in the order of 10^{-9}, which translates in one error bit in every one billion correct bits transmitted.

A signal is converted from analog to digital using an analog-to-digital converter. The process is called analog-to-digital conversion (ADC) and the operation of analog-to-digital converters is comprised of two distinct processes:

- Sample and hold the signal; acquire the amplitude of the signal and retain its value for some time. This is because the time that the signal is being sampled is usually much shorter than the sampling period [26, 27].
- Quantize the voltage into a predefined number of levels.

The number of levels is usually an integer power of 2, thus the number of levels N is defined as its base two logarithm. For example a 10-bit ADC system has 1024 levels.

Even an error-free quantization process induces errors in the digitized signal due to the fact the digital signal retains the digitized value within the sampling period while the analog signal varies continuously in time, as shown in Figure 2.1.

The ADC process is described using the following parameters, where examples for typical values are given in the parentheses:

$$\left.\begin{array}{ll}
\bullet & V_{FS}\text{, the full scale voltage that can be converted (} V_{FS} = 1V \text{)} \\[6pt]
\bullet & Q = \frac{V_{FS}}{2^{N}-1}\text{, the voltage quantization factor (} Q = 0.067V \text{)} \\[6pt]
\bullet & \varDelta Q = \frac{Q}{\sqrt{12}}\text{, the RMS quantization error (} \varDelta Q = 0.019V \text{)} \\[6pt]
\bullet & SNR_{Q}(dB) = 20 \cdot log_{10}\left(\frac{V_{FS,rms}}{\varDelta Q}\right)\text{, the corresponding signal-to-noise ratio}
\end{array}\right\} \qquad (2.1)$$

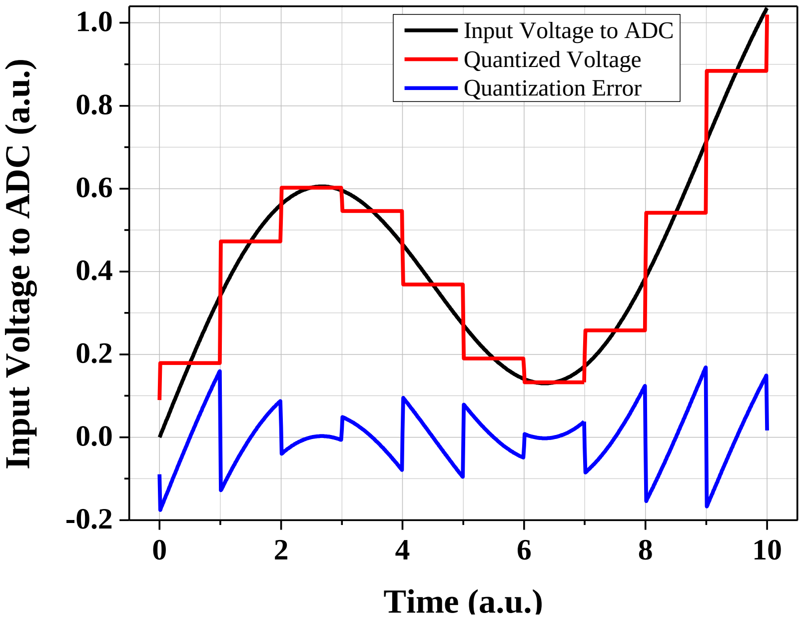

Figure 2.1: Input signal versus time (green) and its digitized form (red). The blue line represents the error of the digitization process. Sampling rate = 2 Samples/second [28].

Noise coming from timing or amplitude variations of the sampling mechanism can degrade the performance of ADCs, decreasing the number of maximum bits that an ADC can deliver from its nominal value *N* to the effective number of bits (ENOB). As an example, Figure 2.2 shows the difference between increasing the number of bits N in a system with low amplitude noise compared to a system that exhibits higher noise. In the first case, shown in the upper row of Figure 2.2, one can increase the number ENOB of the ADC just by using an ADC with higher N, while in the second row the noise inherent in the signal makes any increase of N above 4 futile, since the ENOB cannot be improved.

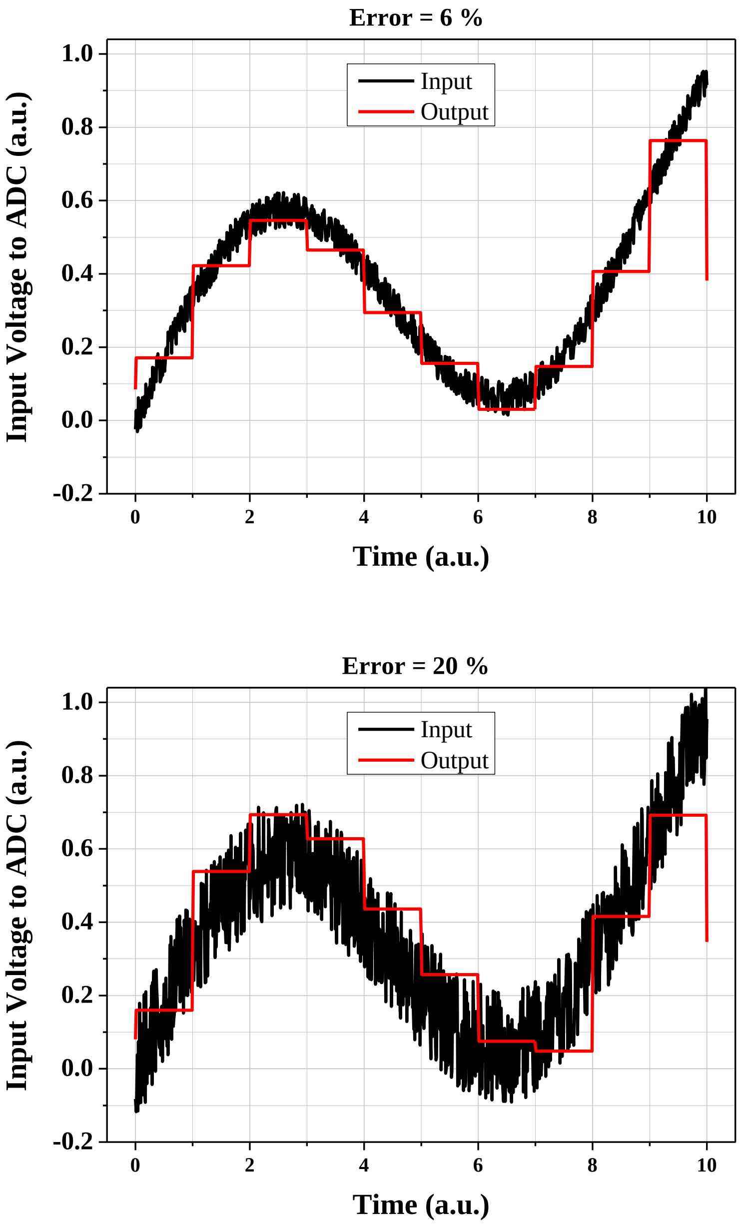

Figure 2.2: Demonstrating the difference between the number of bits that the digitizer is capable of distinguishing (N = 4) and the effective number of bits (ENOB). In a low noise signal N = ENOB (left). However, as the noise in the system becomes comparable to $1\text{-}2^{N\text{-}1}$ an increase of N does improve the ENOB resulting in ENOB < N (right) [28].

A detailed review of the performance of electronic ADCs can be found in [29] and a brief summary of this information can be seen in Figure 2.3, where the effective number of bits versus the system's bandwidth is presented. Also some fundamental limitations for ADCs due to thermal noise or sampling aperture duration are depicted. Thermal or Johnson noise is the white noise arising from thermal electronic fluctuations in the system's components. Comparator ambiguity results from the finite time required by the transistors in the comparator circuit to respond to small voltage differences during the quantization process [30].

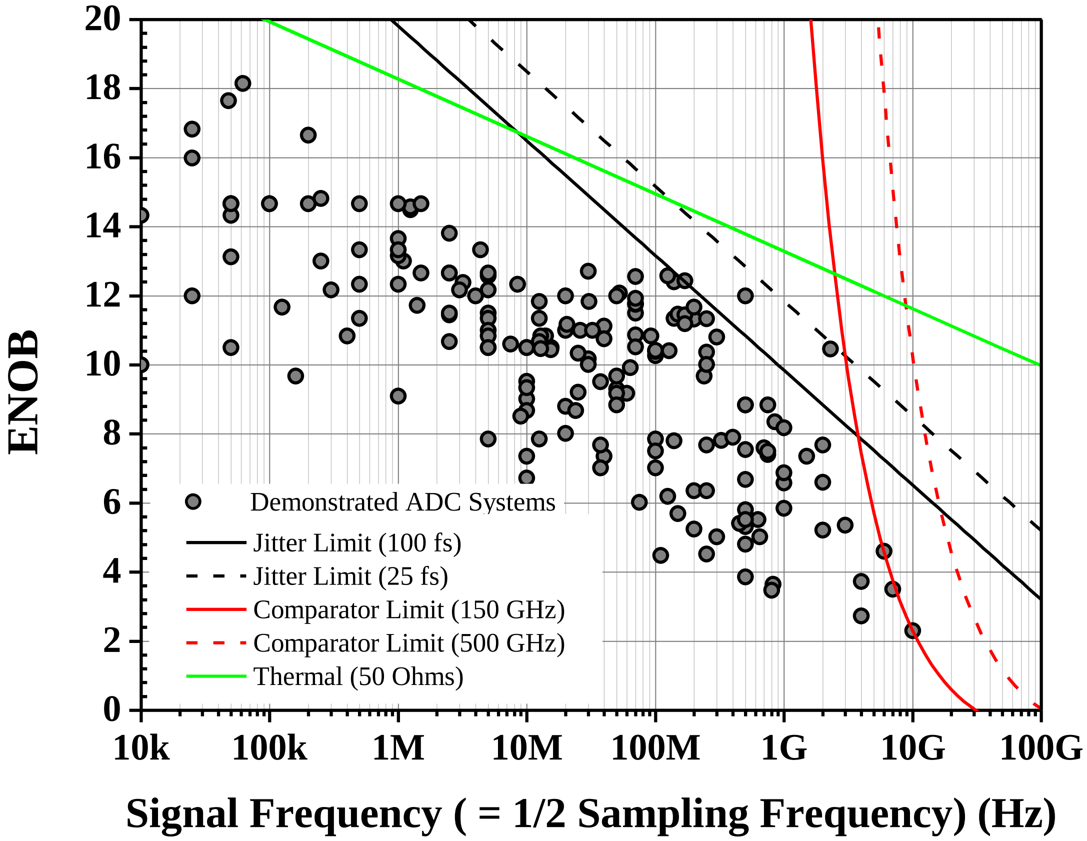

Figure 2.3: ENOB as a function of frequency for existing ADC systems [31].

Notice that in most cases, usually at the user interface level, a signal has to be transformed back to the analog format. For example, the music digitally inscribed on a compact disk surface has to be converted to analog before sent to the speakers. This procedure is performed by a digital-to-analog converter (DAC) and details for those devices can be found in [27, 30, 32].

This work focuses on developing laser sources suitable for high bandwidth photonic ADC. Thus a brief description of the available types of photonic ADC is presented in this chapter, as well as a description of the limiting parameters of ADC.

2.2 Photonic Analog-to Digital Conversion

2.2.1 Classification of Photonic Analog-to-Digital Conversion

Many different implementations of analog-to-digital converters are described by the term *photonic analog-to-digital conversion* which uses photonic technology to convert an analog RF signal at the input to a digital RF signal at the output. Note that although the term photonic might imply conversion or manipulation of an optical signal at the input, the term photonic ADC identifies conversion of RF signals; it is the photonic technology used in one or more steps of the conversion that gives its name to the field.

As we have previously discussed, the ADC process consists of two major functions: sampling and quantization. Photonic ADC systems are divided into categories depending on which of the conversion functions is implemented using photonic technology. Accordingly, there is photonic *sampled*, photonic *quantized*, photonic *sampled and quantized* and photonic *assisted* ADC. The latter describes the case that neither the sampling nor the quantizing is directly performed using photonics. In this work, the focus is on photonic sampled ADC and time stretched photonic ADC, which is a subcategory of photonic assisted ADC. The history of other types of photonic ADC is briefly described. The classification of photonic ADCs is seen in Figure 2.4.

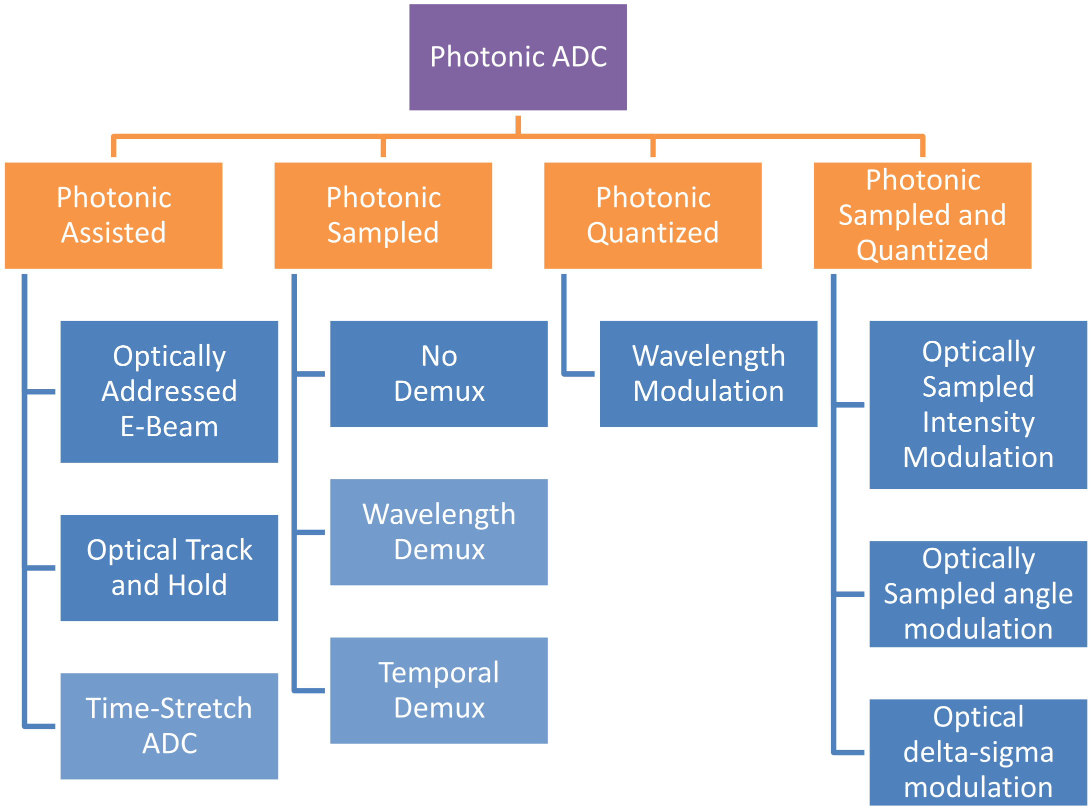

Figure 2.4: Classification of photonic analog-to-digital converters as discussed in [28]. The types of photonic ADC discussed in more details in the text are highlighted.

2.2.2 Photonic Quantized ADC

The majority of the work that demonstrates photonic quantized ADC uses a wavelength-tunable laser being driven by the RF input signal. The optical frequency of the laser changes as a function of the amplitude of the RF signal and when the laser beam is passed through an angular dispersive element, such as a prism or grating, different amplitudes of the RF signal diffract at different angles. Finally, the diverging beam can be focused on a photo-detector array to electrically sample the signal [33-36]. Some researchers have used WDM filters instead of the gratings that significantly simplify the alignment of system components [34].

2.2.3 Photonic Sampled and Quantized ADC

In photonic sampled and quantized ADC, the role of electronics is minimized and both main functions are performed using photonic technology. One method that has been popular utilizes multiple intensity modulators and was suggested by Taylor in 1975 [37]. The basic idea is to use intensity modulators with increasing electrode length. The electrode relative length of the n^{th} intensity modulator is in the general case $1/2^{(N-n)}$, where N is the number of bits that the system is designed for, which is equal to the total number of modulators used.

By setting each DC bias voltage appropriately such that each comparator is set at the middle of the transmission curve, one can get the coding systems, called the gray code, which corresponds to the complete set of quantized input RF signal levels. More information about this scheme can be found in [37-39].

In a more recent approach, the RF signal is optically sampled and then directed to the center of a micro-ring resonator [40]. Multiple wavelengths are input on the waveguide micro-ring resonator, while the varying intensity of the control beam changes the properties of the resonator, allowing different wavelengths to resonate and exit the ring depending on the intensity of the control beam. The advantage of this technique is that it leads to quantization of the incident beam intensity without the use of electronics. However it is limited by non-linear effects due to the physics of the ring resonator.

2.2.4 Photonic Sampled ADC

In photonic sampled ADC, the sampling function of a classical ADC circuit is substituted by photonic sampling, while the quantization is still done by classical electronics. Since the quantization function is performed in the classical way, the noise restrictions of the system are the same as in electronic ADCs [41]. However, the performance of a photonic sampled ADC can improve over a classical approach by replacing the electronic clock with an optical clock having superior performance.

In the general scheme of photonic sampled ADC, the incoming RF signal is first converted into optical signal using an electro-optic transducer. The optical signal can then be directly photodetected or demultiplexed. Of these options, only the latter offers a potential advantage over electronic ADC. Thus, this work will focus on the two different demultiplexing techniques.

As mentioned, the incoming RF signal is converted into optical signal using a transducer. In almost all cases, the transducer chosen is an electro-optic amplitude modulator (modulator or EOM from this point on) which is essentially an integrated Mach-Zehnder $LiNbO_3$ interferometer, in which a linear electrically-induced relative phase difference between its two arms is translated into *sinusoidal* change of the optical intensity at its output. The nonlinear transfer function of a modulator can limit its useful depth of modulation leading to power inefficiency and nonlinear effects unless it is compensated for. Betts [42] and others have shown that the nonlinearity of the transmission function of a modulator can be overcome, thus it is not the limiting factor of photonic sampling. Another concern could be the photodetector's bandwidth, but photodetectors with high bandwidth and responsivity have been available at reasonable cost for some time now. The limiting factor for the performance of photonic sampled ADC is the optical clock. Nevertheless, optical clocks can have superior performance compared to electronic clocks. As an example, the noise of optical clocks due to the amplitude and timing variations can be significantly improved over electronic clocks currently in use. Moreover, optical pulses have been demonstrated having significantly shorter time duration than electric pulses, a key advantage for sampling, as will be discussed later in this text.

The two different ways of demultiplexing the photonic signal are presented, followed by an analysis of the limitations posed by the performance of the optical clock.

The optically sampled signal is split into different segments that contain less bandwidth compared to the input signal, using either *time* or *wavelength* demultiplexing. Both methods aim at partitioning the sampled signal which increases the effective bandwidth of the system. That means that, excluding other limitations, demultiplexed photonic ADC can surpass the speed of electronic ADC.

The time demultiplexed photonic sampled ADC, first implemented by Bell et al [43], uses N stages of 1x2 switches configured in a tree setup to divide subsequent pulses of the optic signal into different channels, as seen in Figure 2.5 (a). The switches must be driven by an accurately synchronized clock, which is difficult to implement and moreover the switching procedure can induce amplitude noise on the sampled train reducing the ENOB. The optical clock used is a mode-locked laser that is easy to develop and has the suitable performance as will be discussed later.

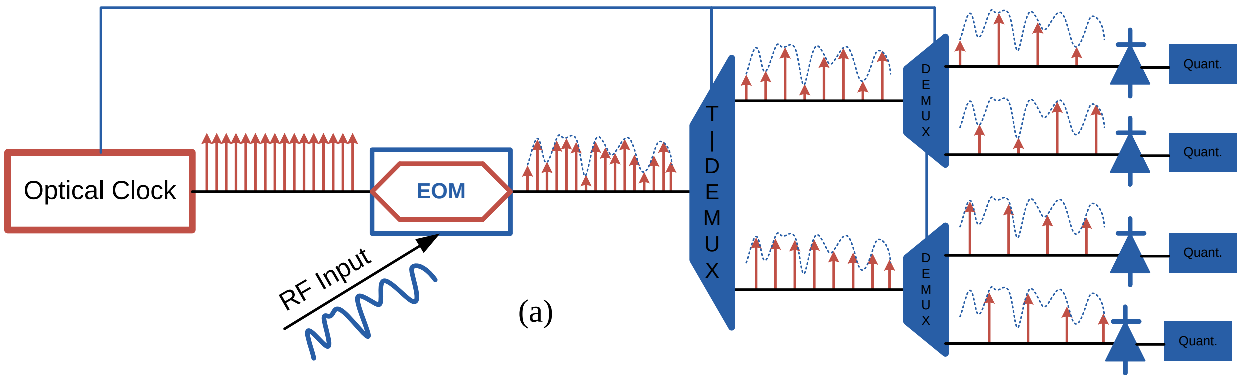

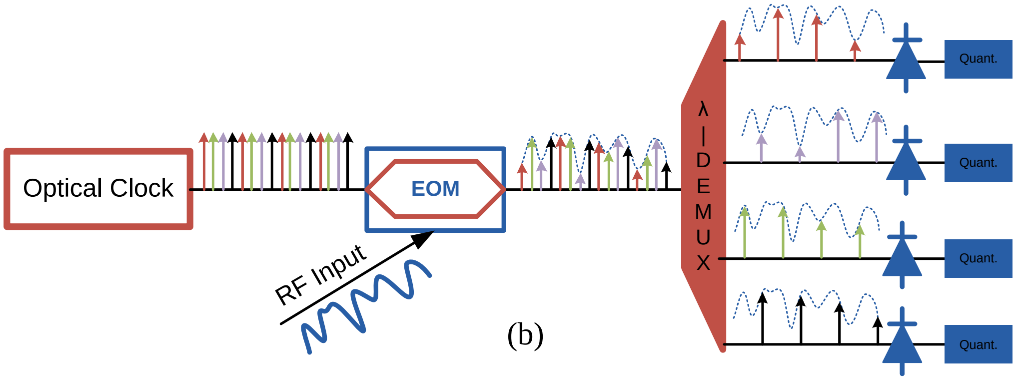

Figure 2.5: Conceptual representation of photonic sampled ADC. (a) Single wavelength MLL and time demux, (b) multi-wavelength MLL and WDM demux. Red/blue is for optical/electronic components. EOM: Electro-Optic Intensity Modulator. Note the simplicity of the multi-wavelength MLL approach.

Wavelength demultiplexed photonic sampled ADC, on the other hand, uses a simpler demultiplexing scheme at the expense of requiring a more sophisticated optical clock. The pulses are easily separated into different channels using periodic in wavelength filters that are broadly used in optical communications and especially in wavelength division multiplexing (WDM) (Figure 2.5 (b)). The WDM filters are passive devices and do not add any dynamic amplitude or timing distortion on the different channels, but they require pulses with spectra periodically centered at different wavelengths. For this purpose multi-wavelength mode-locked lasers are used, but multi-wavelength optical clocks with the performance that would lead to improvement of the ENOB achieved by photonic ADC over electronic ADC have not yet been demonstrated.

The best results demonstrated show timing jitter in excess of 1 ps, when the jitter required, as will be analyzed next, is approximately two orders of magnitude less [44, 45]. On the other hand, photonic sampled and time demultiplexed photonic ADC can use standard mode-locked lasers that have been demonstrated having enhanced performance over their multi-wavelength counterparts [46].

2.2.5 Clock Requirements for ADC and Photonic Sampled ADC.

The reason behind the use of photonic sampled ADC is that the laser sources available have superior performance compared to electronic samplers at high sampling rates. Since both an electronic and an optical sampler perform the same function on the incoming RF signal, their noise constraints and analysis are identical.

The performance of the electronic or photonic sampled ADC is limited by both fundamental constraints and the optical clock's performance as seen in the following analysis adapted from [41, 47].

2.2.5.1 **Fundamental constraints**

2.2.5.1.1 *Thermal or Johnson noise*

Every signal is poisoned by thermal (Johnson) noise, which comes from the thermal agitation of the electrons inside an electrical conductor at equilibrium. This happens regardless of the applied voltage [48, 49]. Thermal noise has white spectral density and its power spectral density is given by:

$$\overline{V^2} = 4 \cdot k \cdot T \tag{2.2}$$

The thermal noise of a sampling procedure can be found using equations (2.1) and (2.2) to be:

$$B_{thermal} = \log_2 \left(\frac{V_{full\ span}^2}{6 \cdot k \cdot T \cdot R \cdot f_{sampling}} \right)^{1/2} - 1, \tag{2.3}$$

where k is the Boltzmann constant = $1.38 \cdot 10^{-23}\ \frac{J}{K}$ and R is the effective resistance of the circuit.

As seen in Figure 2.8, the thermal noise limit has not yet been reached and the ADC systems are limited by other noise contributions.

2.2.5.1.2 *Shot Noise*

Shot noise is a quantum effect. It occurs during experiments that measure a property carried in a quantized amount by particles such as photon energy, or electronic charge. In principle, the smaller the nominal (average) value of the quantity measured, the more prominent the effect of the shot noise becomes.

The ENOB for a shot noise limited system is given by:

$$B_{shot} = \log_2 \left(\frac{V_{full\ span}}{6 \cdot R \cdot q \cdot f_{sampling}} \right)^{1/2} - 1, \tag{2.4}$$

where q is the electronic charge ($1.602 \cdot 10^{-19}$).

2.2.5.1.3 *Heisenberg's uncertainty*

Since sampling is the procedure in which the intensity of a specific signal is acquired within a specific time interval, the ultimate limit for any sampling procedure is defined by the Heisenberg uncertainty principle: $\Delta E \cdot \Delta t \geq \hbar$. A derivation for the limit of the uncertainty principle is presented in Figure 2.6.

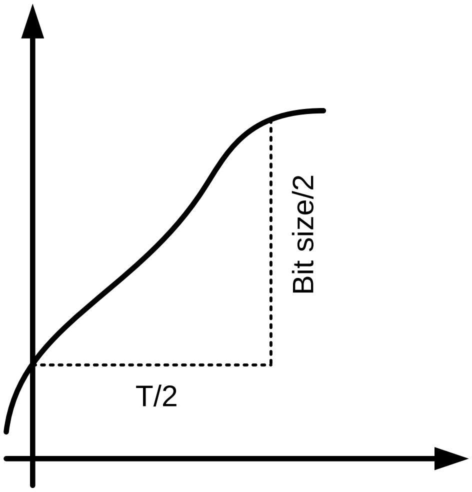

$$f_{sampling} = \frac{1}{T} \qquad Bit\ Size = V_{full\ span} \cdot 2^{-N}$$

$$R = 50\Omega \qquad \Delta t = \frac{T}{2}$$

$$\Delta E = P \cdot \Delta t = \frac{V^2}{R} \cdot \frac{T}{2} = \frac{(Bit\ size/2)^2}{R} \cdot \frac{T}{2}$$

$$\Delta E \cdot \Delta t = \frac{(Bit\ size \cdot T/4)^2}{R} \geq \hbar$$

$$2^N \cdot f_{sampling} \leq \frac{V_{full\ span}/2}{\sqrt{\hbar R}} \rightarrow \qquad N = \frac{log\left(\frac{V_{full\ span}/2}{\sqrt{\hbar R} \cdot f_{sampling}}\right)}{log(2)}$$

Figure 2.6: Schematic explanation of Heisenberg's uncertainty principle and the limitation on ADC samplers, as adapted from [41].

$$B_{heisenberg} = N = \log_2\left[\frac{V_{full\ span}/2}{\sqrt{\hbar R} \cdot f_{sampling}}\right] \tag{2.5}$$

$B_{heisenberg}$ is the ENOB for a system limited only by the uncertainty principle and ħ is Plank's constant divided by 2π.

The above equation results in 13 bits at 840 GHz and 19.4 bits at 10 GHz. These values are a much larger compared to ENOBs currently achieved from either electronic or photonic ADC since the uncertainty limit is the ultimate limit that an ADC system could reach. The uncertainty principle limit can be seen in Figure 2.8 and Figure 2.9.

2.2.5.2 **Optical clock performance constraints**

2.2.5.2.1 *Timing jitter or phase modulation (PM) noise*

The timing jitter of the sampling gate comes in effect due to imperfections of the sampling period of an ADC; the sampling gate period varies in time with a certain mean value and standard deviation. The mean time period is the inverse of the repetition rate of the mode-locked laser used, while τ_J is a measure of the variation of the sampling point and is defined as the root-mean-square jitter of the gate. Assuming that τ_J is known, an expression for the voltage error due to it can be calculated (2.6). This is depicted in Figure 2.7 as broadening on the time axis.

$$B_{jitter} = \log_2\left[\frac{2}{\pi \cdot f_{sampling} \cdot \tau_J}\right] - 1 \qquad (2.6)$$

2.2.5.2.2 *Amplitude jitter or amplitude modulation (AM) noise*

Amplitude noise affects the performance of an ADC directly since the optical clock's amplitude variation, having a statistical standard deviation (σ_{amp}), gives quantization errors. The ENOB is defined for the case that σ_{amp} is set to be equal to half a bit. This effect is seen in Figure 2.7, where a substantial amplitude jitter limits the ENOB of the system. The formula giving the ENOB as a function of σ_{amp} is:

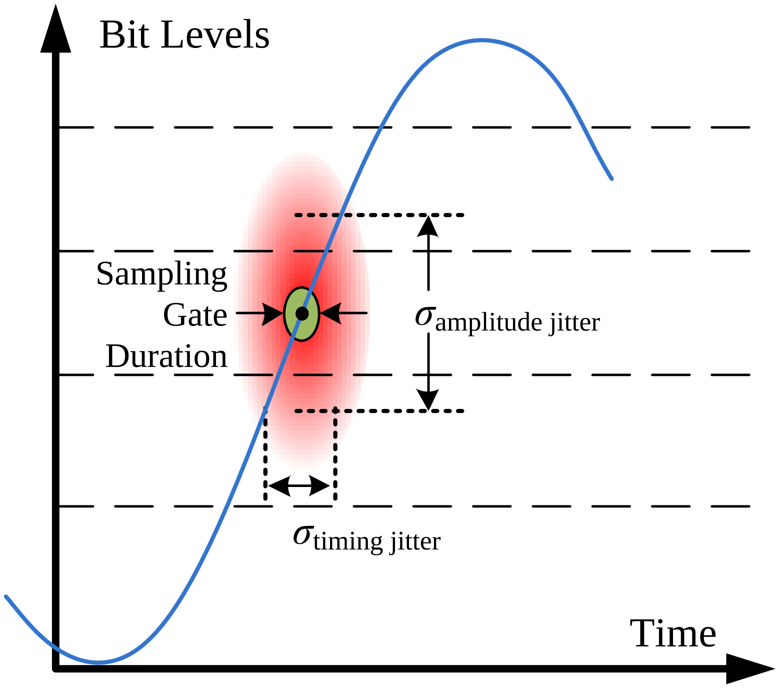

Figure 2.7: Impact of noise of the clock during the sampling procedure. Notice the reduction of N to ENOB due to noise.

$$B_{amp} = \log_2\left[\frac{1}{\sigma_{amp}}\right] - 1 \tag{2.7}$$

2.2.5.2.3 *Gate duration*

Finally, the pulse duration τ_p limits the ENOB due to the finite duration of the sampling gate. The relation connecting the two quantities is the following:

$$B_{pulse} = \log_2\left[\frac{12}{\sqrt{3}\cdot\pi\cdot f_{sampling}\cdot\tau_p}\right] - 1 \tag{2.8}$$

2.2.5.3 **Comparator ambiguity**

As discussed previously, the comparator ambiguity is due to the finite speed of the comparator components that are always used at some point in electronically quantized systems. Comparators define thresholds above which bits are assigned different values. As discussed in [41], the ENOB as function of the sampling frequency for the comparator ambiguity is given as:

$$B_{ambiguity} = \frac{\pi\cdot f_T}{6.93\cdot f_{sampling}} - 1.1 \tag{2.9}$$

where f_T is related to the regeneration time of the comparator by $\tau_{reg} = 2.5 / \pi \cdot f_T$ and is a characteristic of the comparator used. Typical values for τ_{reg} are in the 1 ps range.

The above noise limits for a system close to the current state of the art are presented in Figure 2.8 and Figure 2.9.

In Figure 2.8 and Figure 2.9 one can see that systems of current and perhaps near future technology are far away from being thermal noise limited and that a system can never become uncertainty principle limited because thermal noise will limit the development at an earlier stage. Moreover, it is observed that for low sampling frequencies both systems are AM noise limited (one cannot do much better than 12 bits) but for higher sampling frequencies the systems become timing jitter or pulse width limited. Supposing that pulses can be compressed to the few hundreds of femtoseconds regime using ideal pulse compressors, then one concludes that *ADC systems at high sampling rates (>10 GHz) are timing jitter limited.*

Finally, it should also be noted that there is a high demand for faster comparators that will enable direct analog-to-digital converters to go into the tens of GHz sampling speeds.

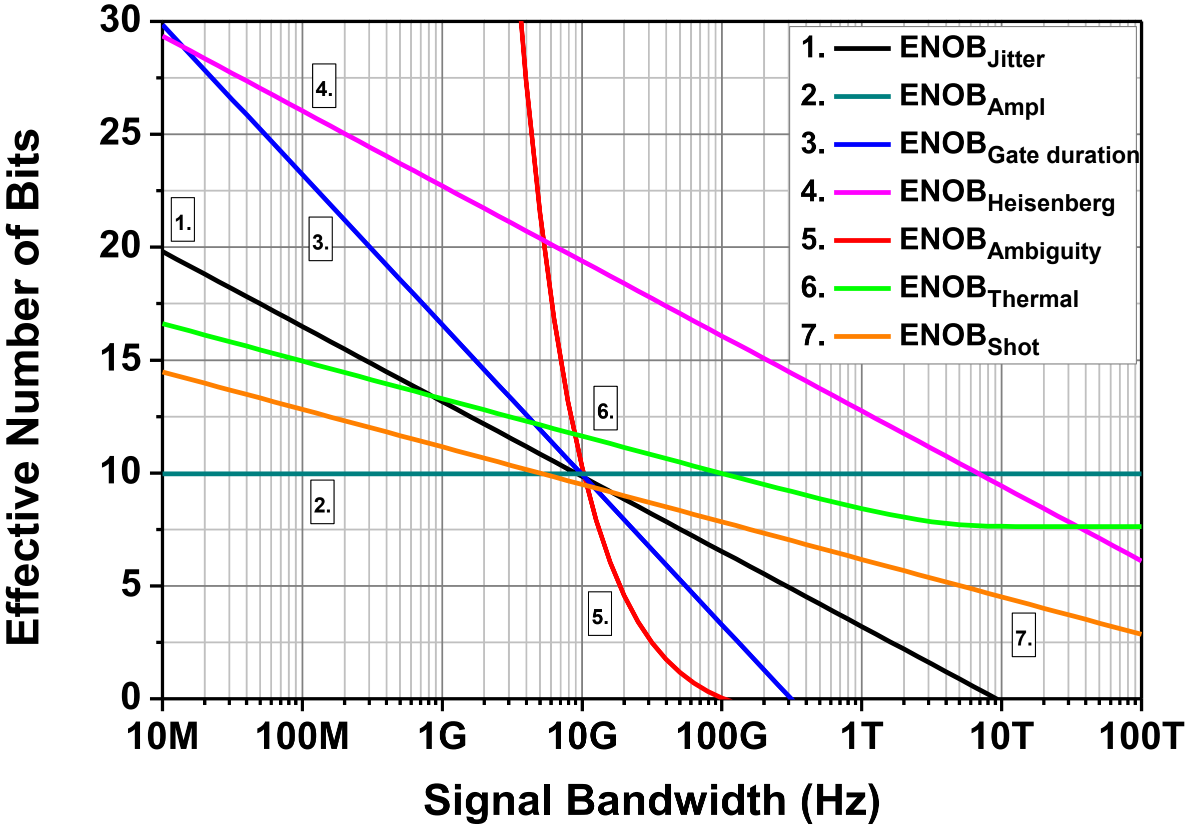

Figure 2.8: Example of ENOB versus sampling frequency for: Timing Jitter = 10 fs, Amplitude Jitter = 0.05 %, Pulse duration = 2.5 ps, comparator regeneration time constant 1.6 ps.

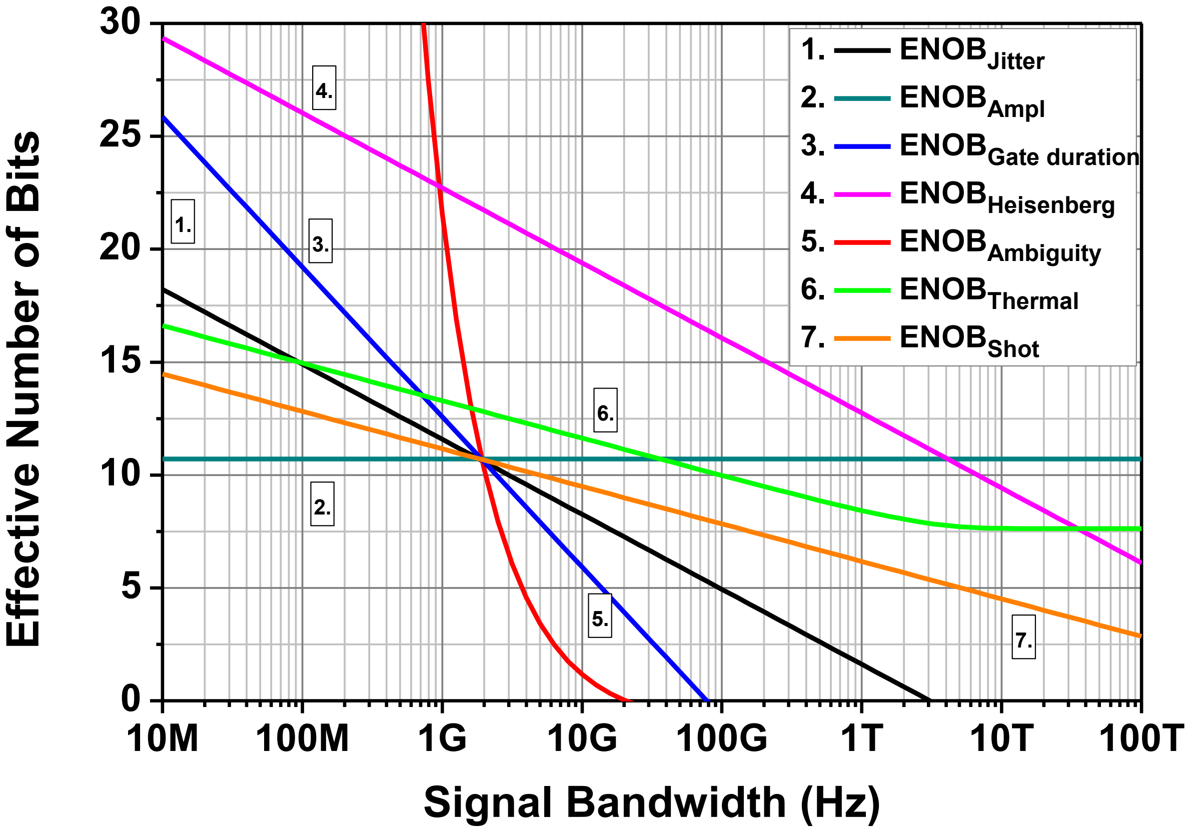

Figure 2.9: Example of ENOB versus sampling frequency for: Timing Jitter = 30 fs, Amplitude Jitter = 0.03 %, Pulse duration = 10 ps, comparator regeneration time constant 8 ps.

2.3 Photonic Assisted ADC

2.3.1 Review of photonic assisted ADC types

In photonic assisted ADC, neither the sampling nor the quantizing functions are performed using photonic technology, but instead optical technology is used at some part of the analog-to-digital system in a way that is beneficial to the system. In the literature, one can find references for optoelectronic track and hold, where a laser beam is used to sample the signal and hold its value for some specific time [50], optically triggered electronic ADC, in which the electronic ADC sampling is activated using an optical clock [51, 52], and optically triggered e-beam ADC, where the deflection angle of an electron beam changes as a function of input RF signal's amplitude [53, 54]. For the purposes of this work, the analysis will focus on time-stretch photonic ADC.

2.3.2 Time-stretch photonic ADC

In general, a time-stretch (TS) photonic ADC uses stretching of the photonic signal in time to reduce the effective bandwidth needed for sampling [55]. There are two different modes of operation both offering increase in the effective bandwidth of the system. In the single-shot TS technique great stretch ratios can be achieved, but the stretched signal's duration cannot exceed the period of the laser source used. In contrast, in continuous TS technique allows for any signal to be sampled at the expense of system design complexity. A schematic design for the two techniques is seen in Figure 2.10 and Figure 2.11. An in-depth analysis of TS photonic ADC can be found in [56].

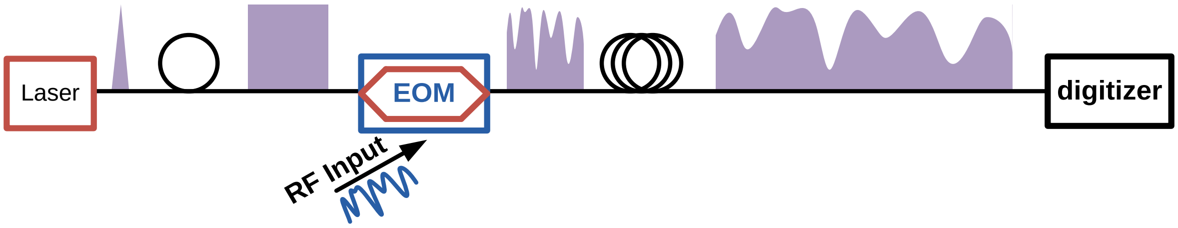

Figure 2.10: Single-shot time-stretch photonic ADC. Notice that the pulse coming out of the first stretcher does not have to fill the time between the two pulses. EOM = Electro-optic amplitude modulator.

Both techniques use a short pulse laser source producing near transform limited pulses with large spectral bandwidth. The pulses are stretched using a dispersion element, most frequently a spool of SMF-28 fiber, producing linearly chirped pulses with time duration in the nanosecond range. In the continuous operation technique, the pulses have to fill the inverse of the repetition rate of the laser, whereas for the single shot case the stretching limitation comes from the RF signal that needs to be decoded. After the time stretching, the input RF signal is imposed upon the stretched pulse using an intensity modulator providing an optical pulse modulated at the speed of the RF signal. Finally, the pulses are stretched further, resulting in a reduction of the RF signal's bandwidth. The factor defined as $M = 1 + {}^{L_2}/_{L_1}$ defines the amount of stretching of the pulse after the second fiber spool compared to the first stretching and is equal to the reduction of the bandwidth of the signal. Usually the digitizers at the end of the system have a bandwidth in the gigahertz range, thus the effective bandwidth of the system, due to the time-stretching, is multiplied by a factor M, resulting in tens of gigahertz of effective system bandwidth. At the end of the system, the information has to be interleaved using electronics, in order to form the input RF signal.

Note that in the single-shot TS ADC technique the property of the pulse train being linearly chirped is not being used in a way that promotes the signal conversion, but in the case of the continuous TS ADC shown in Figure 2.11, the signal is separated in different ports without much complexity using a passive periodic filter like the ones frequently used in wavelength division multiplexing systems.

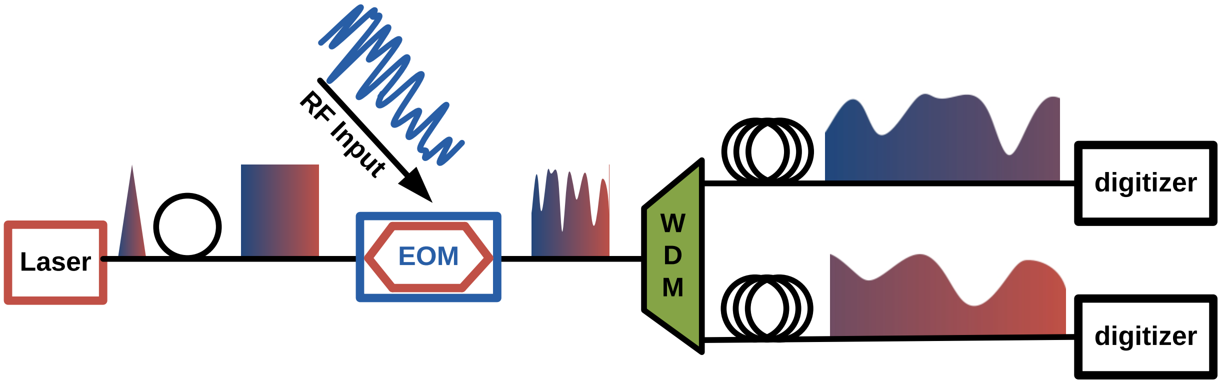

Figure 2.11: Continuous operation time-stretch photonic ADC. Stretching ratio = 2. Notice that the signal fills the time slot of the period of the laser allowing for continuous operation. EOM = electro-optic amplitude modulator, WDM wavelength demultiplexing filter

It is proven in [56] that indeed the bandwidth of TS ADC is reduced by a factor M compared to conventional sampling and moreover, the signal-to-noise ratios (SNR) of thermal and shot noise contributions are conserved, even though the power is divided by M after the second stretching, due to the decrease of the bandwidth by the same factor. The SNR ratio of the jitter is actually improved by this technique for the same reasons. The SNR of the system is usually set by the use of Erbium-doped fiber amplifiers (EDFA) that are used to compensate for the losses and the power per unit wavelength (spectral power) of the broadband laser source.

An inherent advantage of the continuous TS ADC is that the recombination of the RF signal to a continuous signal at the back end of the system can be simplified by using WDM filters that are not perfectly sharp, allowing some small parts of the signal to be shared among neighboring channels. That common part of the signal can be used to connect correctly the sampled signal parts together to form the complete signal at the output.

Although, the timing jitter constraint of TS ADC is relaxed by the stretching factor (M), this is not valid for the continuous TS ADC system. This is because that although the demultiplexed segments can be sampled with relaxed accuracy, they have to be interleaved at the appropriate time slots in order to form the input high bandwidth signal. The interleaving process at the back end of the system has to follow the timing accuracy of the input signal. Thus, the timing jitter constraint is not relaxed and the calculation for the ENOB has to contain the full bandwidth of the original RF signal.

Notice also that the laser source that is needed for TS ADC must have similar specifications to those constraints, as discussed in the time sampled photonic ADC. Thus, there are many similarities in the two approaches and a laser source can be used in both schemes.

Single-shot implementations of TS photonic ADC use ultra-short pulses and SMF as the dispersion element. This technique has achieved as much as 250 times improvement of the sampling speed of a commercially available oscilloscope attaining a 10 TSample/s sampling rate [57]. A continuous operation four-channel system was demonstrated which enhanced the sampling rate and bandwidth of an oscilloscope to 150 GSample/s and 48 GHz respectively, a 3-fold improvement [58].

CHAPTER 3: EXPERIMENTAL WORK

3.1 Introduction

The goal of this work is to provide a low repetition rate, semiconductor-based laser source suitable for high bandwidth photonic ADC. As discussed previously, TS ADC and photonic sampled ADC share common specifications and constraints for the pulsed laser source. Nevertheless, the repetition rate (frequency) of the pulsed laser is different for the two techniques. In photonic sampled ADC a high repetition rate laser is pursued in order for the system to have high bandwidth, whereas for TS ADC a low repetition rate laser is more convenient since the pulses will be stretched and the desired repetition rate should be 1 / M of the available digitizer bandwidth, where M is the stretching factor. Moreover, for continuous TS ADC the timing jitter constraint for the laser source is not relaxed and the jitter has to be in the 10 fs regime.

Thus, *a laser source having low amplitude and timing jitter source with repetition rates in the hundreds of megahertz regime* is required for time-stretch photonic analog-to-digital conversion. Also the laser has to have enough optical bandwidth in order to be able to fill the time interval between the pulses after the first stretcher and to make the wavelength demultiplexing easier by allowing wider wavelength periodicity of the filter.

The development of a low repetition rate semiconductor mode-locked laser is approached in three distinct ways:

- Improving on the noise performance of the Theta-cavity design by using an intra-cavity fiberized Fabry-Perot etalon
- Time demultiplexing of a high repetition laser
- External flattening of the stretched pulses coming from a Theta-cavity design source

Additionally, research conducted for the benefit of the aforementioned approaches is presented:

- High accuracy measurement of the free spectral range of a Fabry-Perot etalons using a narrow linewidth frequency swept laser source
- Measurement of the AM noise of periodic electrical signals and their mode partition noise

3.2 The Low Noise Theta Laser Swept Laser Source

3.2.1 Introduction

This work presents an approach for generating a frequency swept pulse laser using the laser cavity architecture named as the Theta laser with an intra-cavity Fabry-Pérot etalon. The Theta laser is based on chirped pulse amplification (CPA), which has been explored in the Ultrafast Photonics group for almost a decade. Thus, an introduction of the principles and the experiments that the current work is based upon, is presented. Section 3.2.2 briefly presents the results of previous work, while in 3.2.3 and 3.2.4 a blend of previously reported results is blended with new work. Sections 3.2.5 and 3.2.6 present the novel work of the student.

3.2.2 Extreme Chirped Pulse Amplification (X-CPA)

The basic principle in the development of the Theta laser is chirped pulse amplification (CPA) [59]. CPA was devised by the need to reduce nonlinear effects, and more specifically self-phase modulation (SPM), due to the high (peak) pulse power during amplification. CPA is used in the widespread master oscillator power amplifier (MOPA) system architecture, where a seed laser is used as a low power but high fidelity oscillator and the optical power is boosted in extra-cavity setups.

In most media, amplification of pulses with high peak power results in measurable, if not detrimental, second and third order nonlinearities, which lead into pulse broadening and breakdown. Thus, reducing the pulse power per unit volume and time in the gain medium reduces the induced pulse distortion and enables pulse recompression using linear dispersion elements.

One method for reducing the nonlinearity during optical amplification is by increasing the spatial mode profile of the pulses. The extracted energy per pulse, is enhanced by using higher order spatial modes. Some examples include inverse bowtie SOA [60], and tapered amplifiers that manage to access increased pulse energies [61] [62]. Nonetheless, the peak power of the optical pulses can still limit the maximum power that can be attained. Moreover, most applications favor fundamental mode operation and the management of the spatial mode profile can be limited by the mode size, if one wants to maintain high fidelity pulses.

Instead of the spatial stretching of the pulse mode profile used in the multi-spatial mode amplifiers, CPA uses temporal stretching to attain reduced peak pulse power. The pulses emitted by a short pulse laser are linearly stretched in time using a high dispersion element, reducing their peak power; they are subsequently amplified and recompressed using a complimentary dispersion element, as shown in Figure 3.1.

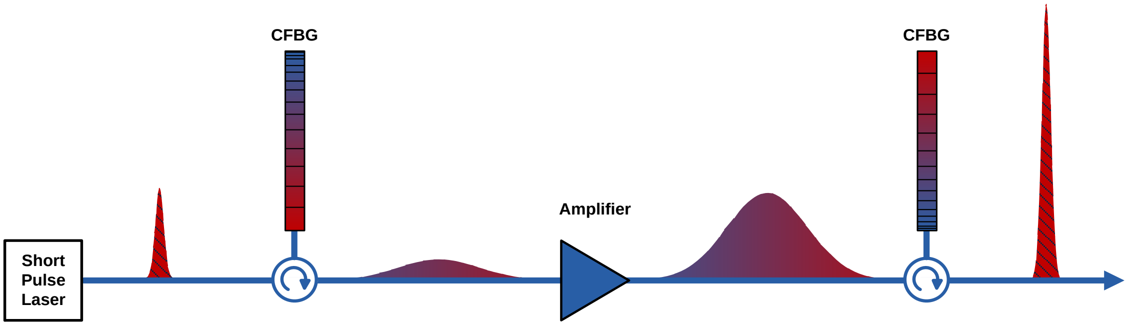

Figure 3.1. Chirped pulse amplification schematic.

The use of semiconductor gain in CPA systems has an added benefit compared to other commonly used gain media. Semiconductor media have electron-hole pairs as the energy carriers which show recombination lifetimes (τ_{rec}) in the order of a nanosecond [2]. Since the pulse durations range between sub-picosecond to multiple nanoseconds, the energy extraction from a semiconductor optical amplifier (SOA) depends strongly on the duration of the amplifying pulse. Pulses with temporal profiles shorter than τ_c deplete the energy stored in the gain medium during amplification, which limits the energy per pulse that can be extracted using a SOA. Nonetheless, if the pulses are stretched to time durations surpassing τ_{rec}, energy additional to the saturation energy is delivered to the SOA during amplification of a single pulse. Thus, for semiconductor-based CPA and pulse durations $\gg \tau_{rec}$, the energy that is added to a pulse upon amplification becomes proportional to its temporal duration [63, 64].

Extreme CPA (X-CPA) describes CPA schemes where the pulses tend to fill the time period between them. t-λ mapping fills the time between the pulses, thus X-CPA is the limit in which the energy per pulse extraction is optimized. X-CPA is experimentally demonstrated in this work in a MOPA system, as well as within a laser oscillator.

The rate equations that describe a medium's response to the temporal intensity profile and phase, as well as the rate equations that describe pulse propagation are [65, 66]:

$$P_{out}(\tau) = P_{in}(\tau) \cdot e^{h(\tau)} \tag{3.1}$$

$$\phi_{out}(\tau) = \phi_{in}(\tau) - \tfrac{1}{2} \cdot \alpha \cdot h(\tau) \tag{3.2}$$

$$h(\tau) = \int_0^L g(z,\tau) \cdot d\tau \tag{3.3}$$

$$\frac{dh}{d\tau} = \frac{g_0 \cdot L - h}{\tau_c} - \frac{P_{in}(\tau)}{E_{sat}} \cdot \left[e^{h(\tau)} - 1 \right] \tag{3.4}$$

$$E_{sat} = \frac{\hbar \cdot \omega_o \cdot \sigma}{a} \tag{3.5}$$

$$P_{sat} = \frac{\hbar \cdot \omega \cdot A}{\Gamma \cdot \gamma \cdot \tau_{rec}} \tag{3.6}$$

τ $(= t - \frac{z}{\upsilon_g})$ is the reduced time, υ_g is a group velocity, P is power, h represents the integrated gain at each point of the pulse profile, ϕ is the phase, α is the linewidth enhancement factor, g is the gain, τ_c is the carrier lifetime, E_{sat} is the saturation energy of the optical amplifier, σ is the mode cross section, a is the differential gain, A is the active region area, Γ is the optical mode confinement factor, γ is the differential gain, and τ_{rec} is the gain recovery time.

The simulations shown in Figure 3.2 demonstrate amplification in simulation and experiment, wherein pulses of variable time durations are amplified by an SOA [63].

Amplification of pulses with temporal duration of 1 ps simulates amplification of pulses typically emitted by semiconductor lasers, while amplification of 9.6 ns long pulses demonstrates the effect of X-CPA. The inherent advantage of using X-CPA over compressed pulse amplification for semiconductor gain media is revealed by the foremost enhancement in the extracted pulse energy.

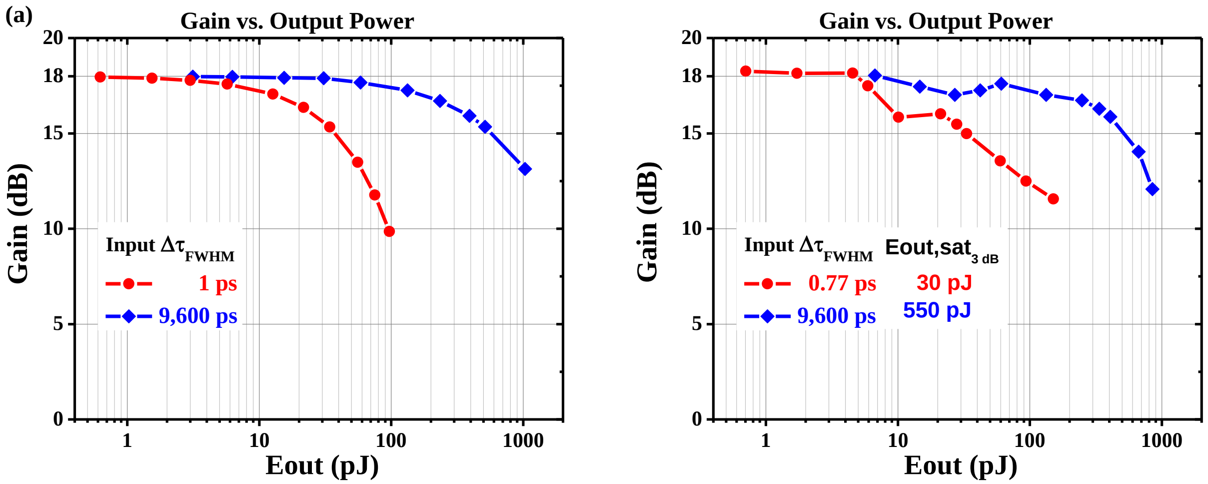

Figure 3.2. Comparison of energy per pulse in different amplification regimes; Short pulse amplification (Δτ = 1 ps) and X-CPA (Δτ = 9,600 ps) (a) Simulation with parameters: small signal gain = 18dB , saturation energy = 30pJ, and carrier lifetime = 600ps. (b) Experimental results. Note the increase of the energy per pulse for the X-CPA case [63].

Experiments conducted using short pulses from a 285 MHz colliding pulse mode-locked laser (CP-MLL) pulse picked to 96 MHz show a good agreement with the simulation [63]. The pulses are dispersed by ~14,000 times of their compressed duration (~1 ps) before amplification using a ridge waveguide SOA (RWGSOA). As presented in Figure 3.2 (b), the extracted energy per pulse reported is 550 pJ for the X-CPA scheme, while a mere 30 pJ for the amplification of the sub-ps pulses. This is an improvement of >18 times or >12 dB.

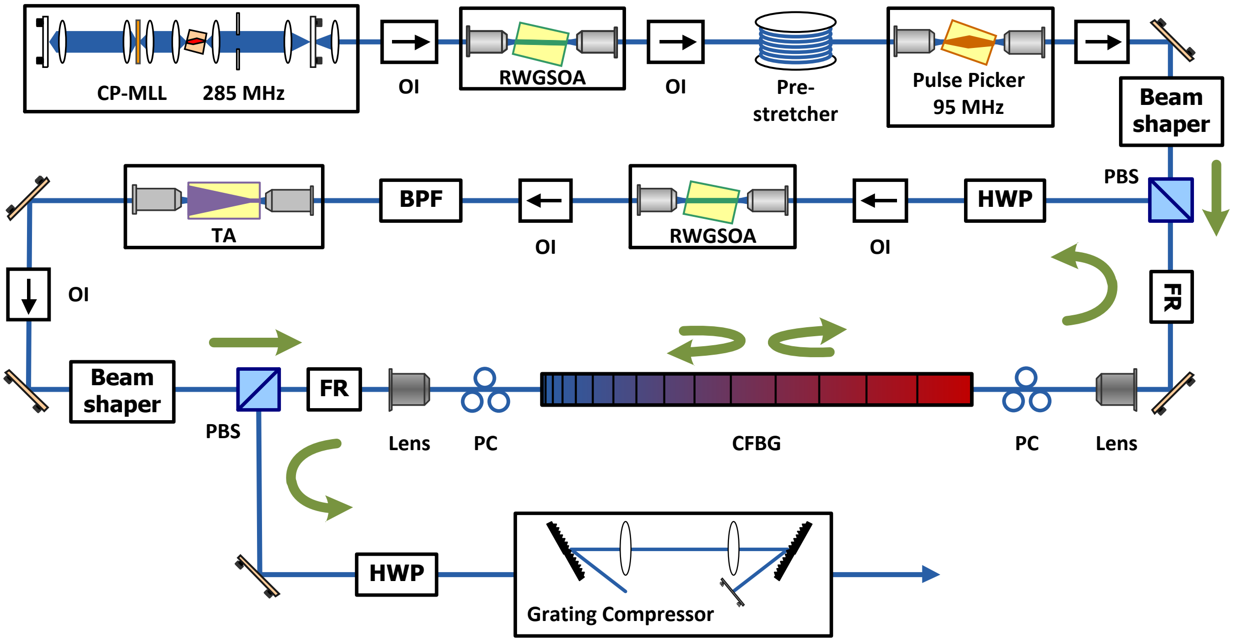

Figure 3.3. Schematic of the semiconductor extreme chirped amplification system. CP-MLL colliding pulse mode-locked semiconductor oscillator; OI, optical isolator; RWGSOA, ridge waveguide semiconductor optical amplifier; PBS, polarization beam splitter; FR, Faraday rotator; PC, polarization controller; CFBG, chirped fiber Bragg grating; HWP, half-wave plate; BPF, band-pass filter; TA, tapered amplifier. Adapted from [63].

A more elaborate X-CPA setup [63], was also implemented using the same CP-MLL as the seed. The pulses are pre-amplified and also pre-stretched using a fiber spool to ~150 ps before pulse picked to a third of their initial repetition rate. This allows for an enhancement of the extracted pulse energy, considering the CFBG available. After extreme stretching to ~9.6 ns the ~10 mW average power pulses are amplified twice, using a second pre-amplifier and a tapered amplifier to acquire an average power of ~1.4 W.

After recompression using the opposite port of the CFBG and a grating compressor the demonstrated average power is 228 mW which corresponds to 2.4 nJ of energy per pulse. The compressed pulse temporal duration of the autocorrelation trace is ~1.06 ps, which corresponds to pulse duration of 0.69 ps, assuming a hyperbolic secant pulse shape; This results to a peak power of ~1.4 kW. In a different amplification scheme where the repetition rate of the stretched pulses is further reduced, a record of ~1.6 μJ per pulse has been demonstrated for the uncompressed pulses [63].

Thus X-CPA can be used to access high energy-per-pulse from semiconductor amplifier. In the following section, X-CPA is used within a laser oscillator.

3.2.3 The Theta Laser – An X-CPA Laser Oscillator (X-CPO)

The concept of X-CPA is used to develop a laser oscillator named the Theta laser, derived from its architecture schematic. The Theta laser architecture uses X-CPA within the laser cavity to overcome the impediment of the semiconductor gain medium short carrier lifetime [67, 68]. In accordance to X-CPA, in the Theta laser cavity the pulses are stretched to durations much longer that the carrier lifetime, amplified, and subsequently recompressed on every round-trip. This results into a "breathing mode" operation for the laser pulses, and the pulses are stretched to the t-λ mapping regime within the laser oscillator. Dispersion is provided by a single CFBG, while the two directions of the grating are used to supply complimentary dispersion. The use of X-CPA in a ring laser oscillator has some noteworthy consequences as will be discussed in this section.

In the laser steady state, the pulses pass through the gain medium fully stretched in the same fashion as for the extra-cavity X-CPA experiments described in section 3.2.1. Nonetheless, the combination of X-CPA, which saturates the SOA, with the regenerative function of the laser results in uniform intensity frequency chirped pulses that fill the laser period. The laser does not follow pulsed amplification dynamics, but exhibits a quasi-CW amplification behavior, as expected for X-CPA. The generated chirped quasi-CW uniform intensity pulses are optimized for pulse energy extraction, since the temporal overlap of the pulse with the amplifier gain is maximized. Due to the t-λ mapping and for a given amplifier saturation power as defined by equation (3.6), the extracted energy per pulse becomes proportional to the time duration of the laser pulses. Since the pulses appear quasi-CW filling the period of the laser, the energy per pulse is proportional to the laser period, or the inverse of the laser repetition rate.

$$E_{pulse} = P_{sat} \cdot \Delta\tau_{pulse} \propto \frac{\Delta\tau_{pulse}}{\tau_{rec}} \propto \frac{1/f_{rep}}{\tau_{rec}} \tag{3.7}$$

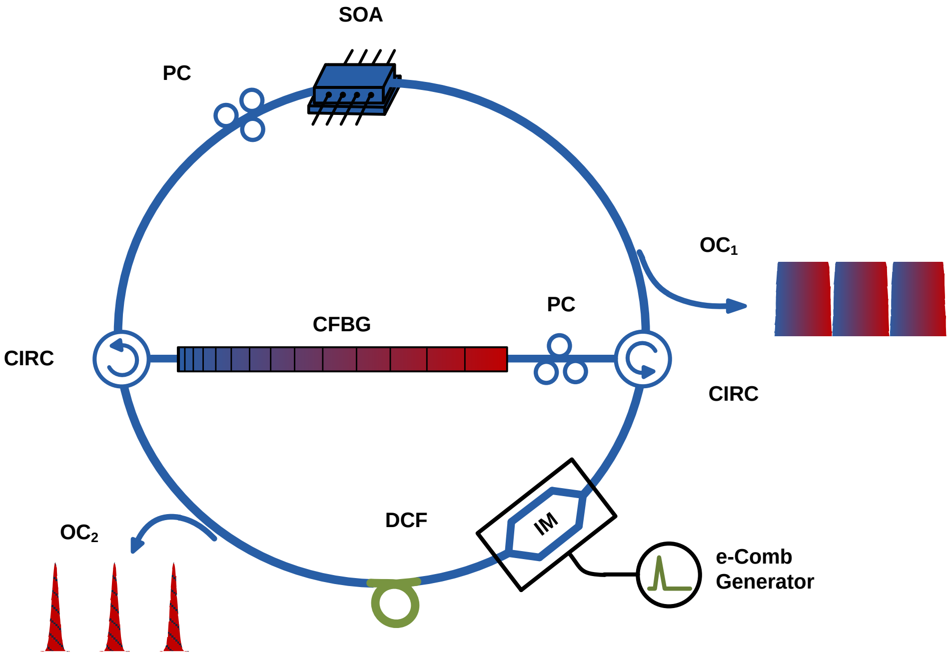

Figure 3.4. Schematic of the Theta laser. CFBG, chirped fiber Bragg grating; CIRC, optical circulator; IM, electro-optic intensity modulator; OC, output coupler; PC, polarization controller; SOA, semiconductor optical amplifier.

Moreover, since the pulses fill the period of the laser for a given dispersion of the CFBG, the lasing spectral bandwidth ($\Delta\lambda$) is predicted by a t-λ mapping calculation. This becomes the master equation for Theta laser oscillator architecture:

$$D_{CFBG} \cdot \Delta\lambda = \frac{1}{f_{rep}} = T \quad (3.8)$$
,

where D_{CFBG} is the CFBG dispersion, $\Delta\lambda$ is the uniform intensity spectral bandwidth, f_{rep} is the laser repetition rate, and T is the laser period.

Combinations for typical operational parameters for the Theta laser experiments presented in this work are presented in Table 3-1.

Table 3-1. Examples of Theta Laser Operation Characteristics

CFBG Dispersion (*ps/nm*)	Rep. Rate (*MHz*)	Spectral Width (*nm*)
2000	100	5.0
2000	33	15.2
1000	100	10.0
500	100	20.0
990	33	30.6

It should be noted that the Theta laser is an external cavity actively and harmonically MLL. Mode locking is attained via loss modulation using an intensity modulator driven by an electrical pulse generator. This is essential for imposing the X-CPA breathing mode dynamics to the laser. The temporal voltage profile of the electrical comb generator is shown Figure 3.5. The “window of opportunity” related to the temporal duration net cavity gain is in the order of 100 ps in temporal duration, although slightly longer gates can also be used.

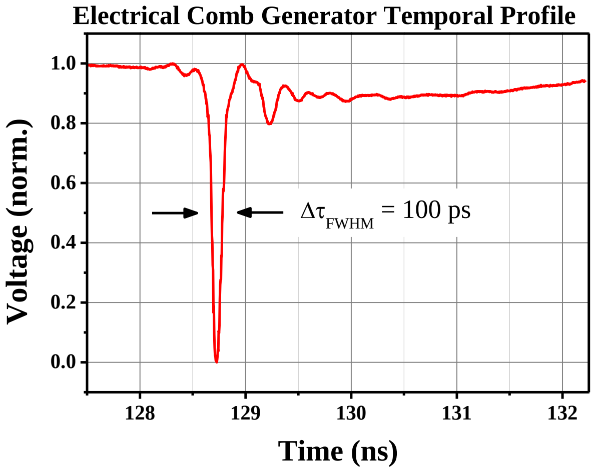

Figure 3.5. Sampling scope trace of the electrical comb generator temporal voltage profile. The full-width half maximum window duration is ~100 ps.

Another useful side-effect of the Theta laser is that it provides access to two different pulsed laser outputs; a primary port with quasi-CW linearly stretched pulses, and a secondary port with compressed pulses of few picosecond duration. The compressed laser pulses have increased energy per pulse compared to conventional laser cavity designs due to the X-CPA effect and they can be used for experiments needing high energies per pulse, clock distribution, optical sampling, metrology, etc.

The loss of the Theta laser as function of wavelength is shown in Figure 3.6. It should be noted that the laser has increased loss, due to the large number of components used in the X-CPA laser architecture. The laser cavity loss is in the order of 15.5 dB with decreased loss at the blue side of the spectrum. It should be noted that the SOA used has increased gain on the same wavelength range.

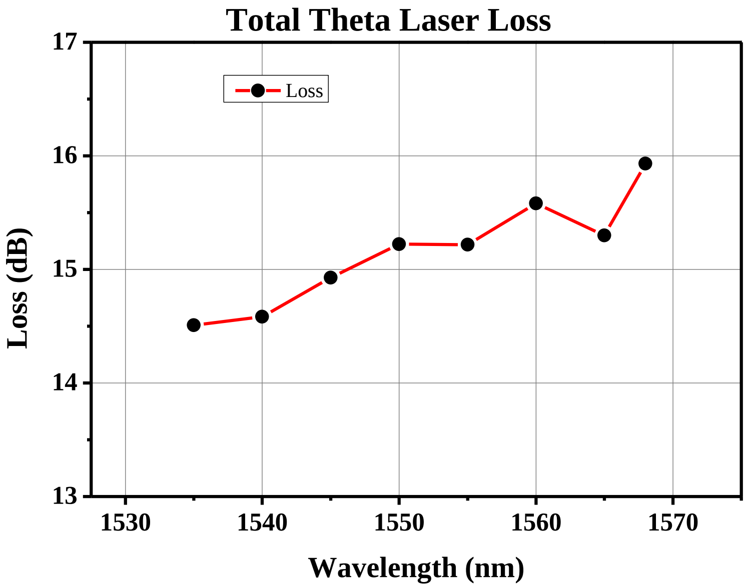

Figure 3.6. Theta laser cavity loss, as a function of wavelength.

3.2.4 Theta Laser Performance

Operation of the Theta laser oscillator cavity has been demonstrated from 2 GHz to 30 MHz Figure 3.7 shows the agreement of the experimental implementation of the Theta laser with equation (3.8) and verifies the prediction for scaling and enhancement of the pulse energy by semiconductor gain media in the Theta laser cavity design.

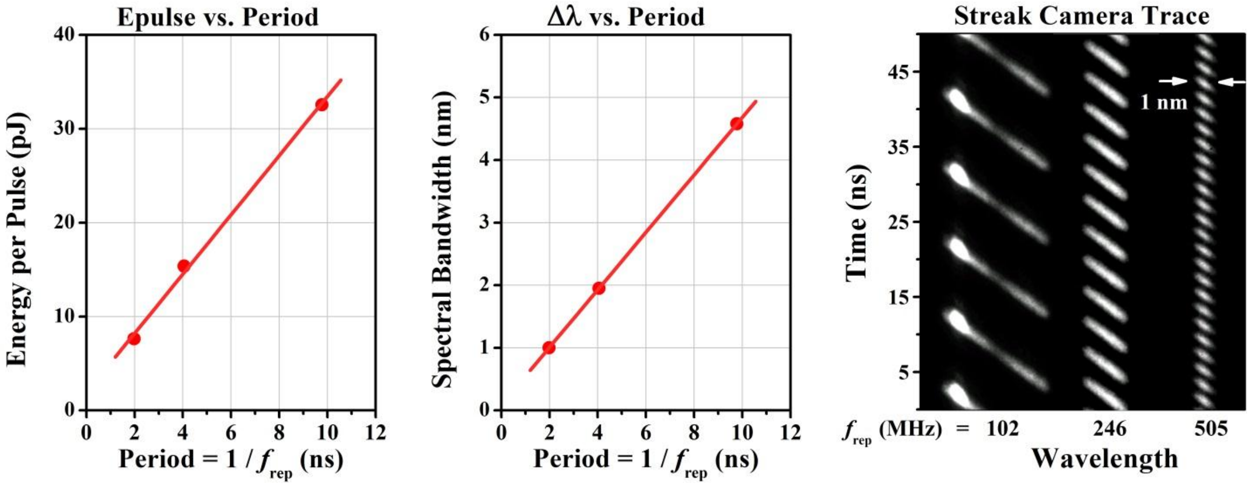

Figure 3.7. Theta laser characterization for different repletion rates using a common CFBG with D_{CFBG} = 2000 ps/nm (a) Energy per pulse scaling versus the laser period. (b) Laser bandwidth versus the laser period. (c) Streak camera traces. Adapted from [67].

Both the spectral bandwidth and the energy per pulse linearly increase as the laser repetition rate decreases, allowing for longer pulses due to the t-λ mapping and the filling of the laser period. Since the pulses appear as quasi-CW during amplification this behavior is not limited to the demonstrated repetition rates and even laser frequencies with higher pulse energies can be attained. Figure 3.7 (c) shows streak camera traces for the Theta laser for different operation frequencies for fixed grating dispersion. Spectral bandwidth scaling is observed, as well as the filling of laser period by the chirped pulses.

The same effect is observed in Figure 3.8, where equation (3.8) is verified for a fixed repetition rate. The optical bandwidth scales as a function of reverse CFBG dispersion.

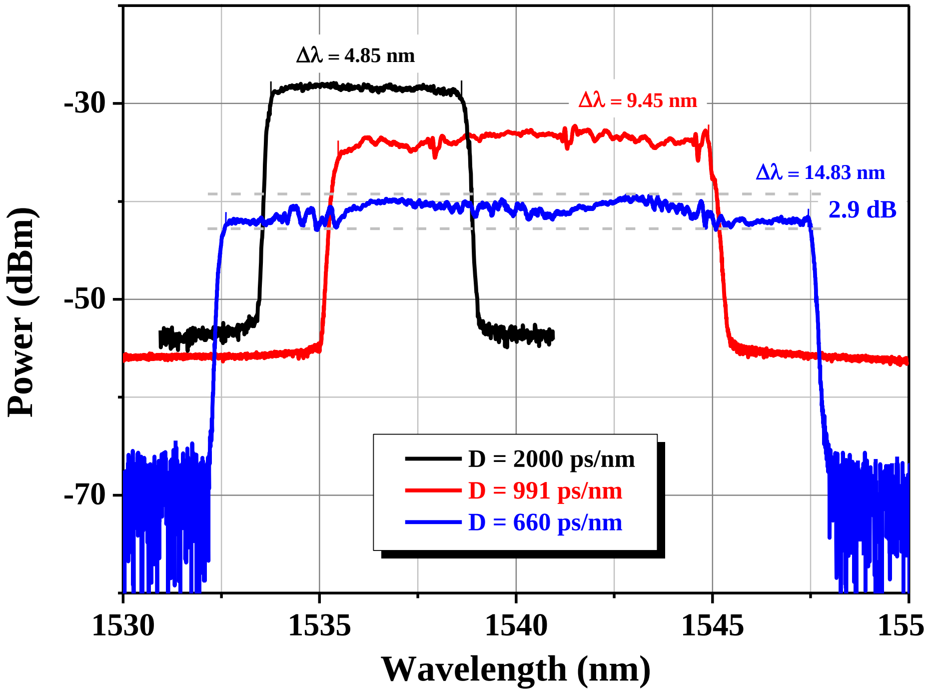

Figure 3.8. Theta laser optical bandwidth as a function of CFBG dispersion. A common repetition rate is used f_{rep} = 100 MHz. Note the linear scaling of the laser bandwidth with decreased CFBG dispersion.

It should be noted that the Theta laser enables the use of semiconductor gain media for pulsed operation at repetition rates that are inaccessible by conventional laser cavity architectures, which is a direct result of the amplifier being in saturation at all times due to the intra-cavity X-CPA effect of the Theta laser.

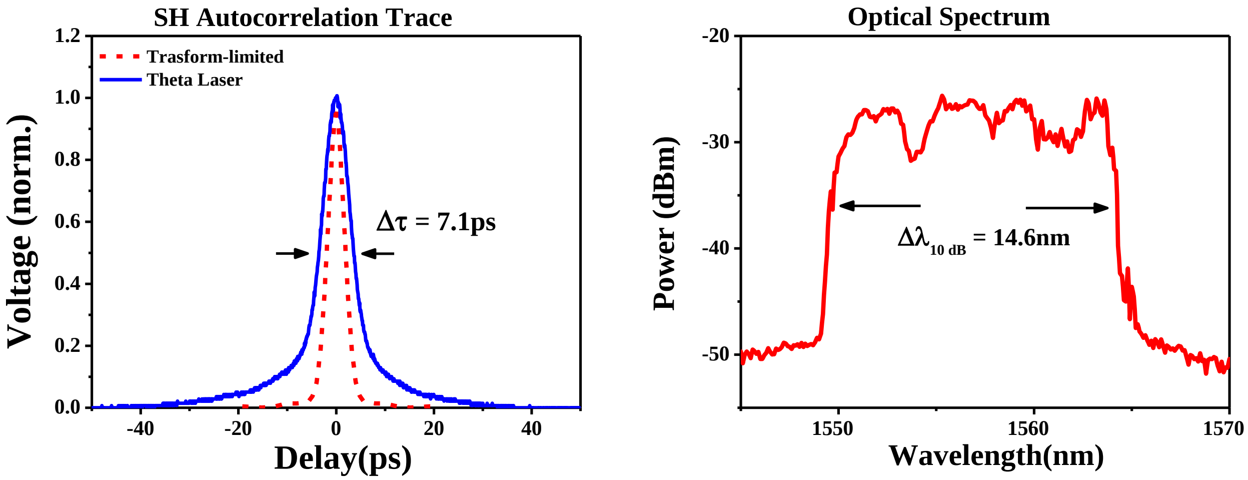

Figure 3.9. Theta laser characterization for 102 MHz repetition rate and 660 ps/nm grating dispersion. (a) Autocorrelation trace of the compressed port pulses, additionally compressed using a dual grating compressor. (b) Optical spectrum of the stretched port. Adapted from [67].

It should be noted that 33 pJ pulse energy is extracted by the laser operating at 102 MHz. The average power is ~3.36 mW, which can easily saturate additional amplifiers for further increasing the energy per pulse prior to compression. The dispersion of the CFBG used is 2,000 ps/nm. The compressed output port emits pulses that can be as much as 7.1 ps in time duration, close to two times the transform limited pulses corresponding to the optical spectrum (Figure 3.9 (a)).

The spectral bandwidth of the pulses can be increased to ~14.6 nm via the use of a CFBG with a reduced dispersion, retaining the repetition rate to ~100 MHz. When the repetition rate is also decreased by a factor of 3 (32 MHz), the spectral bandwidth triples.

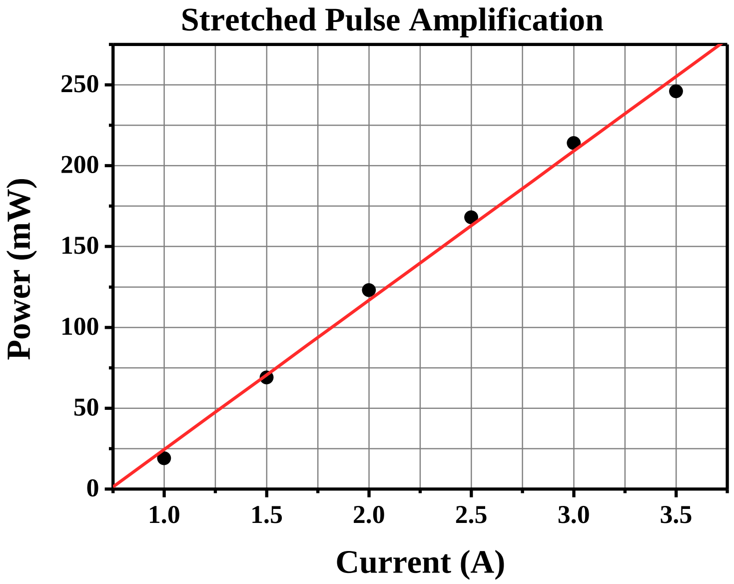

Figure 3.10. Stretched pulse amplification using a slab-coupled waveguide amplifier. Maximum power output P = 246 mW for a pump current of I =3.5 A.

Finally, although the pulses emitted by the laser's stretched port have a repetition rate in the order of ~100 MHz, due to their time-filling property they can still be amplified externally to the laser using an SOA. To demonstrate this, the Theta laser was operated with a repetition rate of 106.2MHz using a CFBG with dispersion of 2000ps/nm, emitting stretched pulses with an average power of 4.4 mW. When a SCOWA amplifier is used for stretch pulse amplification [69, 70], the pulses are able to extract the maximum power from the amplifier, since it operates under saturation due to the time filling pulse train. A maximum of 246 mW of average power is extracted for an injection current of I = 3.5 A. The corresponding pulse energy is 2.6 pJ.

3.2.5 The Theta Laser with an Intra-cavity Fabry-Pérot Etalon

The Theta laser is an external cavity actively and harmonically MLL, as discussed in 3.2.3. Mode locking is attained via loss modulation using an intensity modulator driven by an electrical pulse generator, as described in the previous section. The total length of the fiberized cavity is nominally on the order of 100 m and ~50 pulses circulate within the laser cavity. It is well known that harmonic operation of MLLs gives rise to noisy laser performance due to the limited correlation between the intra-cavity pulses, which is demonstrated as supermode noise spurs (SNS) in the RF spectra of the photodetected pulse train [71]. All interleaved optical modes can simultaneously lase, due to the lack of a selection mechanism. Furthermore, only modes separated by the laser repetition rate, equal to a harmonic of the cavity fundamental frequency, have increased correlation, which also results into a degradation in the noise performance of the laser.

The effect of the SNS in a harmonically MLL can be mitigated by increasing the homogeneity of the laser pulses [72]. A Fabry-Pérot etalon with a free spectral range (FSR) equal to the laser repetition rate, a harmonic of its cavity's fundamental frequency, can act as a mechanism that stores and inter-mixes the pulses. This is equivalent to filtering the unwanted interleaved optical mode groups attributed to the harmonic nature of the laser. The etalon's storage time must be sufficiently large, such as all the pulses are allowed to intermix, or equivalently the finesse of the etalon has to be large enough for the undesired optical modes to be filtered by the etalon. A schematic representation of the etalon function in both the time and frequency domains is depicted in Figure 3.11. Since the power distributed among all the interleaved mode groups is concentrated to the modes that correspond to the etalon FSR, the power per combline is expected to be enhanced by a factor of the harmonic of the laser, as depicted Figure 3.11 (c)-(d).

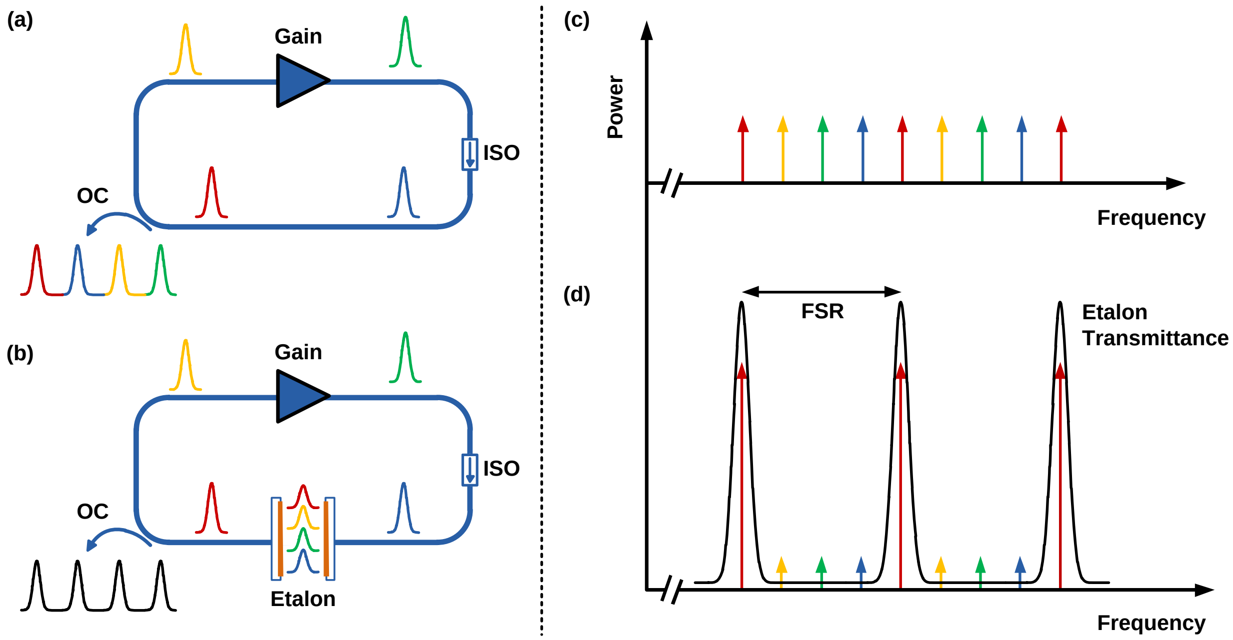

Figure 3.11. Intra-cavity etalon use for harmonically MLLs. (a)-(b) In the time domain explanation the etalon stores and inter-mixes the pulses resulting in an enhancement of intra-pulse homogeneity. (c)-(d) In the frequency explanation, the etalon filtering function suppressed the competing mode-groups associated with the harmonic nature of the laser. The depicted laser is operating at its forth harmonic. OC, output coupler; PBS, polarization beam splitter; ISO, optical isolator; FSR, free spectral range.

Suppression of the SNS has been demonstrated for conventional ring laser resonators operating at 10 GHz [72], and in a recent extension of this line of work, a 10 GHz spaced optical frequency comb was generated with excellent short and long term characteristics [73].

The etalons used in the aforementioned work are air-spaced and are assembled using curved mirrors and low expansion quartz spacers, corresponding to a mirror separation of 1.5 cm. For the scope of this work, the FSR needed for the etalon is 100 MHz, which makes the required mirror separation 100 times larger, or 1.5 m. Instead, a commercially available fiberized Fabry-Pérot etalon is used, constructed by two thin films connected to a dispersion shifted fiber with zero dispersion wavelength in the vicinity of 1550 nm.

Although fiberized etalons offer reduced laser design complexity and ease of use, compared to their free-space counterparts they suffer from FSR drift and increased susceptibility to acoustic and mechanical vibrations, as will be discussed later in this work. Moreover, fiberized etalons exhibit birefringence which is demonstrated as a minor difference in the FSRs for the two fiber polarization eigenstates. Nonetheless, the birefringence of the etalon is exploited to enable the use of an intra-cavity Hänsch-Couillaud (HC) scheme that provides an error signal for referencing the MLL to the etalon [74].

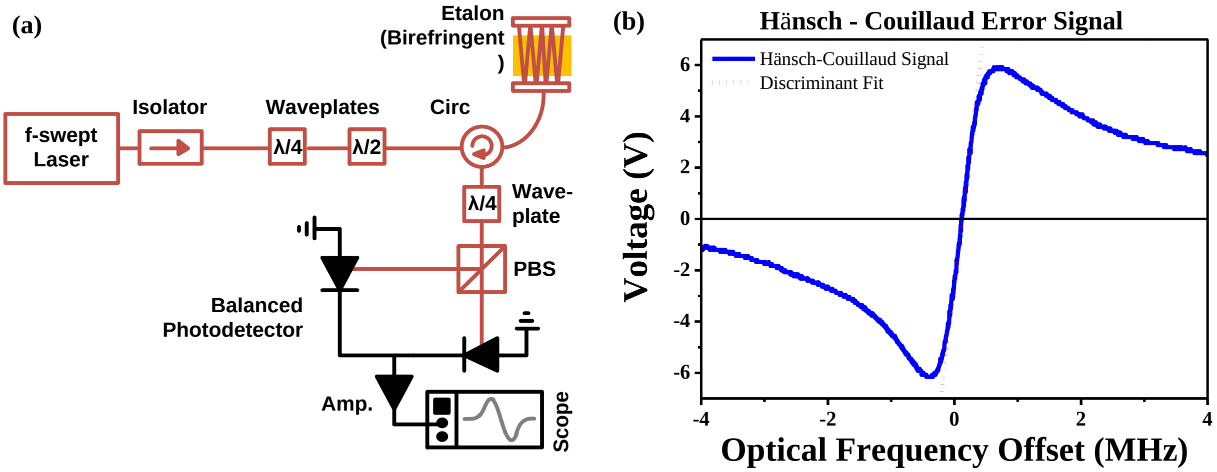

Figure 3.12. Typical Hänsch-Couillaud error signal generation (a) Setup schematic. (b) Error Signal. The linear part of the signal at the center of the resonance can be used for referencing. f-swept laser; narrow linewidth frequency swept laser (see Appendix); Circ, Circulator; PBS, polarization beam splitter; Amp., electrical amplifier.

Previous demonstrations of 10 GHz ring lasers referenced to intra-cavity etalons use the widespread Pound-Drever-Hall (PDH, [75]) technique, since the etalons used are based on free-space optics and do not demonstrate birefringence [72], [73]. In the PDH technique phase modulation on a CW laser results into a signal with a linear discriminant for the deviation of a CW laser from the center of a resonance. The signal driving the modulator is compared to the photodetected signal reflected by the etalon to generate the error signal [76].

On the other hand, the HC technique uses polarization multiplexing for the generation of the signal, enabled by the etalon birefringence. The two etalon polarization Eigen modes demonstrate different FSRs, due to the difference in optical path length. HC uses one of the polarization states as the phase reference, due to the mismatch of the etalon transmission windows for the two polarization states.

The HC scheme has an inherent advantage over the PDH technique in that it consists of fewer and solely passive components. On the other hand, the useful linear part of the HC error signal is approximately half in slope of its PDH counterpart resulting into a somewhat looser lock [77]. An extra-cavity HC signal generation schematic depicted in depicted Figure 3.12, accompanied by the error signal generated. The etalon measured is the same as the one used in the Theta laser results presented in this section. For reference, the linear part of the generated signal has a discriminant with a slope of ~2.1 V/MHz, which corresponds to the voltage differential per MHz of optical frequency deviation.

When referencing the Theta laser to the intra-cavity etalon, all the lasing modes contribute to the generation of the error signal. The number of the ~100 MHz-spaced modes is in the order of 12,000, for 10 nm of lasing bandwidth. Mismatch of the cavity-supported modes with the etalon modes due to dispersion and active frequency drive mismatch results in a broadening of the error signal, which is demonstrated as increased signal noise. This effect is experimentally used for fine tuning the active drive frequency.

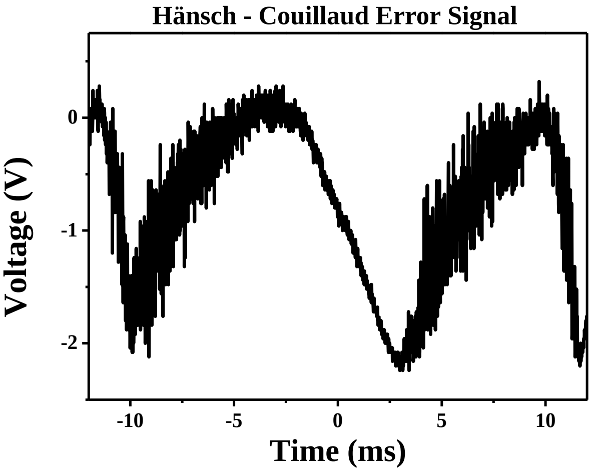

Figure 3.13. Intra-cavity Hänsch-Couillaud error signal from the Theta laser generated using a linear cavity length sweep. It should be noted that all the lasing modes contribute to the generation of the signal.

Consequently, another important experimental design parameter for the Theta laser is interplay between the dispersion of the cavity and that of the etalon. Since the fiberized etalon has reduced but measurable dispersion, (<2 ps/nm/km), the modes of the etalon are not evenly spaced in frequency. Therefore, the dispersion of the fiberized laser cavity must match the dispersion of the etalon in order for the modes supported by the laser cavity to overlap with the etalon transmission windows. If laser dispersion is not experimentally addressed the lasing bandwidth is reduced and the stretched port time intensity profile does not appear as quasi-CW. In the work presented here, 8 m of dispersion compensating fiber balances the laser cavity dispersion to that of the etalon.

It should be noted that since the Theta laser is an actively MLL, the electrical pulse generator must be driven at the appropriate frequency, which for this work is the FSR of the etalon. Thus the frequency corresponding to the etalon FSR must be known with high precision. This problem is addressed in the Appendix, where an ultra-high precision measurement of the etalon properties is presented [78].

3.2.6 Theta Laser with Intra-cavity Etalon Performance

A schematic of the Theta laser with the intra-cavity etalon is shown in Figure 3.14. The developed Theta laser has a repetition rate equal to the FSR of the fiberized etalon, which is: $f_{\mathrm{rep}} = \mathrm{FSR}_e = 99.580$ MHz. The dispersion of the commercially available CFBG used is 990 ps/nm. It should be noted that linearly chirped pulses having uniform time intensity profiles that fill the period of the laser, correspond to optical spectrum that similarly has a uniform, square-shaped intensity profile with bandwidth of 10.1 nm.

Figure 3.15 shows the characterization of the compressed port output of the Theta laser described above. The sampling scope trace of the laser is depicted in Figure 3.15 (a). Pulses of ~30 ps in duration are measured with a ~10 ns period, resulting in a duty cycle <0.3%. There are no satellite pulses and the extinction demonstrated is high. It should be noted that high quality MLL operation with duty cycles in this range cannot be attained using conventional cavity designs for semiconductor-based lasers at this repetition rate regime.

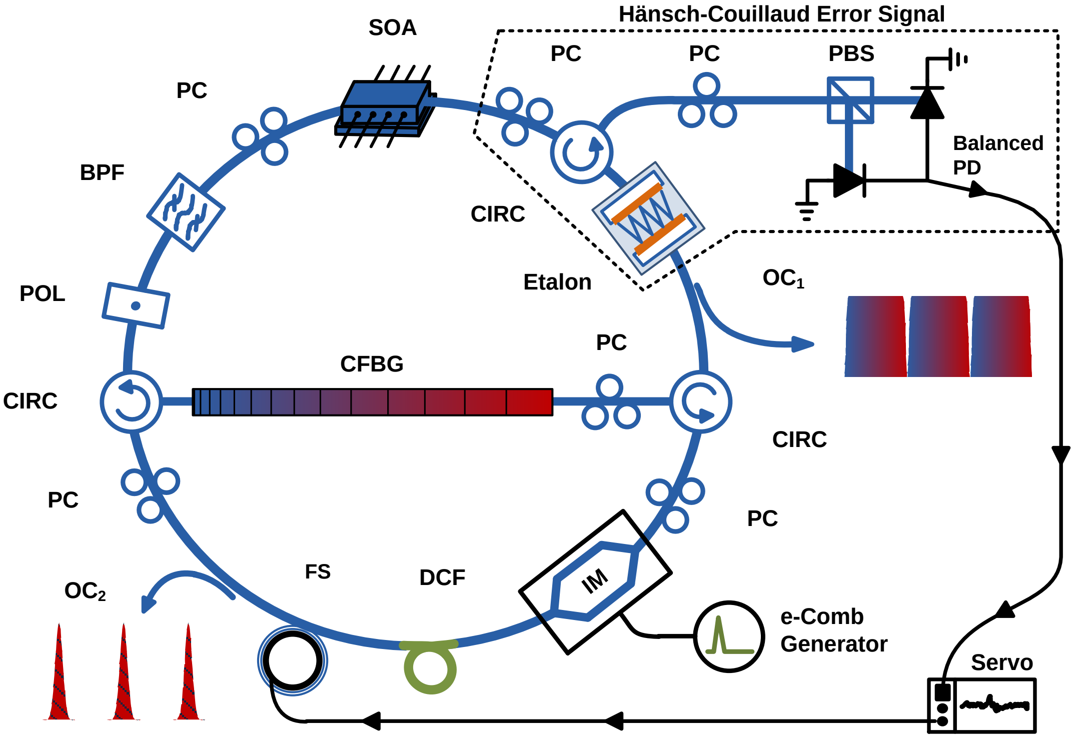

Figure 3.14. Schematic of the Theta laser with an intra-cavity etalon and long-term referencing. BPF, optical band-pass filter; CFBG, chirped fiber Bragg grating; CIRC, optical circulator; DCF, dispersion compensating fiber; FS, fiber stretcher; IM, electro-optic intensity modulator; OC, output coupler; PBS, polarization beam splitter; PC, polarization controller; PD, photodetector; POL, polarizer; SOA, semiconductor optical amplifier.

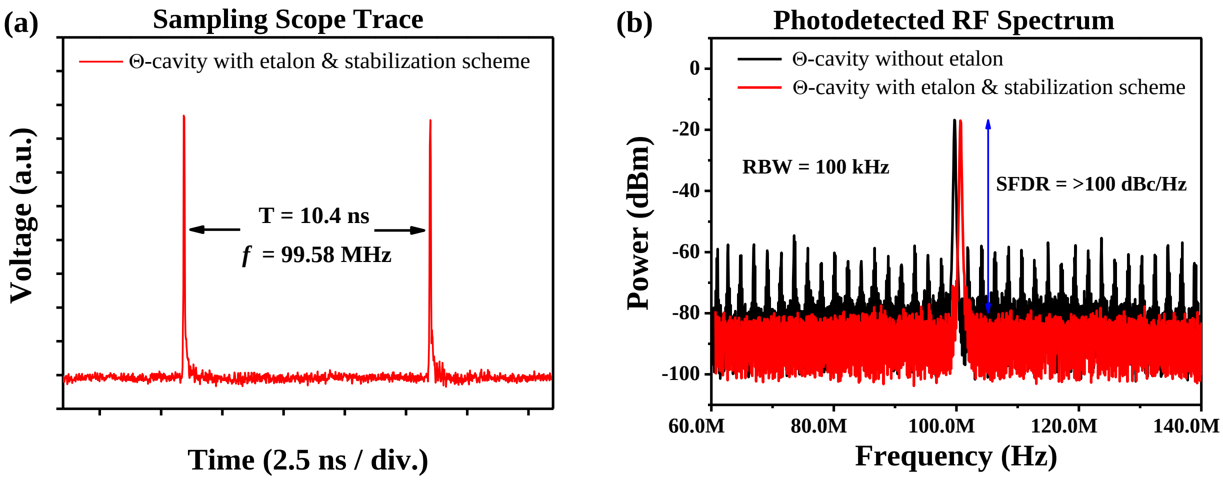

Figure 3.15. Characterization of the compressed-port pulses. (a) Sampling scope trace acquired using a 15 GHz photodetector. (b) Photodetected RF spectrum. Note the absence of the supermode spurs on the red spectrum due to the filtering by the etalon. (The red spectrum has been shifted for viewing purposes).

In the following figures the black trace depicts the results for the Theta laser operating with all the components shown in Figure 3.14 except for the fiberized etalon, while red depicts results for the complete system with the long-term stabilization scheme employed. SNS are observed in the black trace, owing to the harmonic nature of the laser. When the etalon is inserted in the laser cavity and the long-term stabilization scheme is employed the etalon's inter-

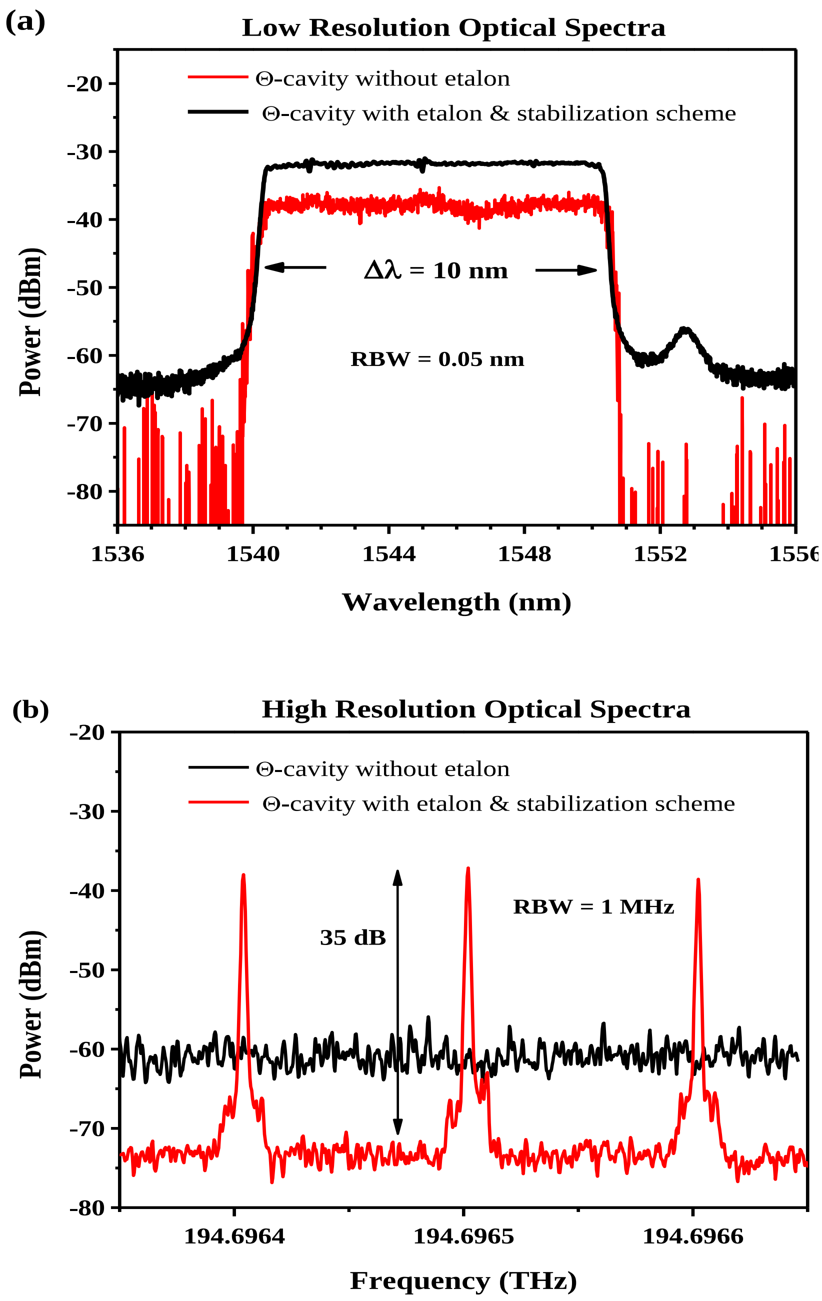

Figure 3.16. Optical spectra of the Theta laser's stretched port. (a) Wide span optical spectra with and without the intra-cavity Fabry-Pérot Etalon. (b) High resolution optical spectra. Note the generation of the optical frequency comb due to the intra-cavity etalon. (The sidebands tones are artifacts of the measurement).

mixing function leads to the suppression of the SNS. The demonstrated suppression is in excess of 10 dB and the SNS are suppressed below the noise floor of the instrument. The RF tone at the laser's repetition rate has spur-free dynamic range in excess of 100 dBc/Hz.

Figure 3.16 shows the spectral characterization of the stretched port of the Theta laser. On the optical spectra of Figure 3.16 (a), acquired using a conventional optical spectrum analyzer, the spectral uniformity of the laser is ~1 dB, while it reduces to 3 dB for the laser with the intra-cavity etalon. Suppression of the undesired spontaneous emission by the etalon is measured to ~10 dB. Careful dispersion compensation of the ~100 meter-long laser cavity enables lasing at the full supported bandwidth even with the use of the Fabry-Pérot etalon, as calculated using equation (3.8). The laser pulses shown in Figure 3.17 are linearly chirped and the time intensity profile of the stretched port appears continuous.

The high resolution spectra presented in Figure 3.16 (b) present a critical effect of the insertion of the etalon in the Theta harmonically MLL. Due to the filtering function of the etalon, the unwanted optical comblines owing to the harmonic nature of the laser are suppressed and a frequency comb with spacing equal to the active drive frequency and the FSR of the etalon is generated. Using the etalon, the power distributed every ~50 optical modes is concentrated in a single combline. To the authors' knowledge this is the first demonstration of a stable optical frequency comb generated using a semiconductor based laser in the 100 MHz regime. The combline contrast measured is in excess of 35 dB, while the power output is 2.0 mW for the stretched port and 0.4 mW for the compressed port.

The temporal characteristics of the stretch output port is depicted in Figure 3.17. The t-λ mapping is apparent in comparison with the optical spectrum shown in Figure 3.16 (a). Also it should be noted that the pulses cover the period of the laser appearing as quasi-CW. The fast modulation on the spectrum is due to manufacturing errors of the CFBG, as will be discussed in the Appendix.

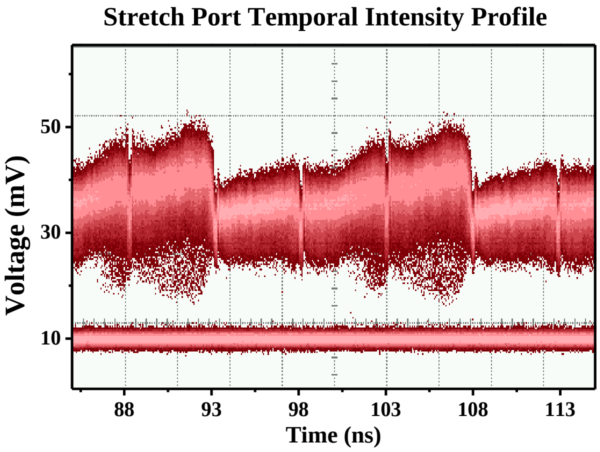

Figure 3.17. Temporal intensity profile of the stretched port photodetected output acquired using a sampling scope. Photodetector bandwidth = 25 GHz.

All potential applications for the Theta laser put stringent requirements for the pulse energy fluctuation of the pulses. The inhomogeneity of the pulses in the simple Theta cavity due to its harmonic nature and the excess noise of the electrical pulse generator drive lead in excess noise for the laser pulses. This is shown in Figure 3.18 (a), where the laser noise is measured using an Agilent E5500 noise testset. The solid lines show the power spectral density (PSD) of the amplitude noise for the laser with and without the etalon, while the lighter traces show the integration giving the pulse-to-pulse energy variance. The relative pulse energy variance (ΔE/E) for the full band is ~1% for both cases.

However, a significant difference is observed for the frequency offset range containing the SNS [2 MHz, 20 MHz], where an improvement of 20 times from ~1% to ~0.05% is calculated. Moreover, one can see an increase in the noise PSD at low offsets, which can be explained by considering the fact that the laser cavity is referenced to the fiberized etalon. For frequencies within the servo mechanism's operating speed the laser follows the fiberized etalon, thus the laser is susceptible to its noise and thermal drift. Also, there is a spike in the PSD at 11.5 kHz due to the resonance of the piezo drum used for referencing the cavity length to the etalon. Since, the aforementioned applications use signals with durations shorter than 10 ms, the appropriate noise integration band starts from 100 kHz and ends at the Nyquist frequency of the pulses, (49.79 MHz). Thus, the use of the fiberized etalon offering significant suppression of the SNS is advantageous for use with the Theta cavity, enabling its use in low noise applications.

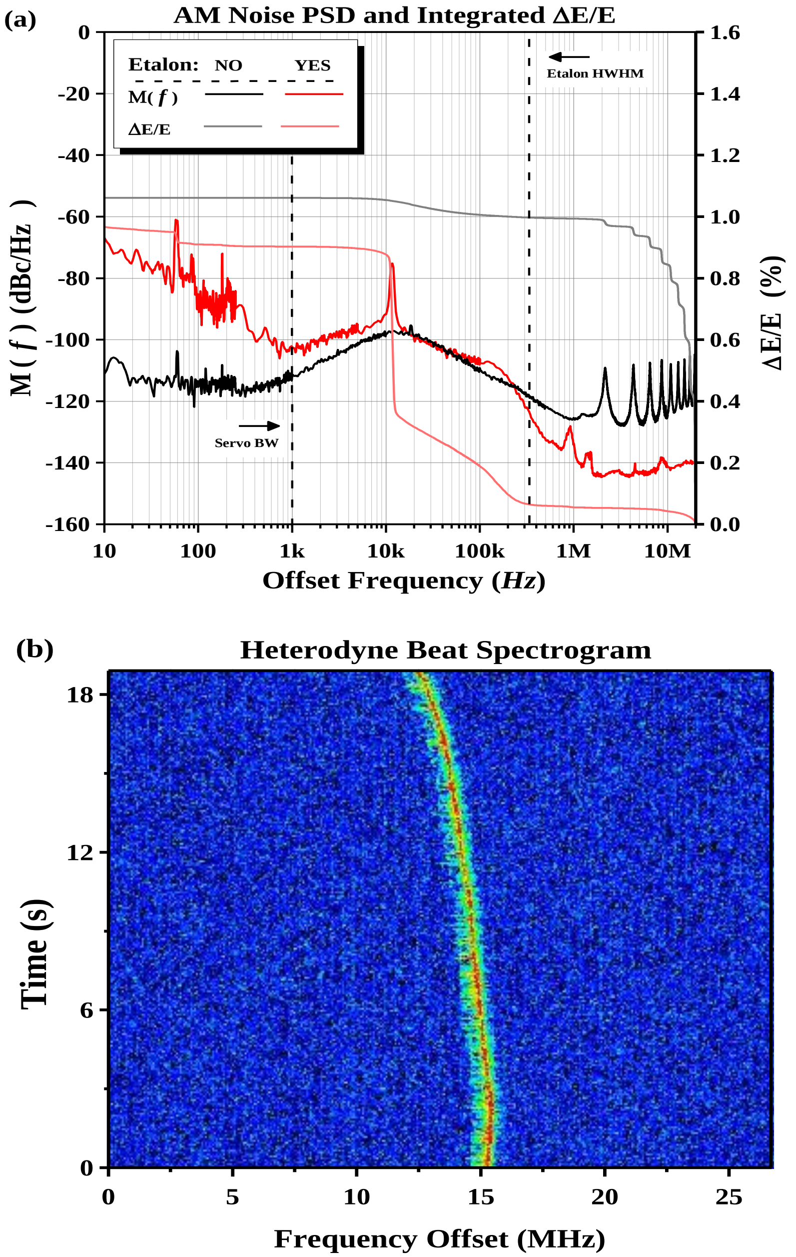

Figure 3.18. (a) Power spectral density of the AM noise of the laser with and without the etalon. The supermode noise spurs are suppressed by >30 dB. The etalon's half width half max (HWHM) is marked. (b) Spectrogram of the heterodyne beat between a single combline of the Theta MLL and a narrow linewidth laser.

A heterodyne beat of one of the laser comblines with a commercially available laser with linewidth 1 kHz is presented in Figure 3.18 (b). The beat tone drifts monotonically by 3 MHz during a measurement of 18 s. This behavior is explained by taking into consideration the fact that the laser is referenced to a fiberized etalon. As discussed in the Appendix [78], the FSR of the etalon drifts in time and so will the optical frequency comb of the Theta laser. Moreover, the etalon’s FSR is affected by acoustic and mechanical noise and special care was taken to isolate the laser components and especially the etalon from room noise. The laser components are in nested acrylic boxes with a foam insulation layer in between. As a result of the etalon drift and noise response, this specific Theta laser implementation cannot be characterized with the pure definition of a frequency comb source. Nonetheless, if a better reference were used, better long term stability would be attained, and a semiconductor-based 100 MHz optical frequency comb could be realized.

Typical autocorrelation traces from the pulses from the compressed port of the Theta laser, amplified with an Erbium-Doped Fiber Amplifier (EDFA), are presented in Figure 3.19. A coherence spike is observed for in the traces for both cases with and without the etalon in the laser. This can be a consequence of increased Amplified Spontaneous Emission (ASE) from the Theta laser or a coherence break across the optical spectrum of the laser. The latter can be explained by the spectral modulation of the residual group delay in a round-trip due the manufacturing imperfections of the CFBG used. This effect is discussed in the Appendix.

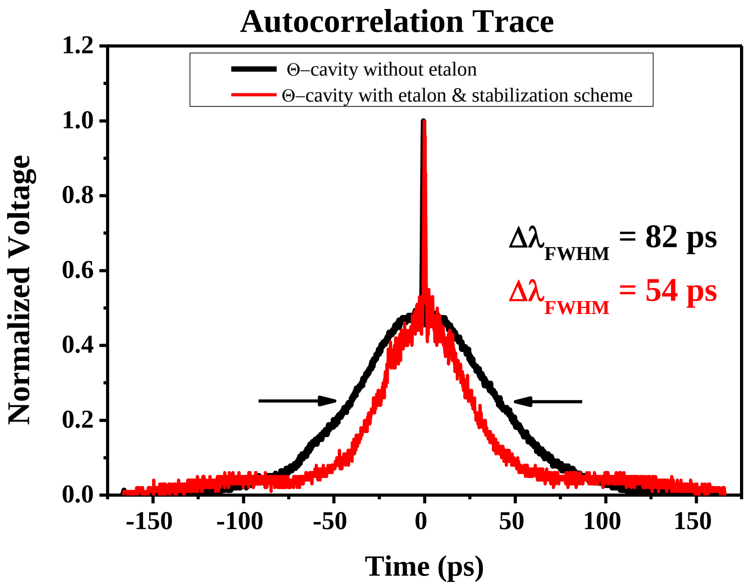

Figure 3.19. Compressed port second harmonic port autocorrelation trace for typical operation of the Theta laser, lasing at with the maximum supported optical bandwidth.

When the Theta laser with the intra-cavity etalon is made to lase at a smaller bandwidth, the coherence spike disappears, as did for the case without the etalon. The measurements are depicted in Figure 3.20, where the autocorrelation trace and the corresponding optical spectrum are shown. The 10 dB spectral bandwidth is <0.3 nm.

Remember that the CFBG has a dispersion of 990 ps/nm, which corresponds to spatial differential in the reflection of ~20cm/nm. The lasing bandwidth implies that the laser operates better when it is using a minimal region of the CFBG.

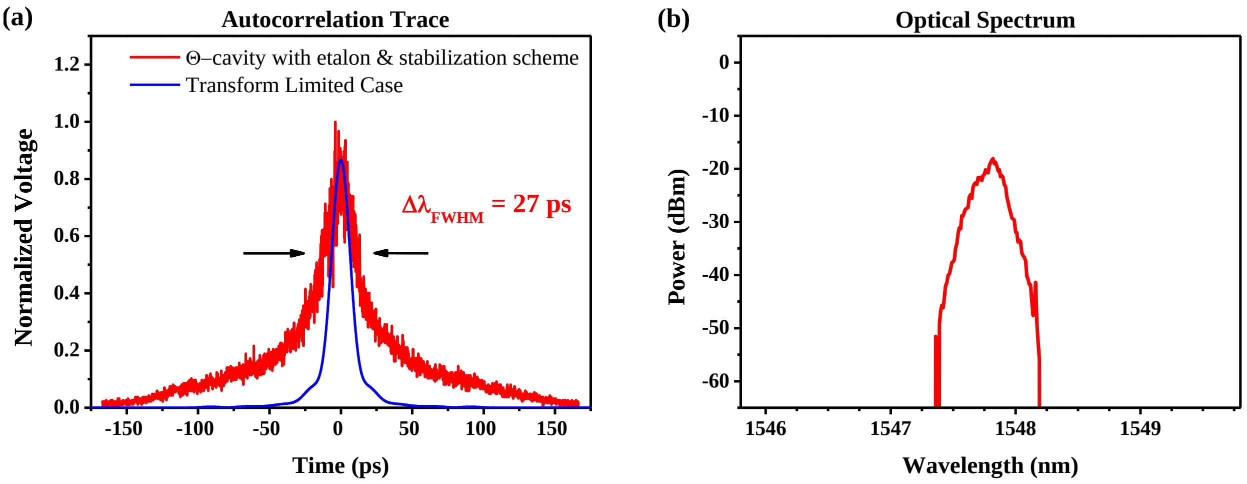

Figure 3.20. (a) Compressed port second harmonic port autocorrelation trace for the Theta laser with the intra-cavity etalon, when lasing at narrow spectral bandwidth. (b) Optical Spectrum.

3.2.7 Conclusion on the Theta Laser with Intra-cavity Etalon

This section presented an extensive report of the development of the Theta laser with intra-cavity selection mechanism. A fiberized etalon is used as an intra-cavity optical filter to suppress the SNS related to the harmonic nature of the laser. Low noise performance is demonstrated with a long-term stabilization scheme.

Compared to the chirped pulse generation techniques discussed in section 2, the Theta laser has the following advantages:

- Fast repetition rate. The mechanically swept sources described are limited due to inertia to few kHz repetition rates. Moreover, laser cavity built-up times also limit the sweep speed [9]. The Theta laser's breathing mode results in quasi-CW frequency chirped laser pulses demonstrated from 32 MHz to 2 GHz.

- Enhanced frequency chirp linearity due to t-λ mapping. The Theta laser pulses are compressible to sub 100 ps. No external calibration is needed for the time axes.
- The pulses fill the laser period appearing as quasi-CW. Continuous data acquisition can be possible.
- The laser is operating at the steady state. The moving part lasers demonstrated are limited by the laser build-up time.
- The Theta laser pulses have enhanced power which is related to the SOA's saturation power, while the ASE is strongly suppressed. The pulses can be easily amplified externally to the laser cavity.

The following section describes a high precision characterization of the etalon used in the Theta laser, which was essential in the laser development.

3.3 Characterization of the Free Spectral Range of a Fabry – Perot Etalon with Sub-Hz Precision

3.3.1 Section Abstract

In this work a narrow linewidth (1 kHz) laser source is used to measure the free spectral range (FSR) of a fiberized Fabry-Perot etalon with sub-Hz accuracy (10^{-8}). A previously demonstrated technique based on the Pound-Drever-Hall error signal is improved in precision by the use of a narrow linewidth laser swept in frequency via an acousto-optic modulator, or single sideband generation. The sub-Hz (10^{-8}) precision attained enables the characterization of both the long-term drift and the polarization dependence of the free spectral range of the fiberized etalon.

3.3.2 Introduction

Fabry-Perot etalons are multi-interference optical resonators having a periodic in frequency amplitude and phase response. In the past years the advancement of thin film and micro-toroid technologies have enabled the development of optical resonators having both high finesse ($\mathscr{F}$) and large frequency separation of successive resonances, or free spectral range (FSR) [79]. Etalons have been used to reduce the linewidth of lasers [80], for frequency multiplication of low repetition rate pulse trains [81], for astronomical instrument calibration [82], to suppress the timing jitter of harmonically mode-locked lasers [83], and recently to improve the performance of optoelectronic oscillators [84].

In most cases, it is advantageous to reference at least one optical tone to the etalon, or vice versa. This is performed by generating an error signal and feeding it back to either alter the frequency of the optical tone, or the center frequency of the resonator. Multiple setups have been demonstrated for the generation of the error signals. Referencing techniques include polarization-based effects [85] and spatial mode interference [86]. Yet, the most widely used cavity referencing mechanism uses phase modulation sidebands on the optical tone; it is called the Pound-Drever-Hall (PDH) technique [87], [88].

For most applications based on optical resonators, precise knowledge of the FSR is required. Most FSR measurement techniques make use of the intensity response of etalons (Fig. 1(a)), which have a flat response for small deviations from the center of the resonance [89], [90]. On the other hand, a technique based on a modified PDH error signal has been demonstrated with accuracy of 1 part in 10^4 [91]. The measurements performed were limited by the linewidth of the probing laser and the finesse of the etalon used.

In this work, the performance of the modified PDH technique described in [91] is analyzed revealing the requirement of a narrow linewidth frequency swept laser. This is achieved by incorporating a 1 kHz linewidth laser swept in frequency using an acousto-optic modulator (AOM). The developed scheme is used for the measurement of the FSR of an etalon with sub-Hz (10^{-8}) accuracy. The high accuracy achieved enables the experimental measurement of both the polarization dependence of the FSR and its long-term drift.

3.3.3 The Pound-Drever-Hall Technique for Free Spectral Range Measurement

In the PDH technique a phase modulator (PM) is driven at a fixed frequency generating sidebands of opposite phase. The PDH error signal is formed when the frequency of the laser along with the phase modulation sidebands are swept through an etalon resonance. Upon reflection from the etalon the central optical tone experiences nonlinear amplitude and phase response, while the optical sidebands are used as a reference, as by the etalon's frequency response depicted in Figure 3.21 (a). The reflected signal is photodetected and subsequently down-converted to the baseband using a frequency mixer and a low pass filter. The error signal generated is given by the formula:

$$V(\nu,\varphi)=\frac{\mathrm{I}_0\cdot\beta\cdot\eta\cdot M\cdot G\cdot \mathrm{R}}{2}\cdot\mathrm{Re}\left\{\left[R(\nu)\cdot R^{*}(\nu+f_{PM})-R(\nu)^{*}\cdot R(\nu-f_{PM})\right]\cdot e^{i\cdot\varphi}\right\}, \quad (3.9)$$

$$\text{where}\quad R(\nu)=\frac{r\cdot\left(e^{i\cdot 2\cdot\pi\cdot\nu/FSR}-1\right)}{1-r^{2}\cdot e^{i\cdot 2\cdot\pi\cdot\nu/FSR}}. \quad (3.10)$$

and ν is the frequency of the laser, f_{PM} is the phase modulation frequency, φ is the phase mismatch of the electrical arms at the mixer, * denotes the complex conjugate, I_0 is the optical power, β is the depth of modulation, η is the photodetector efficiency, M is the mixer conversion gain, G is the amplifier gain, and R (= 50 Ω) is impedance. The proportionality constant in (3.9) does not affect the shape of the error signal. R is the etalon electric field reflection coefficient and r the mirror field reflectivity, assuming identical etalon mirrors. Typically, the PDH error signal used in referencing is generated by using $\varphi = 90^{\circ}$ and modulation frequency at 10-40% of the FSR. The generated error signal has a sharp discriminant at its center [88].

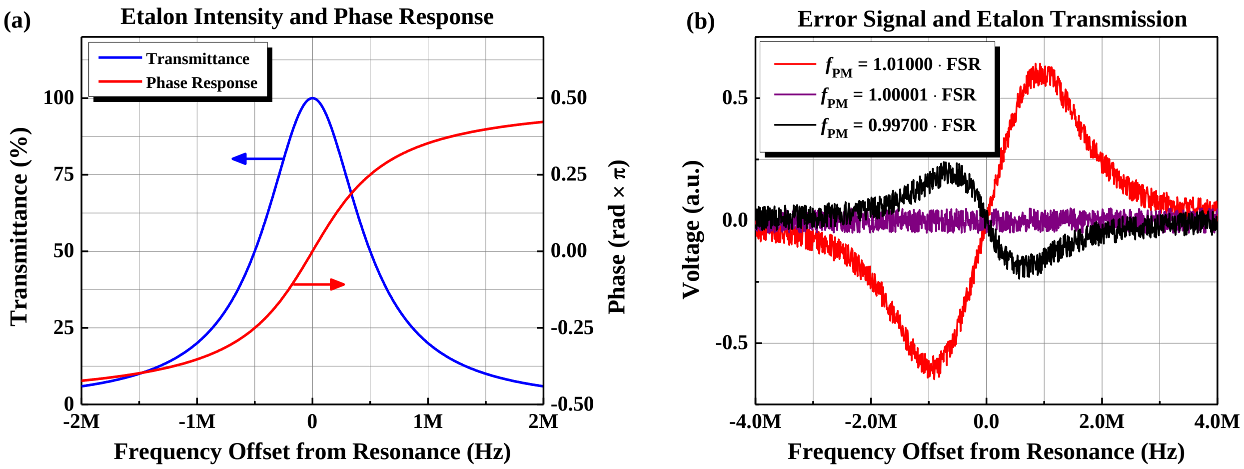

Figure 3.21: (a) Power and phase response of the transmitted beam as a function of the optical frequency. (b) Simulation of the Pound-Drever-Hall error signal for an etalon having FSR = 100 MHz and $\mathscr{F}$ = 100. Error signal voltage generated using phase modulation frequencies in the proximity of the etalon FSR. The simulation includes the effect of electrical noise with amplitude of 0.05 V.

In the case of the FSR measurement first described in [91], the error signal is observed as the modulation frequency is tuned for a phase mismatch $\varphi = 0^{\circ}$. When the modulation sidebands are within the adjacent resonances of the etalon the PDH error signal resembles the shapes shown in the simulation in Figure 3.21 (b), which incorporates the effect of electrical noise with amplitude of 0.05 V. It should be noted that the shape of the error signal is preserved as the modulation frequency is varied through the FSR frequency, but it changes in amplitude. Specifically, Figure 3.22 shows that the error signal vanishes when the modulation frequency matches the FSR and changes sign around the resonances. This effect is used for the measurement of the FSR.

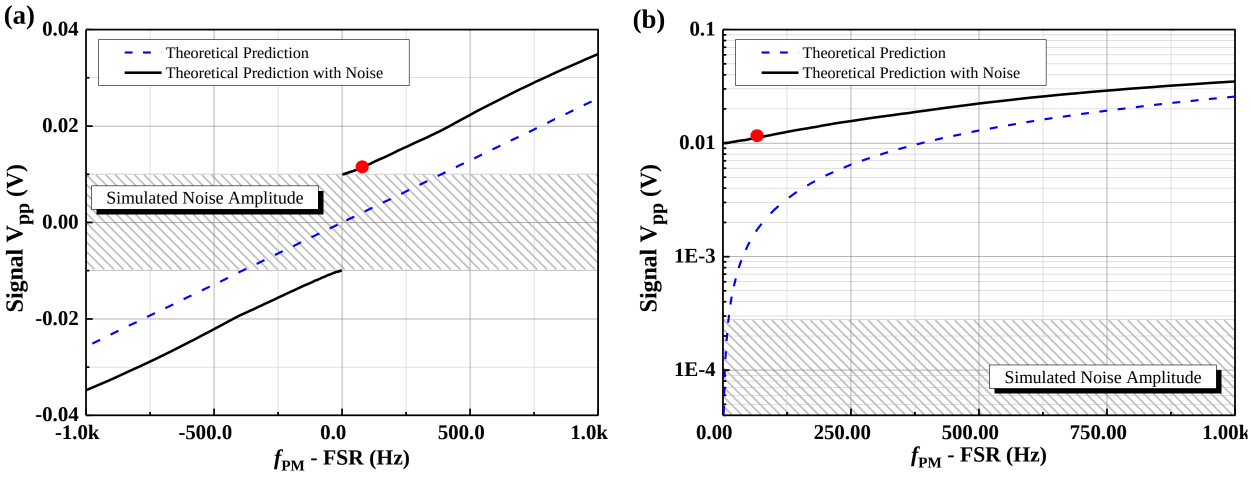

Figure 3.22: Simulation of the peak-to-peak voltage of the error signal as the phase modulation frequency is varied for values close to the etalon FSR, with noise amplitude = 0.01 V. The red dot denotes the resolution limit of the simulation. (a) Linear Scale and (b) Logarithmic scale.

In practice, the peak-to-peak voltage (V_{PP}), is recorded as a function of the modulation frequency (Figure 3.22). The resolution limit of this technique is realized when the signal to noise ratio approaches unity, as indicated by the red dot in Figure 3.22. A significant advantage of the modified PDH technique is that the error signal depends on the phase response of the resonator, which varies linearly near the peak of the resonances in comparison to transmittance measurement techniques that have flat response in the same area of interest. Moreover, it should be noted that the slope of the phase response versus frequency detuning increases linearly with the resonator finesse (for a given FSR) as a result of a reduction in the resonance bandwidth. This effect implies that the relative accuracy of this technique depends on the resonator's finesse. The high accuracy attained by the combination of the modified PDH technique with the frequency swept narrow linewidth laser enables the characterization of Fabry-Perot etalons and resonators with FSRs of up to tens of gigahertz, where phase modulators are available.

3.3.4 Experimental Setup

Although the modified PDH technique has the potential for high accuracy measurements, it can be limited by the linewidth of the laser in use. In the previously published work a (semiconductor) distributed feedback (DFB) laser with MHz linewidth was used to probe etalons having $\mathscr{F}$ = 100, with FSR = 10 GHz, which corresponds to resonances having Δf_{FWHM} = 100 MHz [91]. In that work, the laser was frequency swept via current modulation. However, DFB lasers have inadequate linewidth for etalons having $\Delta f_{\mathrm{FWHM}} < 1$ MHz, thus the FSR measurement of sharp resonances can only be enabled by the use of narrow linewidth lasers. In addition, the required narrow linewidth sources have to be frequency swept with sufficient linearity. In general, narrow laser linewidth is a product of cavity invariance though a frequency sweep implies a modulation of the laser cavity. Thus, for narrow linewidth lasers, the frequency sweep cannot be generated by an intrinsic property of the laser and has to be implemented externally.

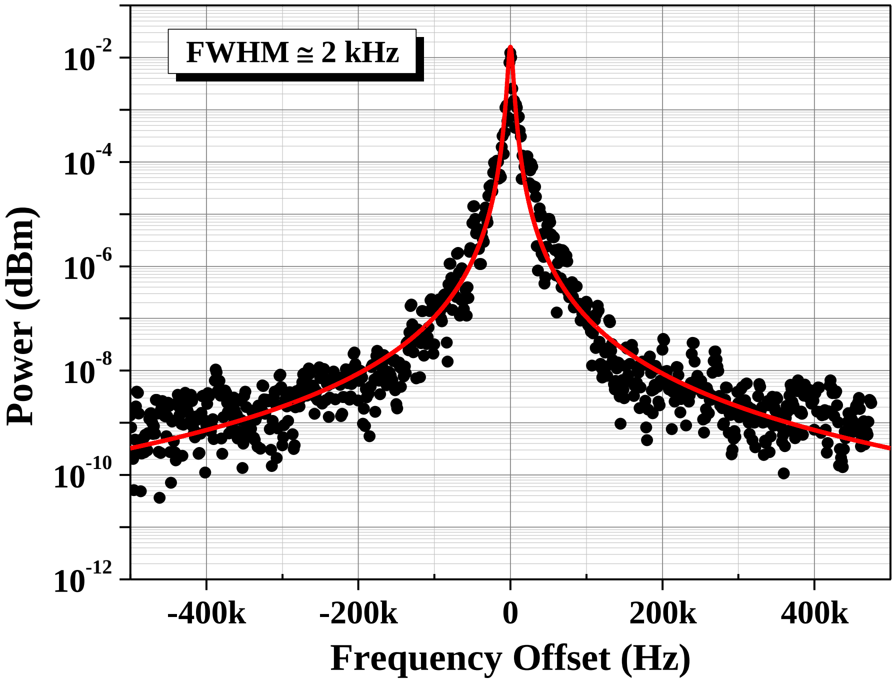

Figure 3.23: Linewidth measurement of the laser source in use. The linewidth of the laser is measured using a heterodyne beat between a pair of similar laser sources to a deconvolved 1 kHz for 1 s.

In this work, a commercially available, narrow linewidth laser source at 1550 nm is used in conjunction with an external frequency sweep implemented using an AOM. The linewidth of the laser is measured via an optical heterodyne beat of two similar lasers and the deconvolved linewidth is measured to be 1 kHz for a measurement of 1 s (Figure 3.23), assuming a Lorentzian distribution.

The AOM used is fiberized and the maximum power in the 1st order deflected beam is obtained by a sinusoidal drive signal at 100 MHz. Scanning of the optical frequency is attained by sweeping the RF frequency driving the AOM. Nevertheless, a change in the driving frequency of the AOM results in a change of the direction of the diffracted 1st order, therefore a deviation from the optimized frequency results in a reduction of the beam power due to reduced fiber coupling. Therefore, a reasonable bandwidth of operation can be defined as the 3 dB, or full width at half maximum (FWHM) bandwidth, usually ~10% of the nominal frequency of the AOM, or 10 MHz for the AOM used.

It should be noted that variations of the optical power input to the resonator do not affect the experiment significantly, since the RF signal generated by the photodetector is directed at the signal port of an electrical mixer. The mixer output is determined by the power at the local oscillator port (under saturation), which for the experiment presented is the phase modulation frequency designed to have sufficient power.

In the experiment conducted, the AOM is driven by an RF signal frequency swept between 95 MHz and 105 MHz, as shown in Figure 3.24. This RF swept signal is generated as the filtered intermodulation product of a mixed local oscillator at 155 MHz with an RF swept source (50 MHz to 60 MHz). This setup resulted in sufficient linearity of the RF frequency sweep, as seen in Figure 3.24, without any spurious tones in the band of interest. The linear RF frequency sweep translates to a linear optical frequency sweep, using the AOM.

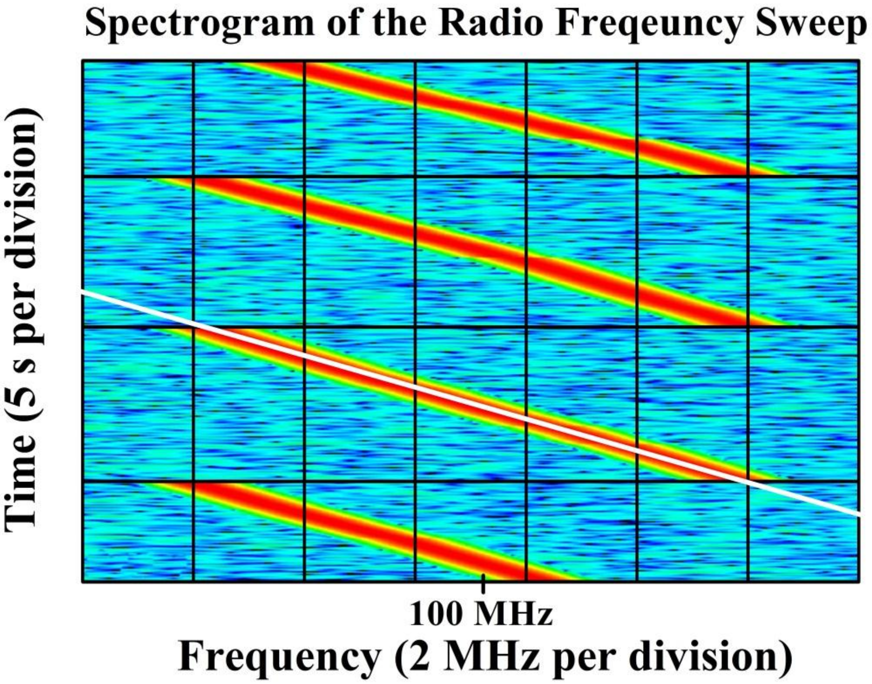

Figure 3.24: Spectrogram of the frequency swept electrical drive of the acousto-optic modulator. Note the sufficient linearity of the driving signal for the generated 10 MHz sweep.

3.3.5 Free Spectral Range Characterization of a Fiberized Etalon

The complete system including the modified PDH setup, depicted in Figure 3.25, is used for the characterization of a commercially available fiberized etalon [24]. The etalon is developed using ~1.02 m of dispersion shifted fiber having zero dispersion wavelength at ~1555 nm. The etalon is specified for FSR = 100 MHz with 1% accuracy and $\mathscr{F} \geq 100$, which corresponds to resonances having $\Delta f_{\mathrm{FWHM}} \leq 1$ MHz. The FSR of this etalon could not be measured using a DFB laser in the same technique, since the resonances are narrower than the linewidth of the DFB laser available.

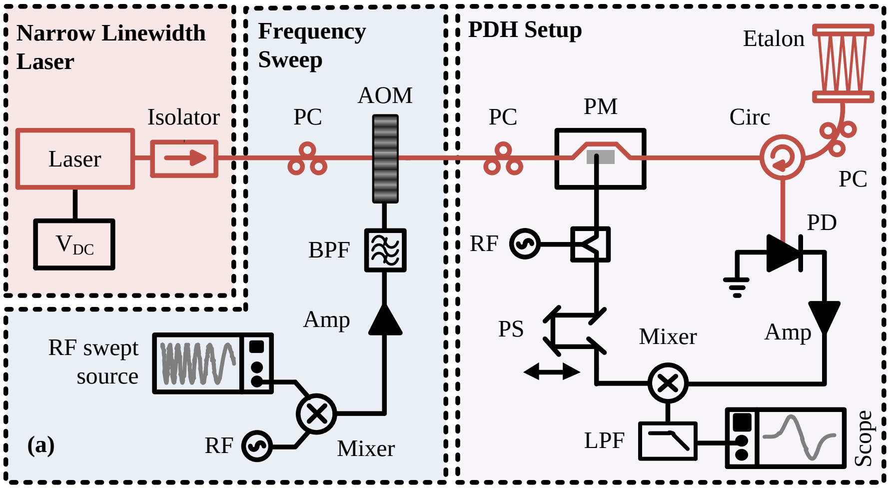

Figure 3.25: Experimental setup schematic. A narrow linewidth laser is frequency swept externally using an acousto-optic modulator driven by the appropriate frequency swept electrical signal. The swept laser source is used in a modified Pound-Drever-Hall setup to measure the free spectral range. VDC, voltage source; PC, polarization controller; AOM, acousto-optic modulator; BPF, band-pass filter; Amp, voltage amplifier; RF, radiofrequency synthesizer; PM, phase modulator; PS, phase shifter; Circ, circulator; PD, photodetector; LPF, low-pass filter.

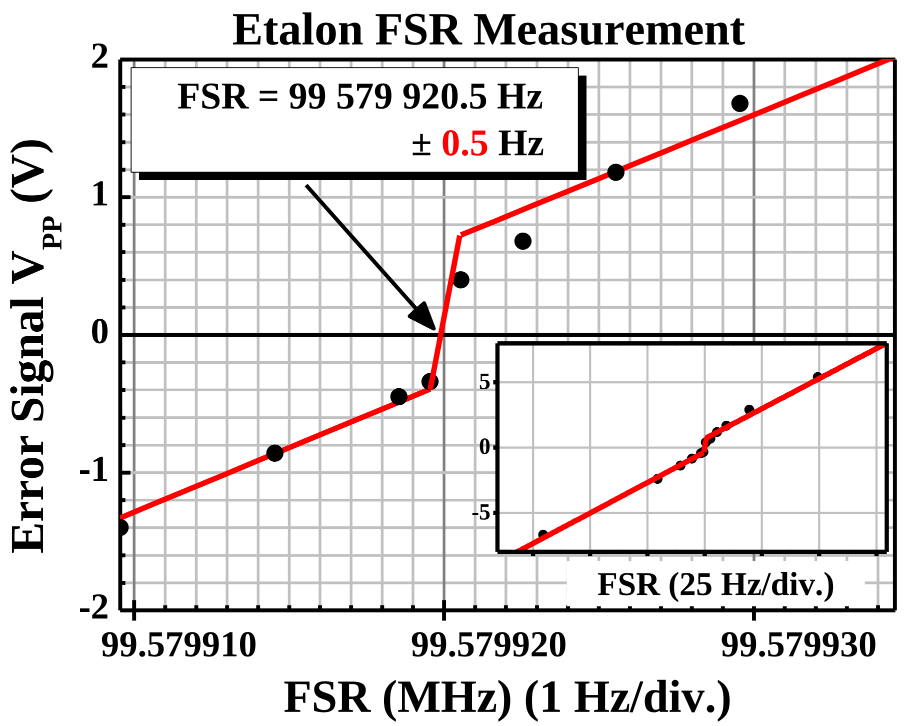

Figure 3.26: Experimental results for the etalon free spectral range measurement. The peak-to-peak voltage of the error signal is recorded as a function of the phase modulation frequency. The FSR for the fiberized etalon is measured with sub-Hz accuracy (10^{-8}).

The FSR of the fiberized etalon is first measured using sidebands that probe the resonance at ± 5 × FSR or ~500 MHz, resulting in an accuracy of better than 1 kHz. Using this result, the etalon is subsequently probed with phase modulation sidebands at ± 100 × FSR to increase the accuracy. The results are presented in Figure 3.26 divided by 100 to enable the calculation of the etalon FSR. As seen in the figure, the change in sign of VPP can be detected for a minimum step of 1 Hz (100 Hz for the raw data). The FSR is experimentally measured to:

$$\mathrm{FSR} = 99\,579\,920.5 \pm 0.5\ \mathrm{Hz}, \tag{3.11}$$

with precision of less than 10^{-8}. This corresponds to an error in the measurement of the length of the meter-long fiber of ~5 nm, or 0.3% of the wavelength of the light used. It should be noted that the accuracy of the technique is extended beyond the limitation imposed by the linewidth of the laser, by using phase modulation sidebands at 100 × FSR.

The increased accuracy attained by the use of the narrow linewidth laser is used to further study the properties of the fiberized etalon. In the above analysis the polarization dependence of the fiberized etalon FSR has been disregarded. Although the etalon is developed using non-polarization maintaining fiber, mechanical stress of the fiber can induce residual birefringence. Thus, the etalon exhibits two different polarization eigenstates which experience two slightly different optical path lengths in the fiberized etalon. This is demonstrated in Figure 3.27 where the high resolution error signal of the two polarization etalon resonances is seen with varying amplitude depending on the laser polarization. For the laser at 1550 nm the two polarization resonances are separated by ~18.8 MHz, or ~19% of the FSR. It should be noted that the two FSRs of the polarization states cannot be measured unless a narrow linewidth laser is used.

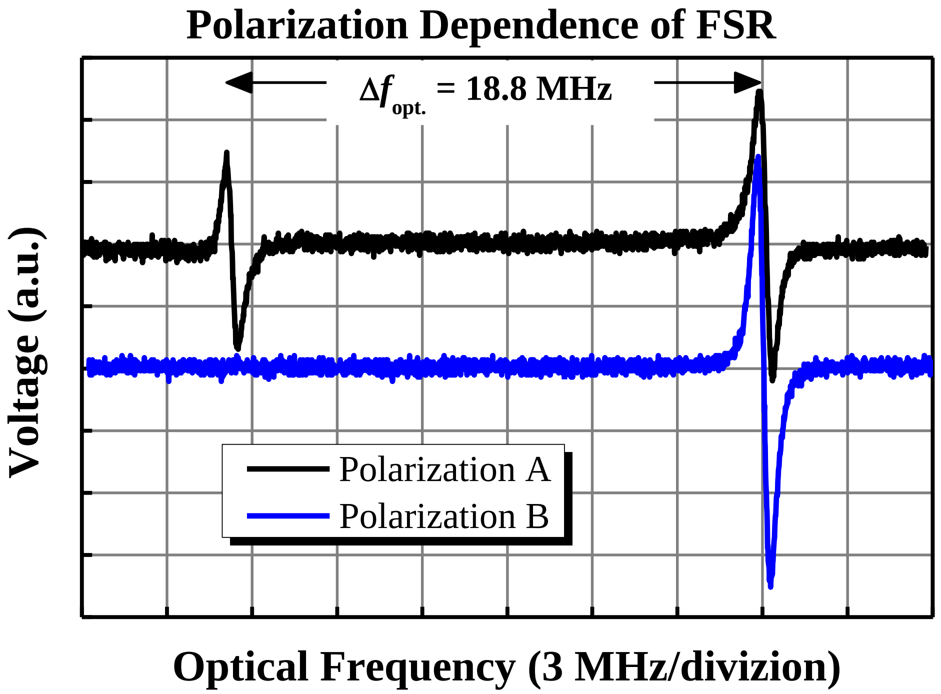

Figure 3.27: Polarization dependence of the free spectral range (FSR) of the etalon. Note that two resonance peaks appear on the black curve when the polarization input to the etalon is not adjusted, while a single peak of higher amplitude remains on the blue curve as the polarization input to the etalon is aligned to one of the polarization eigenstates of the etalon.

The difference between the FSRs of the two polarizations is measured to be: 29 ± 0.5 Hz, or a ~$3 \cdot 10^{-7}$ relative difference. This corresponds to a differential optical path length of ~300 nm, or approximately 1/5 of the wavelength. The specified polarization mode dispersion for the fiber of the etalon is 0.020 ps / $km^{½}$, which corresponds to 190 nm path length difference for the round-trip length of the etalon, or $0.92 \cdot 10^{-7}$. This verifies the validity of the measurement, since the experimentally measured polarization mode dispersion demonstrated as the difference in the

FSRs of the two polarization states is in the same order of magnitude with the fiber used in the etalon.

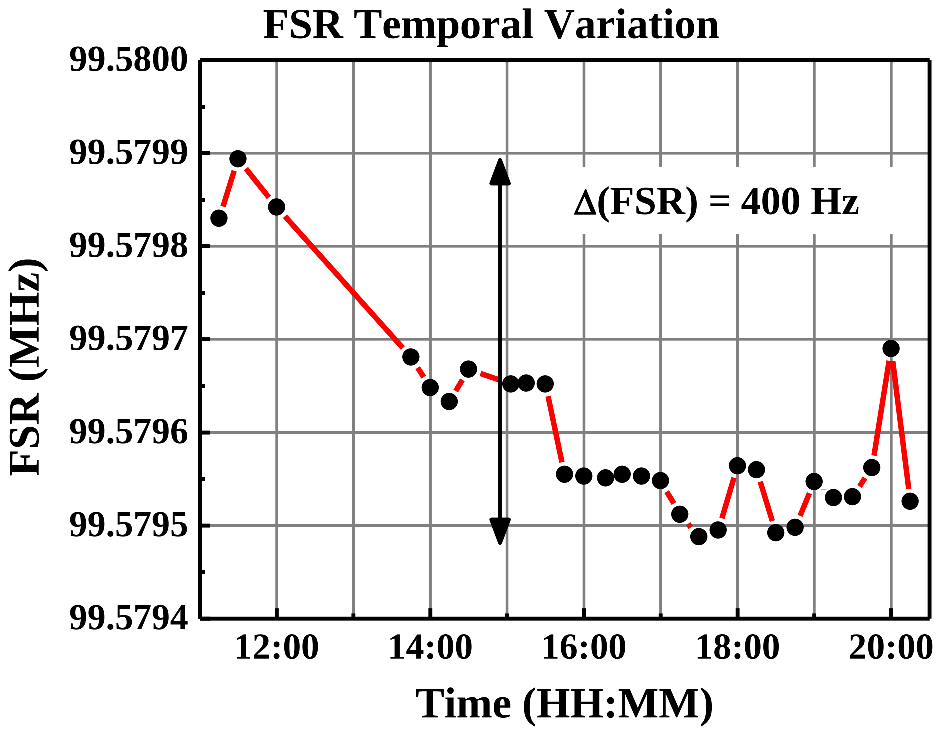

Figure 3.28: Variance of the FSR of the fiberized etalon as a function of time. Note that the FSR varies ~400 Hz in a 9 hour span.

In addition, the high accuracy FSR measurement technique presented enables a study of the variation of the FSR due to the drift of the etalon fiber length. Shown in Figure 3.28 is the FSR of the fiberized etalon as recorded during the working day with sub-Hz accuracy. It can be seen that the FSR of the etalon varies by ~400 Hz, or $4 \cdot 10^{-6}$, in 9 hours.

The thermal expansion coefficient of fused silica, the material used in the fiberized etalon is specified to $\Delta n / n = 6 \cdot 10^{-6}$ ºC^{-1}, which corresponds to: $\Delta(\mathrm{FSR}) = 600$ Hz / ºC for the ~99.58 MHz etalon. Thus, the 400 Hz variation of the etalon FSR corresponds to 0.67 ºC change in the temperature of the etalon during the day, half of which happens during the “cold start” of the system. This temperature variation is reasonable, considering the laboratory conditions, also taking into consideration the power stored in the resonator, which is in the hundreds of mW.

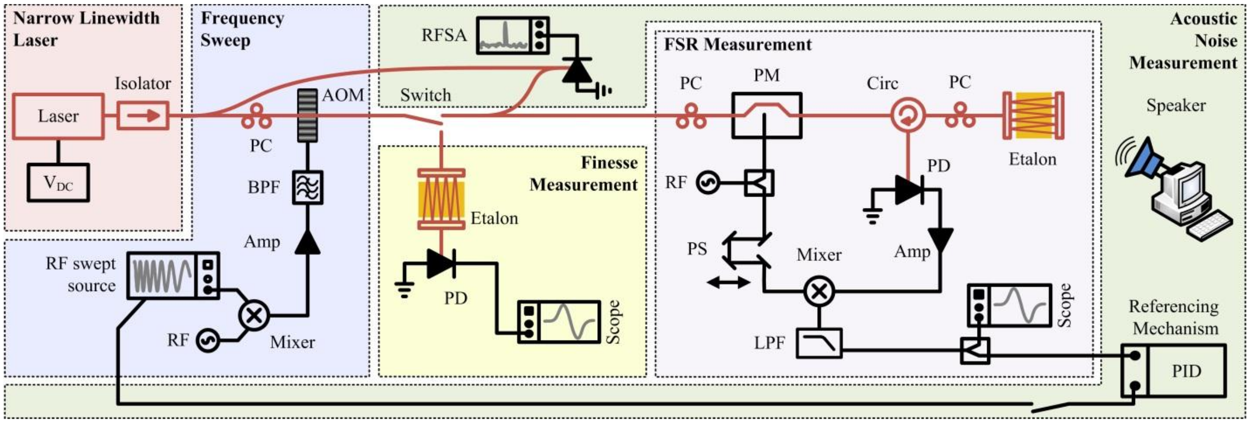

Figure 3.29: Schematic of the experimental setup for all experiments conducted. A narrow linewidth laser is frequency swept using an acousto-optic modulator. A transmission experiment is conducted to measure the finesse of the etalon. The laser is referenced to the fiberized etalon using the PDH scheme enabling the study of the etalon response to acoustic/mechanical noise. VDC, DC Voltage Supply; AOM, Acousto-Optic Modulator; PC, Polarization Controller; PD, Photodetector; LPF, Low-Pass Filter; RF, RF Synthesizer; Amp., Electrical Amplifier; Circ, Circulator; PID, Feedback Servo.

The etalon's transmittance can be used in the experiment depicted in yellow in Figure 3.29 to measure the full-width half maximum of the etalons transmission and subsequently to calculate its finesse. In this scheme the power transmitted through the etalon is measured as the frequency of the laser is linearly swept in time, as in [89]. The time can be converted to optical frequency, due to the linearity of the frequency sweep, as shown in Figure 3.30 (a). The measurement is repeated for various sweep times and frequency spans and the resonance width is calculated as: Δf_{FWHM} = 0.624 MHz ± 0.019 MHz which, given the FSR measured, corresponds to $\mathscr{F}$ = 160 ± 5 (Figure 3.30 (b)). Therefore, the difference in precision between the phase-sensitive modified PDH measurement (10^{-8}) and that of the direct power measurement (5/160 = 3%) is demonstrated.

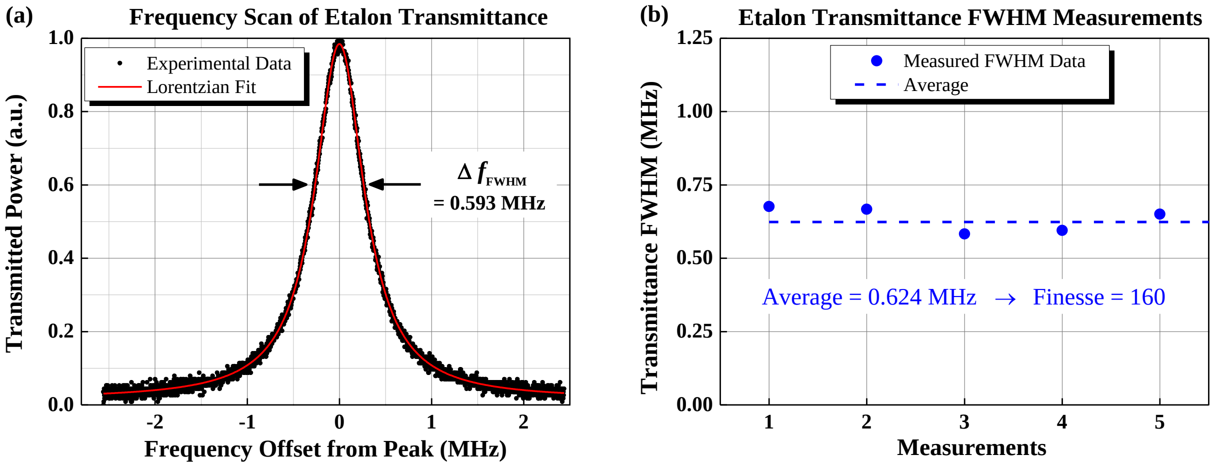

Figure 3.30: (a) Transmission finesse measurement. (b) Finesse measurements as a function of sweep time.

Furthermore, the PDH error signal can be fed to a servo mechanism to reference the laser to the etalon. Specifically, the AOM-shifted frequency of the laser is forced to follow one of the transmission peaks of the etalon. It should be noted that this is not recommended for stabilizing the lasers frequency; on the contrary, since the fiberized etalon is more susceptible to acoustic/mechanical vibrations and background noise the laser's frequency fluctuates with the etalon. Depicted in the green part of Figure 3.29, a self-heterodyne experiment is conducted that down-converts to the microwave regime, the frequency difference between the narrow linewidth laser and its etalon referenced counterpart. Assuming that the laser's short-term frequency stability is superior to the etalon's, which is a good assumption as noted in the experiment, observing the fluctuations of the beat tone one can extract relative measurements for the etalons response to acoustic noise.

Specifically, an acoustic tone of a user-specified frequency is applied in the etalon's surroundings using a speaker system via the use of the following Matlab® code:

```
cf = 80;                        % carrier frequency (Hz)
sf = 22050;                     % sample frequency (Hz)
d = 5.0;                        % duration (s)
n = sf * d;                     % number of samples
s = (1:n) / sf;                 % sound data preparation
s = sin(2 * pi * cf * s);       % sinusoidal modulation
sound(s, sf);                    % sound presentation
pause(d + 0.5);                 % waiting for sound end
```

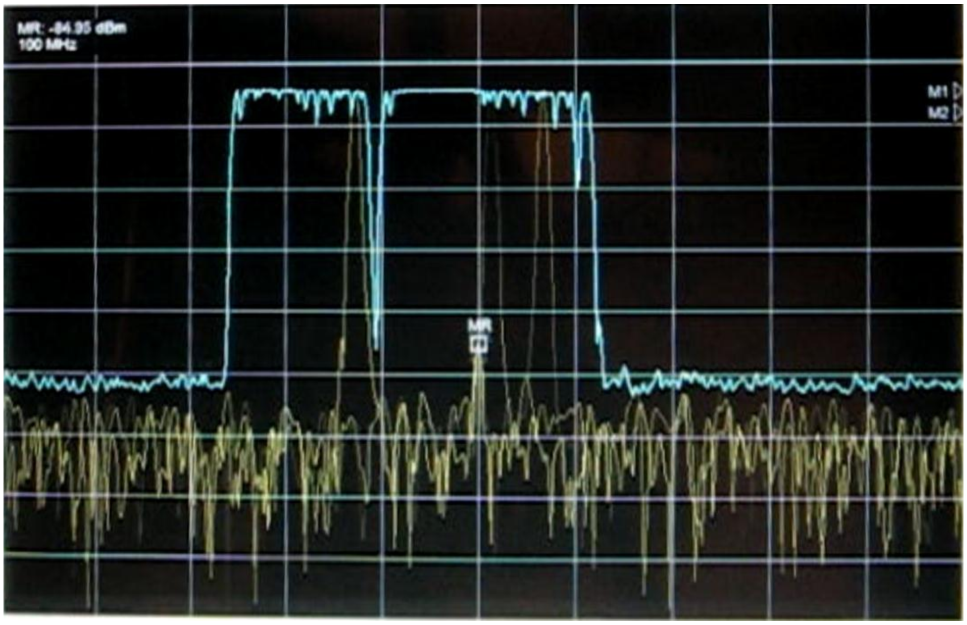

Figure 3.31: Etalon acoustic noise self-heterodyne beat. A real time RF spectrum analyzer is used. Due to the acoustic/mechanical noise, the heterodyne beat frequency fluctuates. The maximum deviation for a specific noise frequency gives a measure of the relative etalon noise susceptibility. x-axis, Frequency; y-axis, power.

During the time that the speakers are operating, the max-hold of the self-heterodyne measurement is recorded, as seen in Figure 3.31. The larger the etalon’s response at an acoustic frequency the larger the deviation of the self-heterodyne beat from its nominal value, the AOM’s operational frequency (100 MHz). The results of the measurements of the etalon’s acoustic response are seen in Figure 3.32, where distinct resonances are observed. The speakers can be used in the ~30 Hz – 20 kHz frequency band. The etalon seems to have resonances up until ~1kHz and after that its response is unresolvable by the measurement system. This information can be used for the design of protection casings for the etalon, to suppress its noise response.

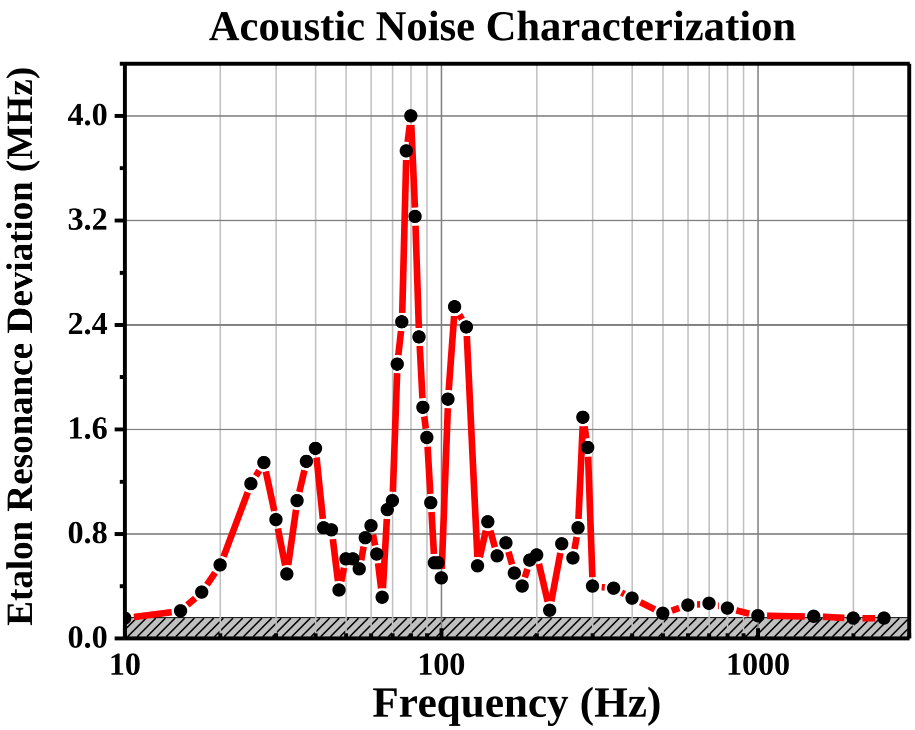

Figure 3.32: Etalon noise response as a function of acoustic/mechanical noise frequency, for constant perturbation power.

3.3.6 Free Spectral Range Measurement of a 10 GHz Etalon

The FSR of a second etalon is measured. The specified FSR for the free-space etalon is 10.24 GHz with 1% precision (100 MHz). The specified finesse for the etalon is 1000, implying Δf_{FWHM} = 10 MHz. For this case the modified PDH technique was used at the laser's neighboring (±1) transmission windows of the etalon. The etalon consists of two mirrors having 50 cm radius of curvature spaced ~3 cm apart. The etalon is sealed and the holder is made of premium grade ultra-low expansion quartz. The experimental results are shown in Figure 3.33, and the calculated FSR is:

$$\mathrm{FSR} = 10.287\,332\,5\ \mathrm{GHz} \pm 2.5\ \mathrm{kHz} \tag{3.12}$$

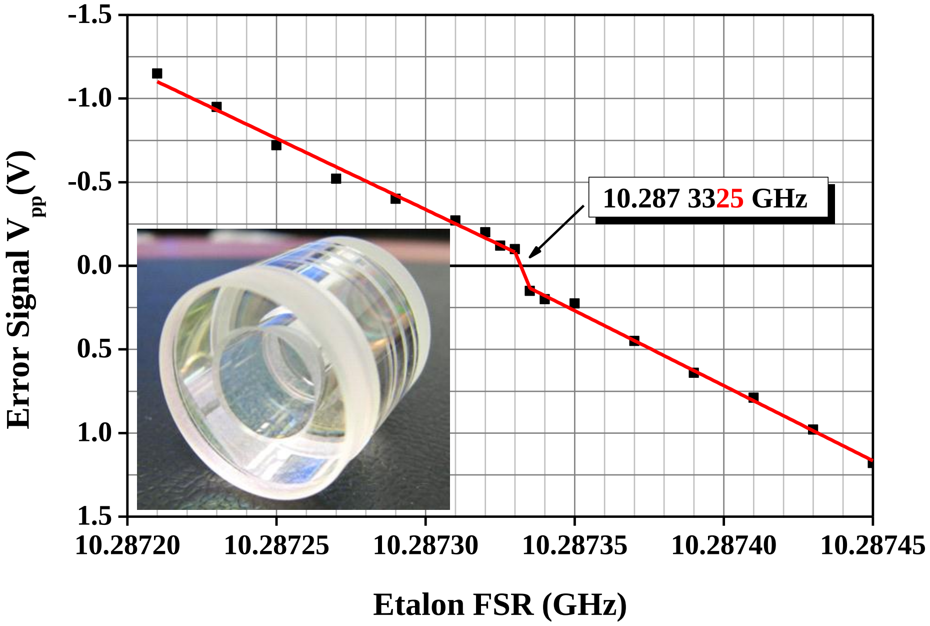

Figure 3.33: 10 GHz etalon FSR measurement. Using the variation of the peak-to-peak voltage of the error signal the FSR of the resonance is calculated to 7 digits of accuracy, for finesse = 10^3. The discontinuity is due to the noise amplitude of the experimental signal (The step at f_m = FSR is the result of the finite width of the measured waveforms due to noise). The etalon is depicted in the inset.

The relative precision attained at the measurement of this etalon is $4 \cdot 10^{-6}$, an improvement of more than 1000 compared to the specified precision. It should be noted that the etalon is found to be within the specified range of 1% of 10.24 GHz.

3.3.7 Discussion

For etalons or resonators with narrow resonances, active locking of the laser to one of the transmission peaks will be beneficial, if not necessary, for both reducing the laser's linewidth and minimizing the relative drift between the laser and the resonator. Moreover, the linear sweep of the laser can be performed using single sideband (SSB) generation, where a specialized phase modulator driven with the appropriate signal is used to shift an optical tone by the RF driving frequency [92]. A sweep in the RF frequency is translated to an optical frequency sweep, as with the AOM technique. In effect, this technique can surpass the frequency sweep limitation of the AOM (at the expense of increased complexity) and was experimentally implemented without any loss of accuracy in the measurements. From the results presented in this work, the SSB generation is used to provide the wide span (30 MHz) results of Figure 3.33, which cannot be attained by the 10 MHz limited sweep of the AOM.

3.3.8 Conclusion on the Etalon Characterization

In this work a 1 kHz linewidth laser source is combined with an AOM (or a SSB generation setup) to induce a linear optical frequency sweep. The linearly swept narrow linewidth laser is used in a (previously demonstrated) modified PDH scheme to measure the free spectral range of a fiberized etalon with sub-Hz accuracy. The free spectral range of the etalon used is measured to be: 99 579 920.5 ± 0.5 Hz, or a relative error of less 10^{-8}. The PMD of the fiber results in an experimentally measured 29 Hz difference between the free spectral ranges of the two polarization states. The thermal drift of the fiber is measured to be 400 Hz in a 9 hour interval, which corresponds to 7.3 ºC change in the temperature of the etalon. The modified PDH technique offers increased accuracy due to the linear phase response of etalons around their resonances, while the use of a narrow-linewidth laser combined with an AOM-induced sweep improves upon the accuracy of the technique by a factor of 10^4. A free space etalon's FSR is also measured with $4 \cdot 10^{-6}$ precision (10.287 332 5 GHz ± 2.5 kHz). The high precision results obtained by this technique can be used by etalon manufacturers to improve on their manufacturing processes. In conclusion, this technique is expected to result in higher accuracy for resonators having higher finesse.

3.4 Time Demultiplexing of Ultra-Low Noise High Repetition Rate Lasers

3.4.1 Introduction

In the last few decades, communication links have evolved from analog to digital schemes, allowing for essentially lossless transfer of information. This is because degradation of signals induced by amplification, processing, or transmission can be overcome by using the digital format at the expense of system complexity. The information has to be converted from the analog to the digital format and vice versa, if needed. For commercial applications, the current analog-to-digital conversion (ADC) technology is based on electronic circuits.

This work is focused on providing a pulsed laser source suitable for high bandwidth photonic ADC, a technology aimed at surpassing the speed and accuracy limitations of state of the art electronics [93]. The approach presented in this work uses a harmonically mode-locked semiconductor-based ring cavity laser having a repetition rate in the GHz regime that is time demultiplexed to provide a low repetition rate and ultra-low noise pulse train, as required by high bandwidth ADC. A significant advantage of time demultiplexing is that high wall-plug efficiency (WPE) for the system can be attained if multiple demultiplexed pulse trains are used in parallel system architecture. Although both high repetition semiconductor lasers [94] and time demultiplexing of optical pulses [95] have been demonstrated, this work harvests the advantages the combination of a semiconductor-based high repetition rate mode-locked laser (MLL) with the time demultiplexing technique and focuses on the analysis of the phase noise of the time demultiplexed pulse train.

Semiconductor gain media have short carrier lifetimes favoring repetition rates in the multi-gigahertz range [96], thus external cavities are used in conjunction with active mode-locking to attain low noise operation. The use of actively mode-locked lasers operated at high repetition rates enables shorter pulse durations, since the pulse duration is inversely proportional to the square root of the modulation frequency [97] and MLLs with pulse duration in the order of picoseconds have been developed [94]. A significant advantage of semiconductor-based lasers is their potential for ultra-low amplitude noise performance [94]. In comparison, the amplitude noise performance of fiber lasers with MHz repetition rates is degraded by the long lifetime of Erbium which results in relaxation oscillations [98].

Moreover, semiconductor-based lasers can achieve high WPE and are robust, compact and inexpensive when mass produced, which makes them preferable for commercial applications. Although time demultiplexing of optical pulses is conceptually straightforward, the performance characteristics of the output optical pulses can be irreversibly degraded in the different stages of a pulse demultiplexing system. In this work, the extinction ratio of the pulses (crosstalk) is addressed by using a low noise pattern generator (PG).

Furthermore, as the in-depth analysis of the phase noise of the pulse train presented in this work shows, timing jitter in the femtosecond regime is difficult to achieve using low frequency pulse trains due to the relative nature of timing jitter, as will be discussed. On the other hand, high repetition rate semiconductor-based MLLs have been developed having attosecond noise [99]. As a result, time demultiplexing a high frequency semiconductor-based MLL is appealing for acquiring ultra-low noise pulse trains at MHz rates.

3.4.2 Phase Noise of Time Demultiplexed Pulse Trains

The phase noise of the MHz repetition rate pulse train is one of the most critical parameters of this work and justifies the selection of both semiconductor as the gain medium of the laser and time demultiplexing as the technique for acquiring MHz pulse trains, as discussed in the introduction. Thus, a description of the behavior of the phase noise performance of ultra-low noise pulse trains during time demultiplexing is presented before the results this work.

The properties of a harmonically MLL as it undergoes time demultiplexing to the cavity fundamental frequency (CFF or ν_0) are first presented. A schematic representation of the typical properties of a harmonically MLL is shown in Figure 3.34 (a) [97]. In harmonically MLLs more than one pulse exists within the laser cavity and the repetition rate of the laser is an integer harmonic of the CFF. The time intensity profile of a harmonically MLL consists of N interleaved pulse sets each having frequency equal to the CFF, where N is an integer. In the optical frequency domain, the pulse sets generate overlapping frequency combs with tones separated by the CFF. Phase correlation among the overlapping frequency combs can give rise to a single optical axial mode group with tone separation equal to the MLL's repetition rate ($N \times \nu_0$), while the other axial mode groups are suppressed [94]. The photodetected laser output of a harmonically MLL has tones at harmonics of the repetition rate of the laser and N-1 interleaved supermode noise spurs (SNS) due to the beating between the optical axial modes.

Subsequently, the SNS also appear in the amplitude and phase noise spectra and contribute to the integrated amplitude and timing jitter of the laser [71]. Time demultiplexing a harmonically MLL to a frequency equal to the CFF induces significant changes in the properties of the pulse train. The frequency of the time demultiplexed pulse train becomes equal to the CFF, while the optical spectrum of the pulse train changes and a single comb with spacing equal to the CFF remains. Moreover, the photodetected RF spectrum of the pulse train will have tones of equal power at every multiple of the CFF, in the case of perfect demodulation of the optical pulses.

The integrated timing jitter in a specific band (σ_j) is calculated using (3.13) given the single sideband power spectral density of the laser's phase noise ($\mathcal{L}(f)$) [100].

$$\sigma_j = \frac{1}{2 \cdot \pi \cdot f_{rep}} \cdot \sqrt{2 \int_{1/t_m}^{f_{Stop}} \mathcal{L}(f) \cdot df} \tag{3.13}$$

The start frequency corresponds to the inverse of the measurement time (t_m). Setting $f_{Stop} = f_{MLL} / 2$, the Nyquist frequency of the pulse train [101], results in the total timing jitter of the pulse train. Whereas, for $f_{Stop} = \nu_0 / 2$ the integration gives the timing jitter for each of the individual pulse sets of the harmonically MLL with repetition rates equal to the CFF. The relative nature of timing jitter should be noted, since the square root term gives the jitter as a percentage of the laser period. This implies that short period, or high repetition rate, lasers can more easily achieve ultra-low integrated timing jitter.

The phase noise of the time demultiplexed pulse train shows significant differences compared to the phase noise of the harmonically MLL, as depicted in Figure 3.34 (b). First, the Nyquist frequency of the demultiplexed pulses is reduced by a factor of N compared to that of the MLL because time demultiplexing reduces the repetition rate of the pulses by the same factor. That alone reduces the timing jitter integrated to the corresponding Nyquist frequency of each pulse train, since this excludes the contribution to the timing jitter of the multiple pulse sets of the harmonically MLL.

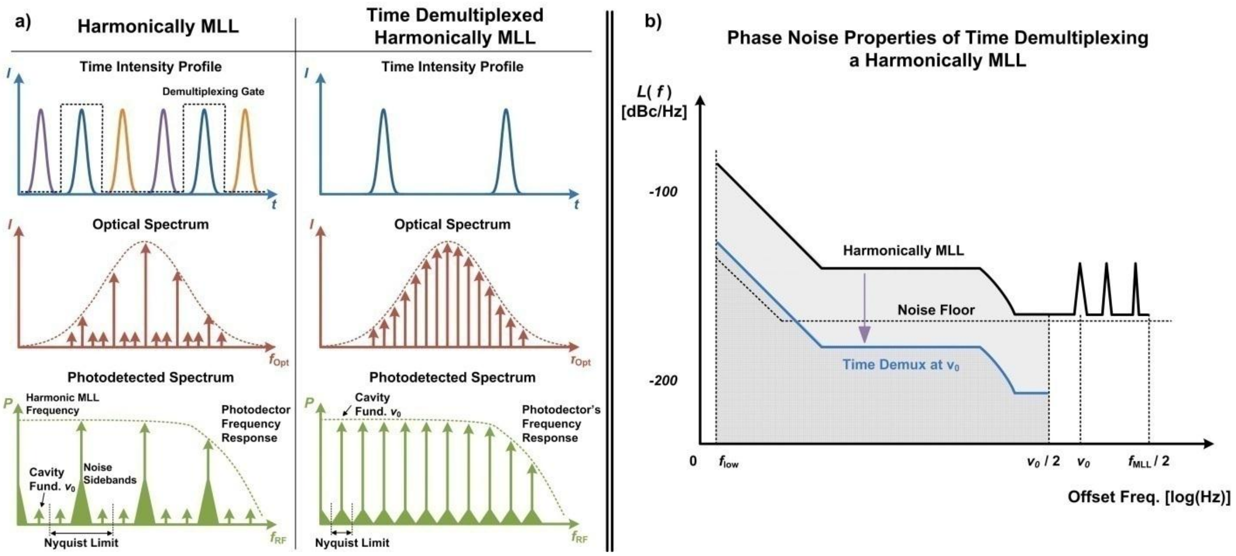

Figure 3.34: a) Schematic depiction of the properties of a harmonically mode-locked laser and the pulse train demultiplexed at the cavity fundamental frequency for $f_{MLL} = 3 \times \nu_0$, b) Effect on the phase noise of time demultiplexing a harmonically mode-locked laser to the fundamental frequency of the laser cavity for $f_{MLL} = 7 \times \nu_0$.

The second and most critical difference in the phase noise of a harmonically MLL and that of a time demultiplexed pulse train is the drastic reduction in the magnitude of $\mathcal{L}(\mathrm{f})$. This can be seen by noting that time demultiplexing the pulses emitted by the MLL does not affect their integrated timing jitter (σ_j), when the pulses have a shorter duration compared to the demultiplexing signal. Thus, the timing jitter of a pulse set of the harmonically MLL is preserved under time demultiplexing, or:

$$\sigma_{j,\ \mathit{Pulse\ set\ of\ MLL}} = \sigma_{\mathit{Demultiplexed\ pulse\ set\ of\ MLL}} \tag{3.14}$$

This implies:

$$\frac{1}{2\cdot\pi\cdot f_{MLL}}\cdot\sqrt{2\int_{1/t_m}^{\nu_0}\mathcal{L}(\mathrm{f})\cdot df} = \frac{1}{2\cdot\pi\cdot\nu_0}\cdot\sqrt{2\int_{1/t_m}^{\nu_0}\mathcal{L}'(\mathrm{f})\cdot df} \tag{3.15}$$

However, since $f_{MLL} = N \times \nu_0$ and the functional form of the phase noise power spectral density should be unaltered:

$$\mathcal{L}'(\mathrm{f}) = \frac{\mathcal{L}(\mathrm{f})}{\mathrm{N}^2} \quad \text{or} \quad \mathcal{L}'(\mathrm{f})_{dB} = \mathcal{L}(\mathrm{f})_{dB} - 10\cdot log(\mathrm{N}^2) \tag{3.16}$$

This implies that the phase noise power spectral density $\mathcal{L}(\mathrm{f})$ reduces with the square of the demultiplexing factor (N^2). This leads to a dramatic decrease of the relative timing jitter of the pulse train, since the absolute jitter is preserved, when the period of the pulse train is increased. $\mathcal{L}(\mathrm{f})$ for a time demultiplexed laser having timing jitter in the femtosecond regime cannot be measured because a significant part of $\mathcal{L}(\mathrm{f})$ is beneath the noise floor of typical measurement setups. Thus, an alternative way of measuring the timing jitter of the demultiplexed pulse train has to be applied. This is addressed in Section 3.4.4.

3.4.3 High Repetition Rate Oscillator

The performance needed for high bandwidth ADC can be attained using actively MLLs with GHz repetition rates. It should be stressed that obtaining ultra-low noise clocks at low repetition rates is difficult owing to the properties of phase noise, as described above. Hence the way to achieve low repetition rate pulse trains is by dividing the repetition rate of a low noise source operating at a higher rate. The high quality noise performance of the high repetition laser is preserved at the reduced rate. This section describes the developed laser oscillator operating at 2.56 GHz that serves as the pulse source that will be subsequently time demultiplexed.

The laser is harmonically mode-locked at 2.56 GHz through loss modulation using an intensity modulator driven by a low noise oscillator (LNO). The length of the ring cavity (~2.5

m) is adjusted using a variable optical delay in order for the fixed frequency of the LNO to match an integer multiple of the CFF (= 80 MHz). A 20 % directional coupler is used for extracting the pulses from the laser cavity, while an isolator guarantees unidirectional operation. The components used in the laser cavity are commercially available except for the semiconductor amplifier. A schematic representation of the ring laser developed is shown in Figure 3.35.

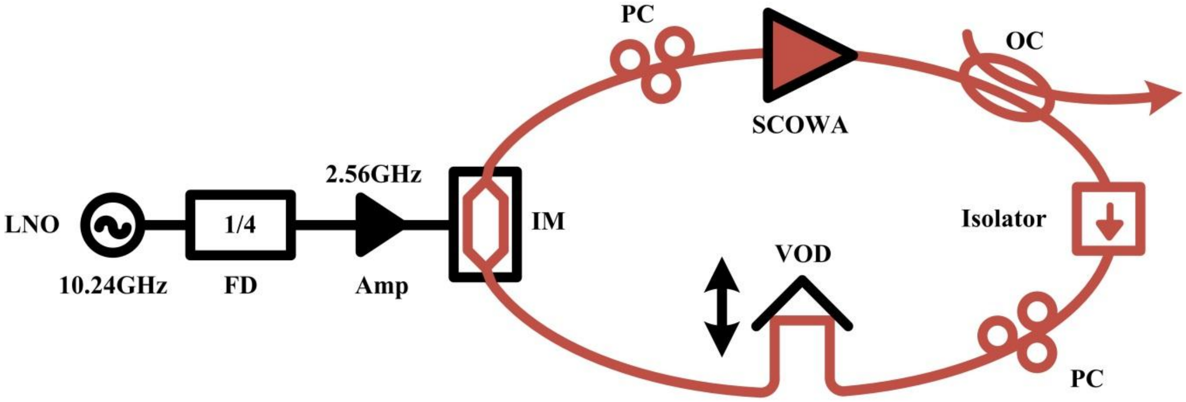

Figure 3.35: Schematic of the harmonically mode-locked ring laser operating at a fixed repetition rate of 2.56 GHz. LNO, low noise oscillator; VOD, variable optical delay; FD, frequency divider; Amp, electrical amplifier; IM, intensity modulator; PC, polarization controller; SCOWA, slab-coupled optical waveguide amplifier; OC, output coupler.

Gain in the laser cavity is provided by the use of a semiconductor optical amplifier (SOA) in order for the laser to have both increased wall-plug efficiency and low noise characteristics. Specifically, a slab-coupled optical waveguide amplifier (SCOWA) is used having saturation power in excess of 300 mW while providing a small signal gain of ~25 dB for

4 A of injection current [102]],[70]. The high saturation power and the reduced mode overlap of the SCOWA compared to commercially available SOAs contributes to the low noise performance of the laser. The spectral peak of the gain of the SCOWA is centered at ~1510 nm. The average output power of the laser oscillator is ~25 mW.

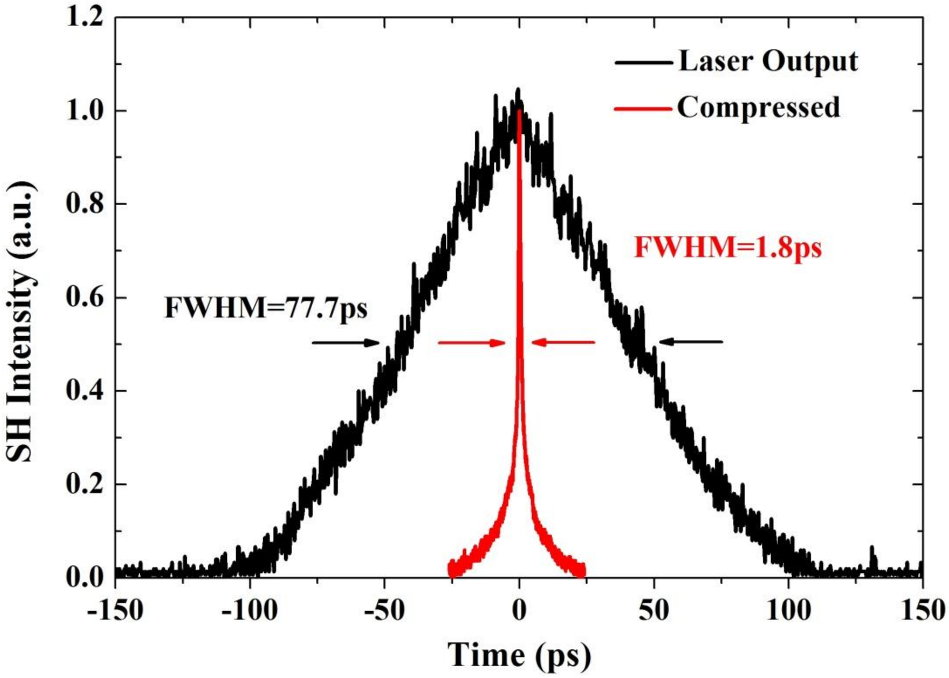

Figure 3.36: a) Second Harmonic (SH) autocorrelation trace of the ring laser output (black curve) and of the compressed pulse train (red curve). Note the triangular shape of the autocorrelation trace of the laser output implying linear chirp. The compression ratio achieved is ~43. b) Optical Spectrum of the ring laser operated at 2.56 GHz. The spectral bandwidth at 20 dB is ~25 nm.

The time duration of the second harmonic autocorrelation trace of the pulse train is $\Delta\tau_{FWHM}$ = 78 ps and exhibits a triangular shape, which is an indication of linearly chirped pulses.

The chirp of the laser pulses is compensated using a dual grating compressor having linear dispersion of -3 ps/nm which results in $\Delta\tau_{FWHM}$ = 1.8 ps for the time duration of the autocorrelation trace [103]. The compression ratio of the pulses is ~43. The second harmonic autocorrelation trace of the laser pulses directly at the cavity output and after compression is shown in Figure 3.36.

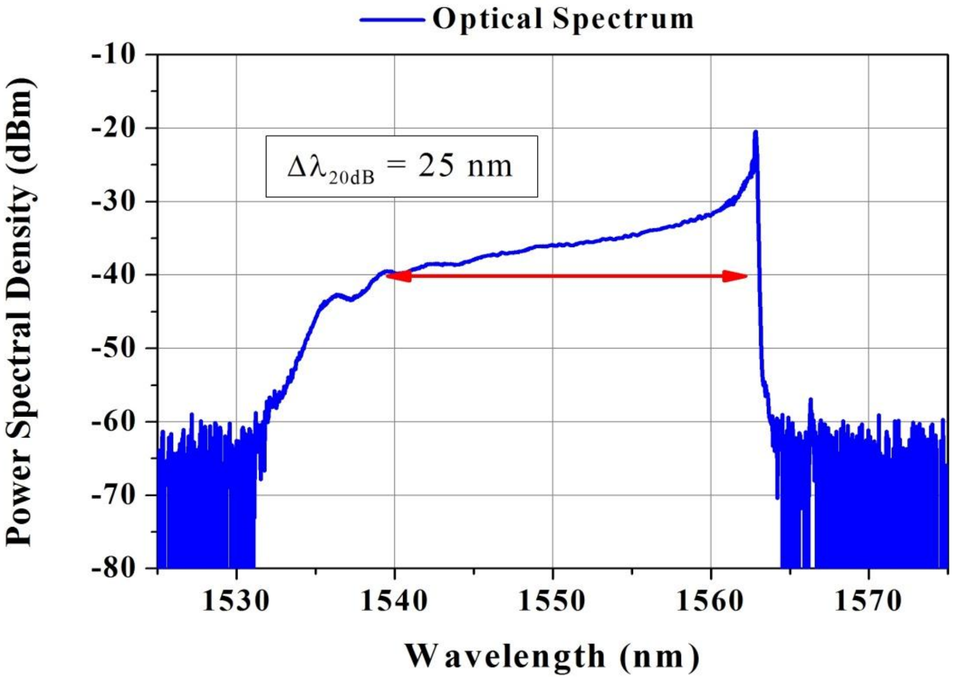

Figure 3.37: Optical Spectrum of the ring laser operated at 2.56 GHz. The spectral bandwidth at 20 dB is ~25 nm.

The optical spectrum of the ring laser oscillator is asymmetric, having a peak on the long wavelength side, as shown in Figure 3.37. It should be noted that although the FWHM optical bandwidth is less than 1 nm, a significant amount of power is carried in the short wavelength part of the spectrum. Accordingly, it is appropriate to define the spectral bandwidth of interest as the 20 dB bandwidth relative to the peak of the optical spectrum. The 20 dB bandwidth is measured to $\Delta\lambda_{20\ \mathrm{dB}}$ = 25 nm. If a stretched pulse source is needed, the uniformity of the time intensity profile of the pulses can be improved by using a feedforward scheme, as described in [104].

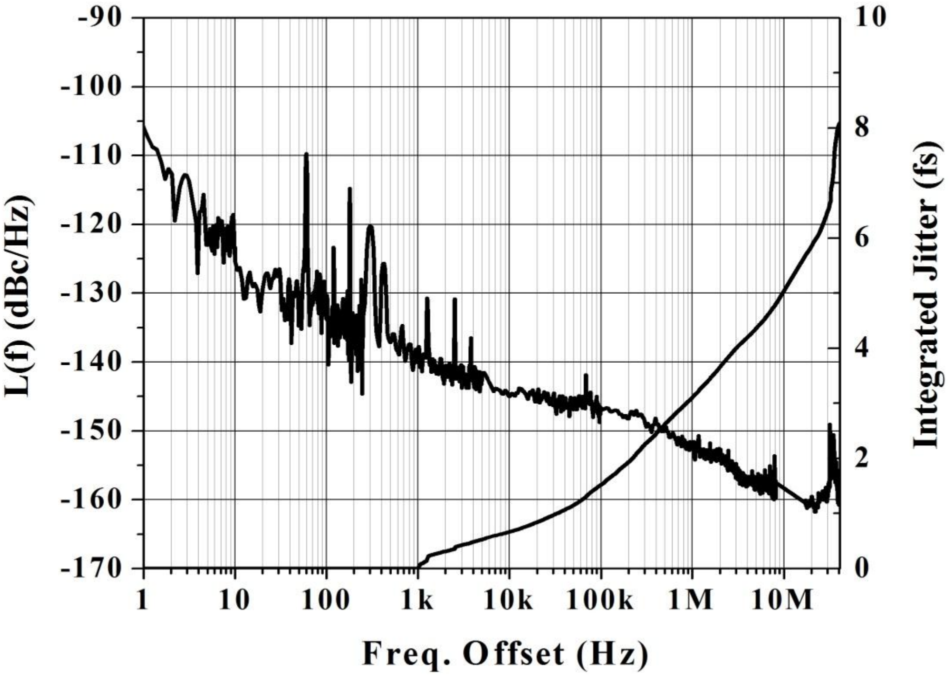

Figure 3.38: Single sideband residual phase noise power spectral density integrated to the carrier power and integrated timing jitter of the ring laser at 2.56 GHz. The timing jitter is found to be 8 fs integrated from 1 kHz to 40 MHz.

The AM and PM noise power spectral densities presented in this work are acquired using the photodetected RF spectra of the pulse trains [100]. A photodetector with sufficient bandwidth and power handling is used in conjunction with a commercially available noise measurement system to achieve high dynamic range. The laser system developed in this work is designed for use in an ADC system based on a mono-static architecture where the echo of an RF signal is compared to the signal transmitted. Thus, assuming that the RF signal is phase-locked with the mode-locking LNO, the noise added by the laser compared to the LNO is sufficient for characterizing the timing jitter of the pulses. Accordingly, the phase noise presented in this work is always measured against the LNO resulting in what is defined as *residual* phase noise spectra and integrated timing jitter values.

The residual phase noise of the ring laser is shown in Figure 3.38. The timing jitter, which is calculated by integrating the phase noise [100], is ~8 fs, integrated from 1 kHz to 40 MHz. The start point for the integration band is chosen as 1 kHz because the system is designed to operate with signals having a return time delay no longer than 1 ms, while the end of the band is ν_0 / 2 = 40 MHz, the Nyquist limit of the time demultiplexed pulse train. Terminating the integration band at ν_0 / 2 implies that the laser noise performance is determined by the noise of one of the pulse sets of the harmonically MLL. Therefore the noise added by the interplay between pulse sets is completely filtered. This is the case of interest since a single pulse set is time demultiplexed in Section 3.4.4.

Figure 3.39 shows the single sideband Amplitude Modulation (AM) noise power spectral density relative to the carrier power and the integrated AM noise of the ring laser. The integrated amplitude noise from 1 kHz to 40 MHz is ~0.0125 %. Note that the AM noise of the input to the demultiplexer is unaffected by either the optical amplification or the pulse compression, as seen by the red curve of Figure 3.39.

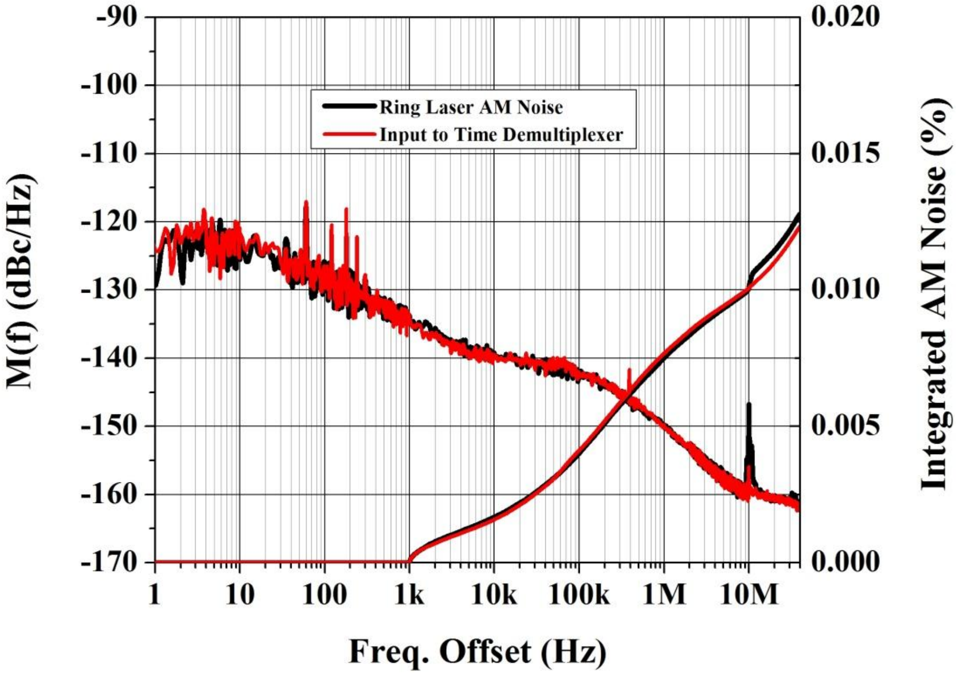

Figure 3.39: Single sideband amplitude modulation (AM) noise power spectral density normalized to the carrier power and integrated AM noise of the ring laser operating at 2.56 GHz directly at the output of the laser (black curve) and after being compressed by a dual grating pair compressor and amplified using an Erbium-Doped Fiber Amplifier (red curve). Note that there is no degradation of AM noise of the signal. The 10 MHz spike is due to environmental noise.

3.4.4 Cavity Fundamental Frequency Demultiplexing

This section describes the generation of a low repetition rate pulse train having low amplitude and phase noise, high WPE and short pulse duration via time demultiplexing the high repetition rate, semiconductor-based MLL described in section 3.4.3. The experimental setup used is depicted in Figure 3.40.

The LNO operates at 2.56 GHz generating a low amplitude and phase noise signal used for both mode-locking and for triggering an electrical PG. The pulses generated by the low noise MLL described in Section 3.4.3 are compressed using a dual grating compressor and amplified before directed to the input of the time demultiplexer. Compressing the pulses is advantageous for the system design, since the time duration of the pulses (~1.8 ps FWHM) is much shorter than the duration of the electrical demultiplexing gate (~391 ps), eliminating edge effects that potentially may affect the noise properties of the pulses.

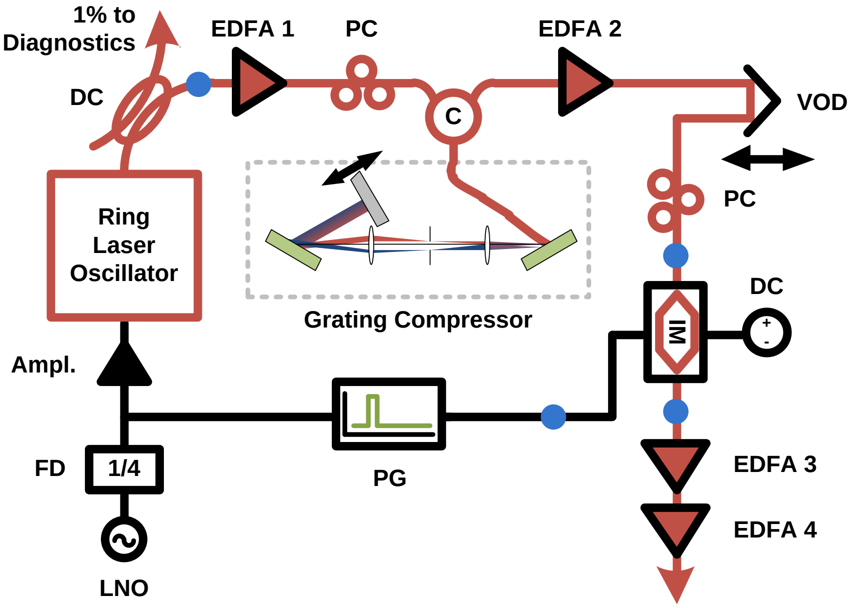

Figure 3.40: System schematic for time demultiplexing the 2.56 GHz pulse train emitted from the ring laser to its cavity fundamental frequency (80 MHz). The pulses are compressed in a dual grating pair compressor, amplified using an Erbium-doped fiber amplifier (EDFA) and selected using an Intensity Modulator (IM) driven by a Pattern Generator (PG). The blue dots correspond to points of the system where the performance of the system is evaluated. LNO, low noise oscillator; FD, frequency divider; Ampl., electrical amplifier; DC, directional coupler; PC, polarization controller; C, circulator; VOD, variable optical delay; DC, DC voltage supply.

Time demultiplexing the MLL to 80 MHz, corresponding to $N = 32$ times, would demand at least five 1-by-2 interferometric switches [95], increasing the complexity of the experimental setup. Instead, a proof-of-concept experiment is conducted, where a single intensity modulator driven by the appropriate electrical signal attenuates the unwanted pulses as opposed to directing them to different channels. Both time demultiplexing and attenuating the pulses affect in a similar way the performance characteristics of the pulse train. The system developed gives access to a single pulse train at the CFF, while a system using the full tree of (31) switches would provide multiple (N = 32) pulse trains. The availability of multiple ultra-low noise pulse trains can be advantageous for systems based on parallel architectures. Moreover, the WPE of the system would be improved in a parallel system architecture.

The electrical pattern generator used is synchronized with the common 2.56 GHz signal and has the ability to create return-to-zero square pulse patterns with minimal bit time duration equal to integer multiples of ~391 ps, which is the period of the 2.56 GHz signal. An electrical signal consisting of one 2 V bin followed by thirty one 0 V bins is programmed and drives an intensity modulator which, when biased appropriately, attenuates the optical pulses arriving when the pattern generator signal is 0 V, while allowing the pulses to transmit otherwise.

The AM noise of the demultiplexed pulse train is a combination of the AM noise of the 2.56 GHz pulse train and the noise of the demultiplexing electrical gate. Since the two noise sources are uncorrelated, their combined effect is the sum of the individual components. The single sideband AM noise power spectral density for the input and output pulse trains as well as for the electrical demultiplexing gate are shown in Figure 3.41 (a). The integrated AM noise of the 80 MHz pulse train from 1 kHz to 40 MHz, the Nyquist frequency of the pulse train, is ~0.017 %. The degradation of the AM noise of the pulse train is minimal, due to the ultra-low noise of the electrical gate.

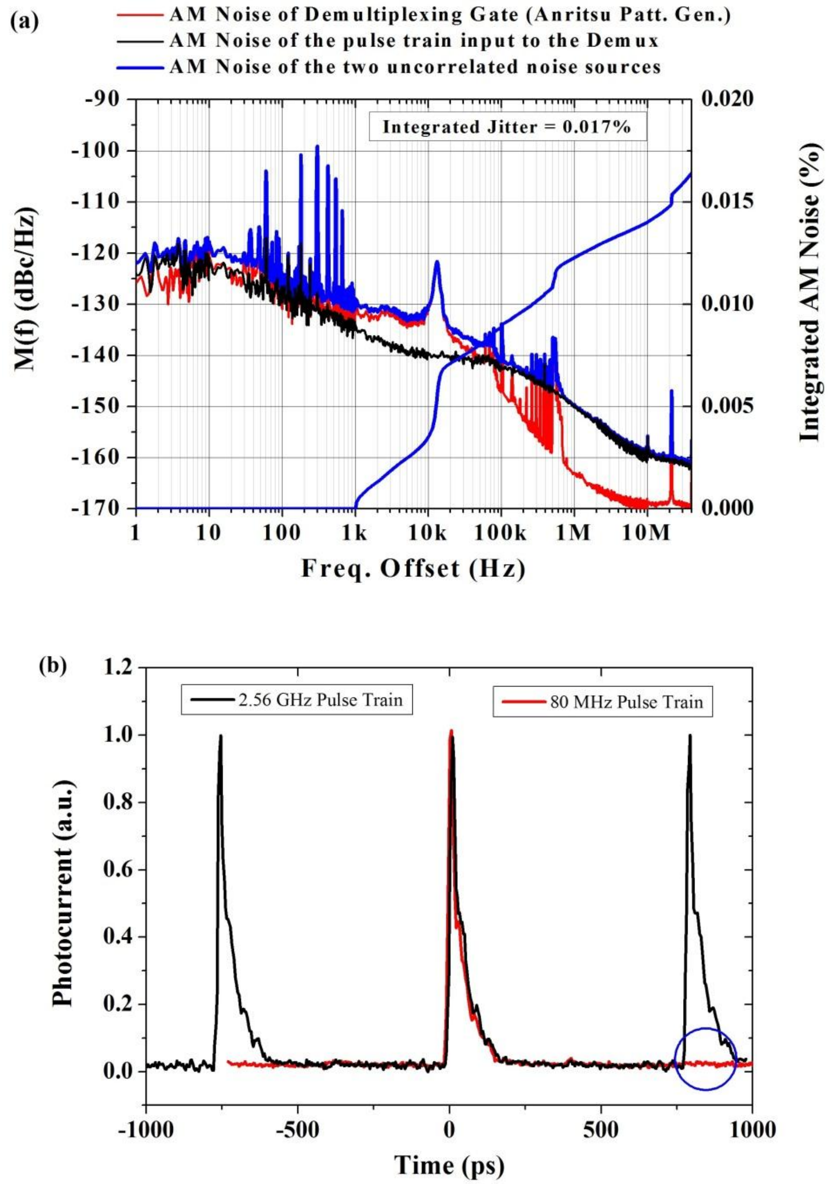

Figure 3.41: a) AM noise of the 80 MHz pulse train integrated to the Nyquist limit. The two uncorrelated noise sources of the 2.56 GHz pulse train and the electrical gate are summed giving the expected noise of pulse train at the cavity fundamental frequency. b) Time intensity profile of the photodetected pulses of the laser oscillator (black line) and the time demultiplexed pulse train (red line). The sampling oscilloscope uses an optical module having 30 GHz of bandwidth.

The time intensity profile of the photodetected pulses emitted by both the 2.56 GHz ring laser and the time demultiplexed system at 80 MHz are shown in Figure 3.41 (b). Note the ample extinction achieved by the combined use of a PG and an intensity modulator.

In addition, a high power pulse train having sufficient WPE is desired. This is attained by using a power efficient SCOWA as the gain medium for the ring laser and EDFAs for amplifying the ultrashort pulses. The pulse train is carefully amplified at the system and to achieve high WPE, making use of the high WPE and saturation power of EDFAs. Specifically, the 80 MHz pulse train is amplified twice using EDFAs to achieve 500 mW of average power with a total system WPE of 4 %, considering power consumed by solely the opto-electrical components. Keeping all the time demultiplexed pulse trains would yield a system with multiple parallel ultra-low noise pulse trains while improving the WPE of the total system.

As discussed in section 3.4.2, measuring the residual phase noise of the 80 MHz pulse train is challenging. Time demultiplexing a 2.56 GHz pulse train to 80 MHz implies that $N = 32$, while $N^2 = 1024 \approx 30$ dB. This reduction of $\mathcal{L}(f)$ implies that most of it lies beneath the noise floor of the measurement system, as described using Figure 3.34 (b). Moreover, residual phase noise measurement is not possible for the demultiplexed train, since the LNO used as the reference operates at 2.56 GHz.

Nevertheless the opposite of the effect described in Section 3.4.2 can be used to estimate $\mathcal{L}(f)$. The power spectral density of phase noise increases as the square of the harmonic number at which it is observed [100]. Figure 3.42 shows the photodetected RF spectra at various frequency harmonics, where the x-axis is the frequency offset at each harmonic. Although that at 4.8 GHz, or the N = 60th harmonic of the 80 MHz pulse train, the noise is increased by 60^2 = 35.6 dB compared to the frequency of the 80 MHz pulse train, there is no significant feature visible other than the instrument's noise floor. Thus using (3.16), the 95 dBc/Hz signal to noise ratio, shown in Figure 3.42, at the 60th harmonic corresponds to signal to noise ratio = 130.6 dBc/Hz at 1 kHz offset for the 80 MHz tone. At 1 kHz offset from the carrier, Figure 3.41 (a) shows that the residual phase noise power spectral density is at -134 dBc/Hz. That means that the residual phase noise has not significantly increased during the time demultiplexing and can safely be considered unaffected by the time demultiplexing performed.

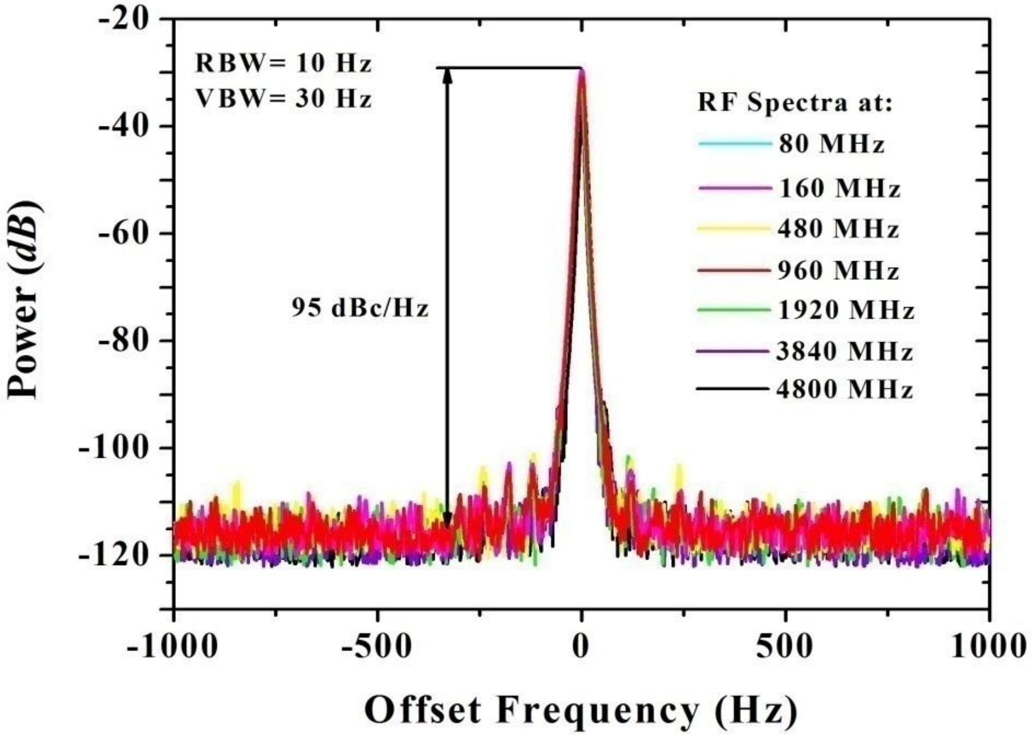

Figure 3.42: RF Spectra of the photodetected pulse train at various harmonics. The von der Linde method [24] for estimating the timing jitter verifies that timing jitter of the time demultiplexed pulse train has not significantly increased. Note that although the phase noise is increased by 35 dB compared to the 80 MHz train at the 60th harmonic, there are no visible features rising from the noise floor of the measurement.

As a conclusion to this work, the performance of the laser system developed is related to the requirements for a laser source of time-stretch (TS) photonic ADC as proposed by Han and Jalali [56]. In TS ADC the bandwidth of an input RF signal can be effectively reduced by the stretching in time of the photonically sampled signal. As an example, a single-shot implementation of an ADC system having an instantaneous bandwidth of 5 GHz can be attained using a TS architecture with 62.5 times stretch factor resulting in an 80 MHz effective bandwidth. The ENOB = 17.1 [29], considering only the phase noise restriction [105]. Actually the ENOB of the described ADC system will be 12.5 as dictated by the AM noise of the optical pulse train. On the other hand, for a continuous TS system [105] with the same performance characteristics, the timing jitter constraint is defined by the stitching of the digitized segments that is performed at the back end of the system and the bandwidth constraint of the signal cannot be reduced to the effective bandwidth of the TS system [106]. Hence, for a continuous TS architecture having a bandwidth of 5 GHz the resulting ENOB = 12.1, which is based on the ultra-low noise performance of the developed MLL. In both cases, the time demultiplexed pulse train generated can support a high bandwidth, high ENOB photonic ADC system implementation.

3.4.5 Conclusion on the Time Demultiplexing Experiments

A semiconductor-based harmonically MLL with low integrated amplitude and timing jitter is developed and time demultiplexed to 80 MHz, the cavity fundamental frequency of the laser cavity. The AM noise of the ring laser is 0.0125 % and the integrated timing jitter is 8 fs over the integration band (1 kHz - 40 MHz), while the spectral bandwidth of the laser is 25 nm (full width at 20 dB). The time demultiplexed 80 MHz pulse train has 0.017 % AM noise, integrated from 1 kHz to 40 MHz, the Nyquist limit of the pulse train. The phase noise of the time demultiplexed pulse train was proven to be unaffected by the demultiplexing process and it is on the order of 8 fs integrated over the same band. The WPE of the system is 4 %, considering only electro-optic components. The ENOB that the demultiplexed pulse train can achieve for use in a continuous TS photonic ADC architecture is limited by the timing jitter of the high repetition rate laser to $\mathrm{ENOB}_{80\mathrm{MHz}} = 12.1$.

The presented 80 MHz, ultra-low noise laser pulse train can be used in a high bandwidth TS photonic ADC architecture system, for all-optical switching and for any application demanding ultra-low pulse-to-pulse energy or timing jitter.

3.5 Mode Partition Noise of Periodic Electric Signals

3.5.1 Introduction

Periodic electrical signals having low amplitude noise have been in use in the field of optical communications and signal processing providing the driving signal for photonic signal gating and generation [107]. The noise of the driving electrical signal is additive to that of the optical wave, leading to degradation of the noise characteristics of the output optical pulse train. Moreover, periodic electrical patterns can be used in radar applications and in testing of photonic network components. Thus, accurate characterization of the amplitude modulation (AM) noise properties of periodic electrical signals is critical for the development of low amplitude noise microwave and photonic applications.

Limited information on the quality of periodic electrical signals can be extracted by examining their time intensity profiles, or eye diagrams, generated by high-speed (sampling) oscilloscopes. However, both the speed of those instruments and their accuracy are limited and depend on the analog-to-digital converter (ADC) used.

The relative variance of the amplitude noise of optical pulse trains, the photonic equivalent of periodic electrical signals is calculated using:

$$\sigma_{\mathrm{A}mpl.} = \sqrt{2 \cdot \int_{1/t_{observation}}^{Nyquist} \mathrm{M}(f) \cdot df} \tag{3.17}$$

M(f) is the (Nyquist zone filtered) single sideband (SSB) power spectral density (PSD) of the RF power spectrum at the fundamental frequency of the photodetected optical pulse train. The theory developed in [100] proves that the amplitude noise on the fundamental (as well as on all other harmonics) of the photodetected signal is an accurate representation of the amplitude noise of the optical pulse train. The photodetected SSB technique has large dynamic range and ultra-low AM noise of mode-locked lasers has been measured.

When M(f) is measured directly by using the fundamental tone of periodic *electrical* signals, such as signals generated by pattern generators, the technique fails due to the fact that the noise appearing as sidebands at the electrical tone is not solely due to the noise of the complete signal. In this work, we show experimental results that prove that part of the noise on the measured M(f) is noise anti-correlated, having 180^o phase difference, to other harmonic tones of the RF spectrum. This effect has an optical equivalent named mode partition noise (MPN) [84]. MPN is removed in the optical experiment due to the effective mixing induced by the photodetector. Moreover, we propose and demonstrate a technique using *photonics* that enables the accurate measurement of the SSB noise for periodic electrical signals. The experimental results furthermore prove the existence of anti-correlated noise between the frequency components of the periodic electrical signal.

3.5.2 Mode Partition Noise of Electrical Signals

In this work, the device that is used to generate electrical signals is a commercially available electrical pattern generator (PG). The PG is triggered by a low noise, 2.56 GHz signal. The PG is set to have 32 time slots programmed to output either 0 V or 2 V. Thus, both the duty cycle and the repetition rate of the generated signal can be adjusted using the PG.

The AM noise single sideband PSDs are measured from the electrical signal. The Nyquist frequency zone at the fundamental frequency of the electrical signal is *filtered, using the appropriate RF filters,* and M(f) is measured using an Agilent E5500 series noise measurement testset.

The possibility of applying the direct SSB frequency technique for measuring the AM noise of periodic electrical signals is first examined. Figure 3.43 shows M(f) for various duty cycles, as measured at the fundamental frequency of 80 MHz for square waves. Although the shape of M(f) is preserved for all duty cycles its level relative to the carrier changes as a function of the duty cycle. The change has a nonlinear dependence on the duty cycle and there is a ~20 dB increase of M(f) between duty cycles of 50 % and 6.25 %.

The dependence of the PSD on the duty cycle could be attributed to some internal function of the PG which would make short in duration pulses more prone to noise. However, M(f) is unaltered for pulses having variable time duration when the duty cycle is fixed to 50 %, as seen in Figure 3.44. It should be noted that the 50 % duty cycle pulses having 1.28 GHz repetition rate have the same time duration (~390 ps) as the 80 MHz pulses having 6.25 % duty cycle. This strongly suggests that the dependence of the PSD level of the periodic electrical train on the duty cycle is an artifact of the measurement method.

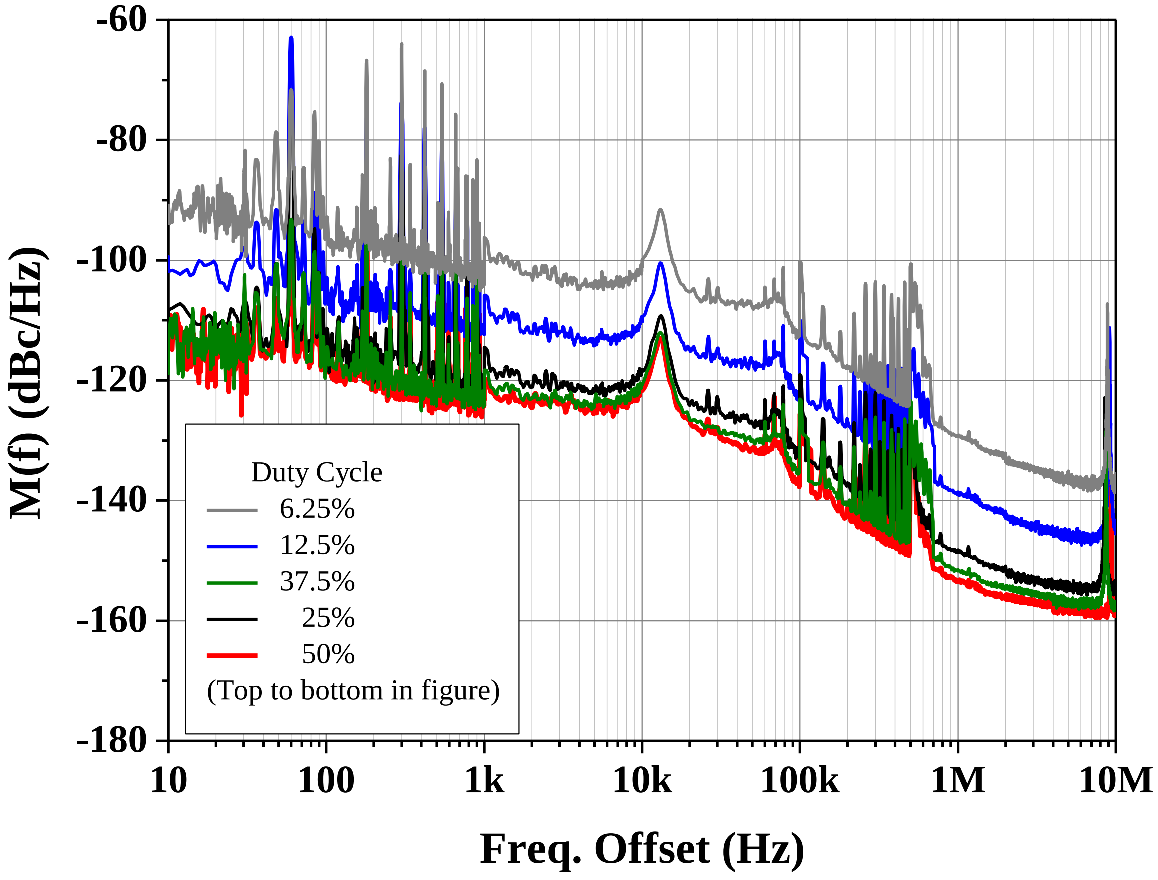

Figure 3.43: Single sideband power spectral density of amplitude modulation noise of square electrical waves having 80 MHz repetition rate for variable duty cycles.

The increase of the AM noise PSD with decreasing duty cycle of the electrical signal presented in Figure 3.43 is attributed to the existence of correlated electrical MPN. Part of the noise appearing on the RF spectrum of each harmonic tone of the signal can be correlated with noise in another tone. Anti-correlated noise at different frequency components, noise having 180° of phase difference, results in reduced noise of the composite signal although it is accentuated in the PSDs of individual RF components.

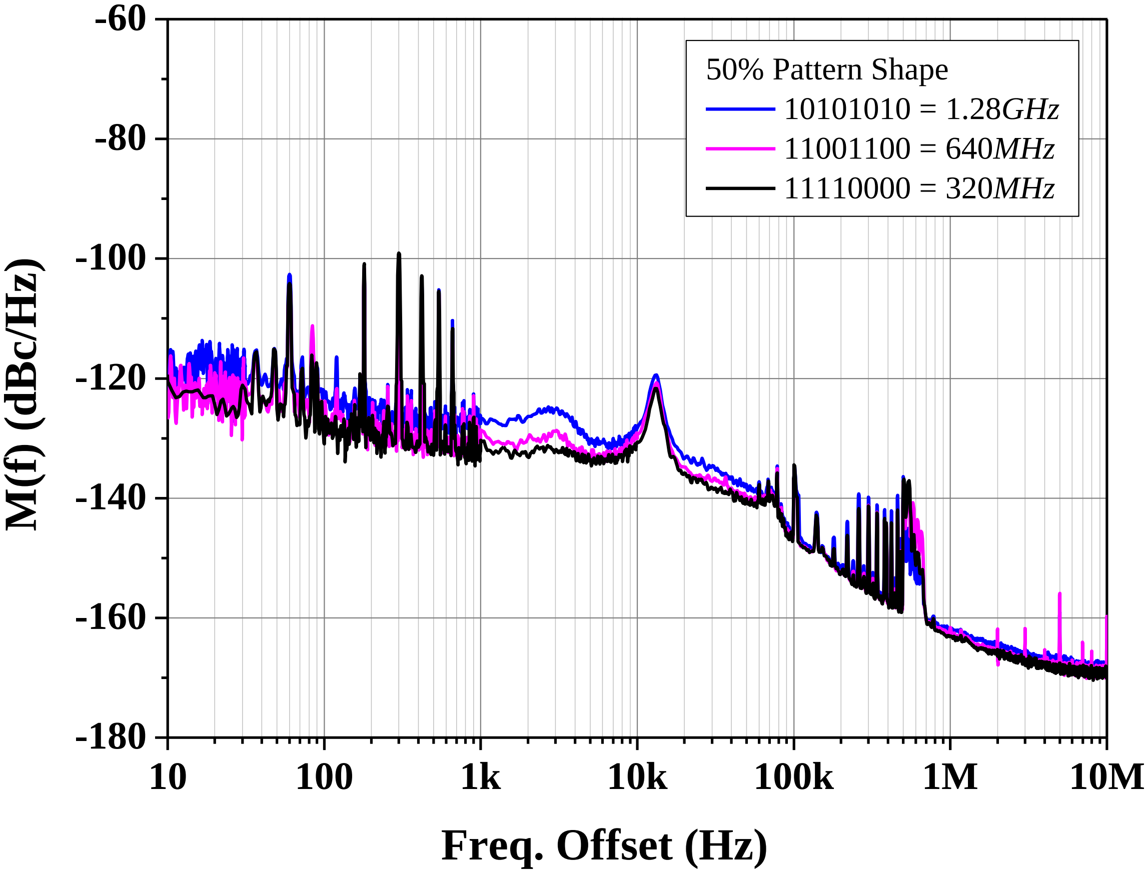

Figure 3.44: Single sideband power spectral density of amplitude modulation noise of square electrical waves created using an electrical pattern generator having 50 % duty cycle and different open gate duration.

The increase of the MPN with reduced duty cycle can be qualitatively explained using Figure 3.45. Square waves with a duty cycle tending to 50 % are comprised by a smaller number of RF tones with significant power, compared to waves of lower duty cycles, as dictated by Fourier transform properties. Therefore, a low duty cycle periodic signal allows more noise to appear about a single frequency component since the correlation between components may allow overall noise suppression in the composite signal. The PSD of the 50 % duty cycle square wave should be closest to the accurate representation of the periodic signal's PSD.

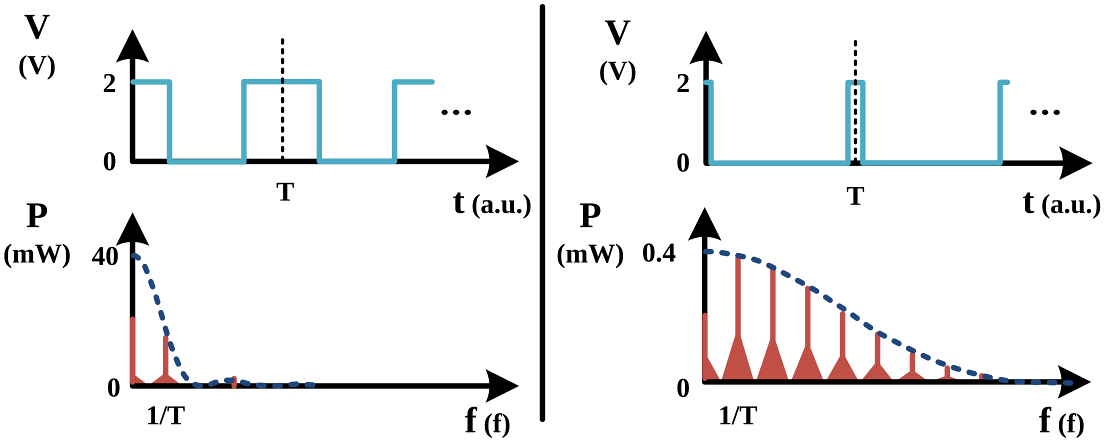

Figure 3.45: Schematic representation of the time voltage profile (top) and RF spectral power (bottom) of a 2 V return-to-zero square wave for 50 % (left) and 10 % duty cycles (right).

Consequently, applying the direct SSB technique for calculating the AM noise of periodic electrical signals may lead to results that overestimate the actual noise of the signal. In the following section we present and experimentally demonstrate a photonic method that enables the SSB frequency technique to be used for measuring the AM noise of periodic electrical pulse trains.

3.5.3 Photonic Noise Measurement Technique

As discussed in Section 3.5.1 integrating M(f) yields accurate results when used to measure the noise of photodetected optical pulses. To enable the use of this technique for periodic electrical signals we introduce a photonic up-convert and down-convert setup, as seen in Figure 3.46. The periodic electrical signal is up-converted to an optical carrier by modulating the light intensity of a continuous wave (CW) laser. When the peak of the electrical signal is at the quadrature point of the intensity modulator, which has a linear slope, the AM noise of the electrical signal is also up-converted. Subsequently, a photodetector is used to down-convert the signal back to the electrical domain. As seen in Figure 3.46, both the time intensity profile and the RF spectrum of the final signal appear unaltered compared to the electrical square wave signal. Nonetheless, the noise of the down-converted electrical signal differs from the noise of the initial electrical signal as a result of the photodetection.

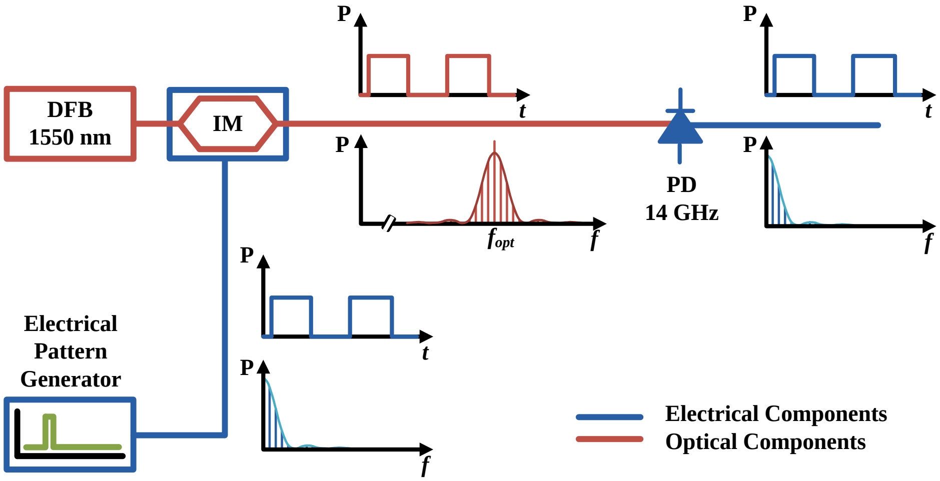

Figure 3.46: Experimental setup. The RF spectrum of the photodetected signal has the same functional form as that of the pattern generator but different noise properties. IM: Intensity Modulator; DFB: Distributed Feedback Laser; PD: Photodetector.

The photodetector's output is proportional to $E \cdot E^{*}$, the intensity of the optical signal. Particularly, the photodetector acts as an optical frequency mixer, multiplying the incident ultrafast electrical field with its conjugate. The mixing process creates sum and difference frequencies and down-converts the optical signal, since neighboring optical tones are separated by the fundamental frequency (f_{fund}) of the electrical signal. Hence, the generated tone at f_{fund} of the photodetected output is effectively formed by the mixing of all the neighboring components of the optical spectrum. This allows correlated noise to add or cancel depending on the relative phase between neighboring frequency components [100].

The proposed optical setup is used to measure the SSB noise PSD of square waves of variable duty cycles at 80 MHz, as in Section 3.5.2, and the results are shown in Figure 3.47. There are significant differences between Figure 3.43 and Figure 3.47, which show M(f) for the electrical and the photonic measurements respectively. At low frequency offsets from the carrier, M(f) is independent of the duty cycle, in contrast with the direct measurement of the electrical RF tone presented in Figure 3.43 This is in accordance with the expectations of the up-convert and down-convert experiment proposed and it proves that the excess noise for small duty cycle signals of Figure 3.43 is due to correlated MPN. For example, the strong peak at ~10 kHz shown in Figure 3.43 is suppressed in Figure 3.47, which indicates that this is a correlated noise peak. Moreover, M(f) seems to be at levels comparable to the 50 % duty cycle direct measurement experiment which verifies that the optical measurement yields the actual AM noise PSD of the periodic electrical signal.

Furthermore, it should be noted that all measurements reach a plateau at frequency offsets greater than 10 kHz. This is because at those offsets the measurements are below the noise floor of the Agilent measurement setup. The relatively low RF power at the fundamental frequency generated using the photonic technique results in a disproportionately large increase of the noise figure of the measurement setup used. This is because the up-convert and down-convert procedure is power inefficient due to the limited photocurrent generated by the photodetector.

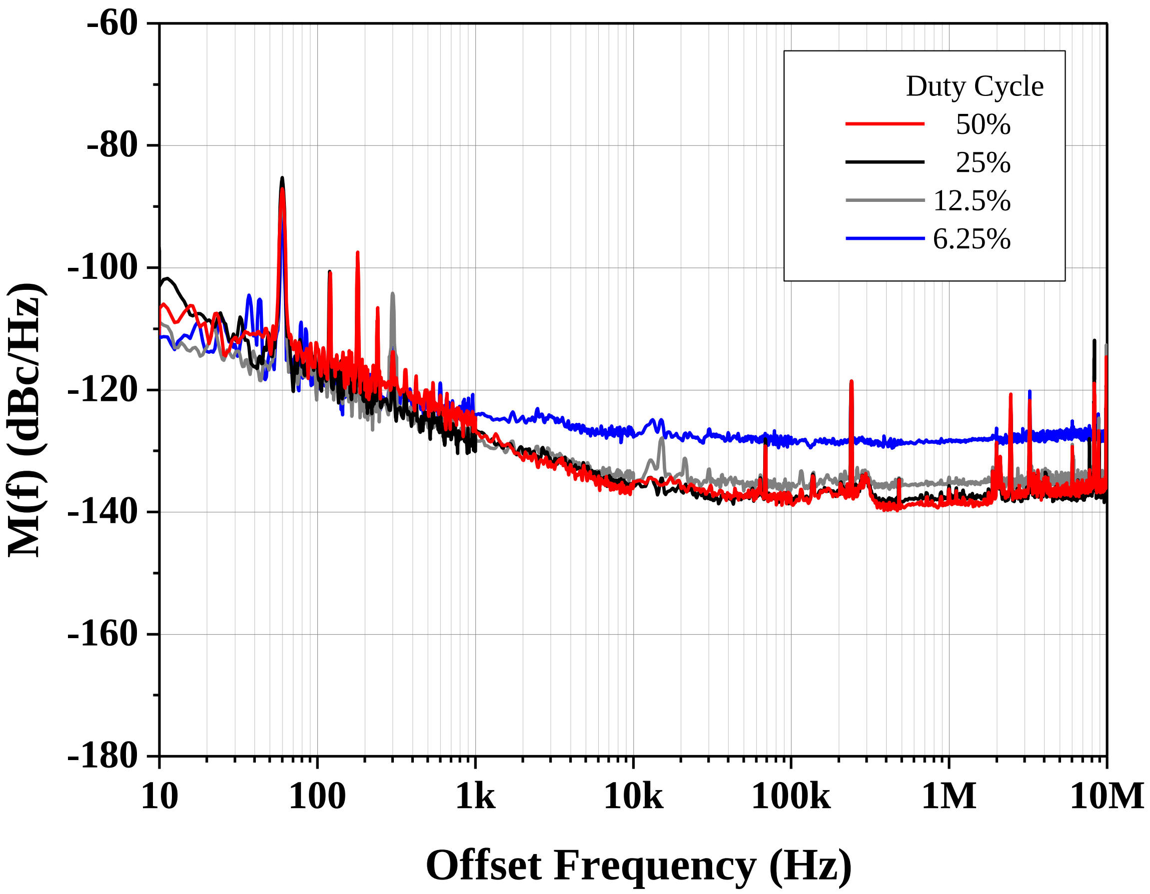

Figure 3.47: Single sideband power spectral density of amplitude modulation noise of up-convert and down-convert signal. The graphs are limited by the noise floor of the measurement for frequency offsets > ~10 kHz.

Nonetheless, the suggested technique has the potential to provide gain through optical amplification which can improve on the dynamic range of the measurement. Specifically, amplification of ultra-fast electrical signals is challenging due to their broad frequency content, however when signals are up-converted to an optical carrier the relative bandwidth of the signals is reduced, allowing narrow-band amplifiers, such as Erbium doped fiber amplifiers, to be used.

Future advancements in the fields of intensity modulators (insertion loss) and photodetectors (generated photocurrent) can significantly improve on the proposed technique.

Note that a similar technique can be proposed that uses an RF mixer to perform the mixing of neighboring components. Nevertheless, the apparent convenience of using a mixer is invalidated by considering the specifics of the experiment. The mixer has to be saturated for all frequency components that vary significantly in power. In addition, the conversion loss of the RF mixer limits the generated power. For example, under the same conditions as the experiment described in 3.5.2 the power at f_{fund} of the RF mixed signal is attenuated in excess of 15 dB compared to the photodetected signal. The reduced power at f_{fund} is detrimental for the dynamic range of the setup giving much higher noise floors compared to Figure 3.47.

3.5.4 Conclusion on the Noise of Periodic Electrical Signals

This work demonstrates the challenges of acquiring AM noise measurements of periodic electrical signals using the direct SSB technique. The variation of the AM noise PSD was shown to be ~20 dB for a square wave with variable duty cycle. This effect is attributed to correlated noise of the frequency components composing the signal. Subsequently, the electrical signal was up-converted to an optical carrier and the SSB noise PSD of the photodetected signal was acquired. The resulting PSDs show no dependence on the duty cycle and both prove the existence of correlated MPN in the direct measurement technique and contain the accurate AM noise for the full periodic electrical signal.

3.6 An Electro-Optic Feedforward System for Dynamic Control of a Quasi-CW Chirped Laser Source

3.6.1 Introduction

In the last few decades, communication links have switched from analog to digital schemes allowing for essentially lossless transfer of information [108]. Information is converted to the digital format and it is transferred through a medium, such as optical fiber or air, via electromagnetic radiation. At the end the information is converted to the analog format, if needed. Currently, for commercial applications, the ADC is performed using electronic technology.

The performance of modern electronic analog-to-digital converters is limited by timing and amplitude jitter, the duration of the sampling gate, thermal noise and comparator ambiguity [29]. Photonic ADC, which uses optical technology, has the potential of surpassing the speed of conventional electronic ADC. Sampling gate time durations on the order of picoseconds or shorter are easily achieved using optical pulses and optical pulses with improved timing and amplitude jitter compared to that of electronic gates have been demonstrated [99], [109]. In addition, numerous methods of photonic ADC have been demonstrated [28].

This letter focuses on the TS photonic-assisted ADC architecture [56]. In this approach, a linearly chirped laser source with low amplitude and timing jitter is needed and previous work has depended upon the stretching of ultra-short pulses for signals with limited time duration. Due to the extreme chirp, *frequency-to-time* mapping is observed, which means that the temporal intensity profile of the stretched pulses follows the shape of the optical spectrum. For continuous operation of the TS photonic ADC a chirped laser source that covers the time interval between the pulses is needed. Also, pulses having uniform temporal profile are advantageous for the system, since equalized time profiles demand less calibration and reduce crosstalk between adjacent pulses.

A novel cavity design called the Theta laser cavity, which uses chirped pulse amplification within the laser cavity, has been demonstrated providing the chirped pulses directly from the laser cavity and having a quasi-uniform optical spectrum that covers the time interval between the pulses [110]. The Theta laser is suitable as the laser source for TS photonic ADC, providing the required linearly chirped output; however it suffers from non-uniform optical spectra, which translate into modulation of the temporal intensity pulse profile.

A feedforward system broadening the full-width half max of a Gaussian-shaped intensity time profile has been demonstrated by Cundiff et al. [111]. This work goes beyond the initial demonstration by Cundiff et al. by identifying key experimental parameters which must be satisfied in order to achieve broadband operation needed for the dynamic control of square-shaped optical spectra. In addition, the work presented in this section experimentally measures and verifies the system’s overall broadband response. The broad frequency response feedforward system developed is capable of dynamically equalizing the time profile or spectral shape of a quasi-CW chirped laser source suitable for continuous TS photonic ADC. Analysis of the feedforward system’s performance reveals the limitations on the system’s response and dynamic range.

3.6.2 Experimental Setup

The feedforward system developed uses the voltage response of an electro-optic amplitude modulator. When a time-varying voltage representation of the input optical signal is generated and applied appropriately to the modulator it can reduce the transmittance of the higher intensities of the signal as compared to that of the lower intensities, increasing the uniforminty of the signal (Figure 3.48).

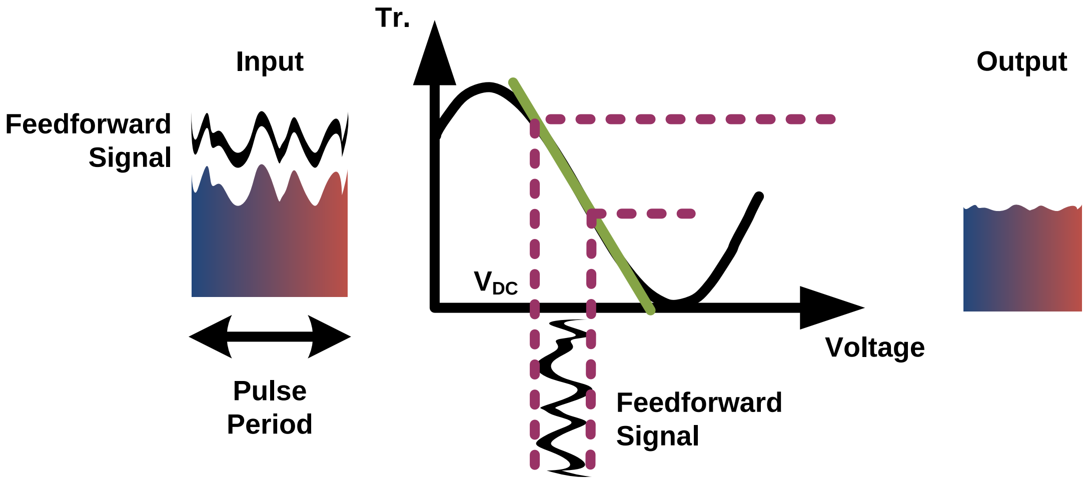

Figure 3.48: Conceptual representation of the feedforward system. The temporal variation of the signal is reduced when a voltage copy of the variation of the signal drives an amplitude modulator. V_{DC}, DC Voltage supplied to the amplitude modulator; Tr., the transmittance of the amplitude modulator

In the scheme developed, shown in Figure 3.49, the quasi-CW pulse train generated by the laser is split by a directional coupler. Part of the laser beam is delayed using optical fiber and a variable optical delay line, while the other part of the input is amplified using an EDFA and photodetected by a wide bandwidth photodetector, which converts the optical intensity to an electrical signal. Subsequently, the electrical signal is amplified and changes the transmittance of an electro-optic amplitude modulator. By optimizing the DC voltage on the modulator and the amplitude of the electrical signal, the feedforward system can attenuate the peaks of the intensity more than the valleys, resulting in an improvement of the uniformity of the temporal intensity profile and the optical spectrum, due to the time-to-frequency mapping of the signal.

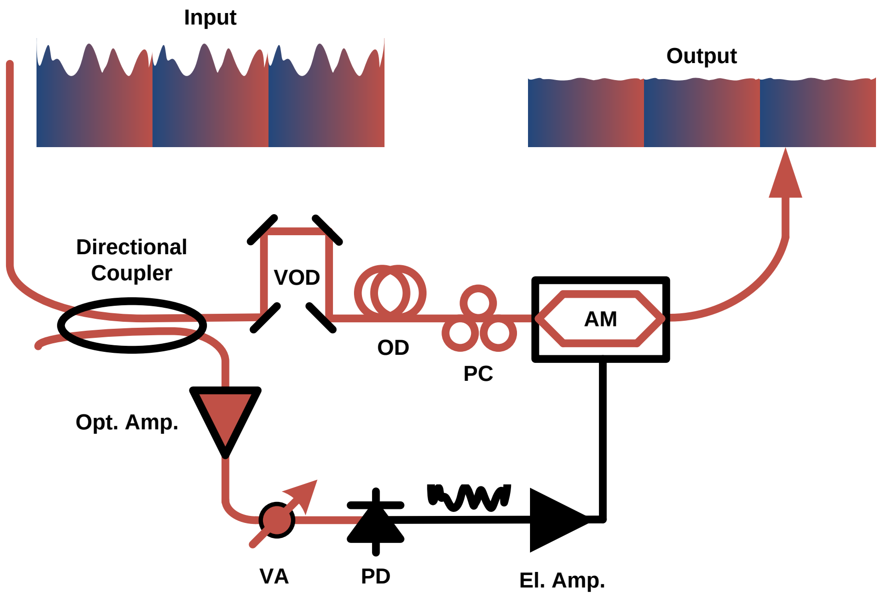

Figure 3.49: Feedforward system for equalizing the temporal intensity profile. PD, photodetector; PC, polarization controller; AM, electro-optic amplitude modulator; VOD, variable optical delay; OD, optical delay; VA, optical variable attenuator.

The two arms of the system must be synchronized. The system is an electro-optic interferometer, thus any mismatch of the time delay between the two arms will lead to a sinusoidal frequency dependence of the system response, with nulls spaced by the inverse of the temporal difference between the two arms. A mismatch between the two arms of the system would mitigate the frequency response of the system disabling the equalization of square-shaped spectra, unlike with Gaussian-shaped spectra which require a narrowband frequency response.

Moreover, for the system to both be able to use the linear region of the transmittance of the modulator and have sufficient dynamic range, the peak to peak voltage of the voltage signal input to the modulator has to be on the order of the V_π of the amplitude modulator.

To avoid causing nonlinearities coming from the response of the modulator that can reduce system performance, the system should be operated in the quasi-linear region of the modulator's transmittance. For ± 5 % of difference between the sinusoid transmittance and the linear approximation, the maximum electrical signal amplitude is approximately V_π / 2, which corresponds to 72% of the full dynamic range of the system. An amplitude modulator with linear response would significantly improve on the dynamic range of the system.

3.6.3 Experimental Results

The system was tested using the stretched pulses generated using a Theta laser operating at a pulse repetition rate of 105 MHz, using a chirp fiber Bragg grating with 1981 ps/nm dispersion, as described in [110]. The pulses are 9.5 ns apart and the corresponding spectral bandwidth that would fill the time duration between the pulses is 4.8 nm. In order to have control upon the spectral shape of the Theta laser output to demonstrate the effectiveness of the system the pulses created had 2.6 nm of spectral bandwidth with pulse duration of 5.1 ns.

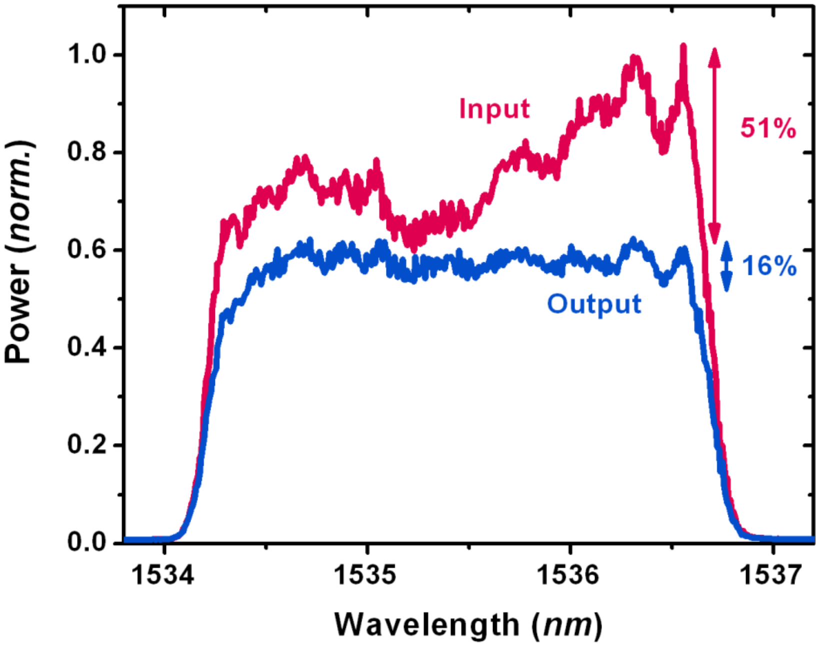

Figure 3.50: Spectral flattening of a chirped laser pulse. The contrast of the input, optical spectrum to the system is 51 % (red curve), while the output spectrum has contrast of 16 % (blue curve).

The result of the output of the developed feedforward system is shown in Figure 3.50. The *contrast* is defined as the ratio of the intensity modulation of the quasi-uniform part of the optical spectrum to its average, which is a measure of relative spectral uniformity.

$$Contrast = \frac{\max - \min}{(\max + \min)/2} \tag{3.18}$$

The contrast of an input chirped pulse is improved from 51 % to 16 %, a 3.1 times improvement. The remaining modulation of the spectrum is due to fast varying components of the optical spectrum, which is an indication that the system’s response is non-uniform for all frequencies. Exploring the frequency response can provide additional insight on the process.

3.6.4 Frequency Response Characterization

The frequency response of the system was characterized using the setup shown in Figure 3.51. The feedforward system was probed by a single-mode continuous wave laser modulated with a 30% depth of modulation sinusoidal signal, using an electro-optic amplitude modulator and the response of the system was recorded as a function of the modulation frequency. In particular, the output of the system was photodetected and the power of the RF tone at the modulation frequency was measured with and without the feedforward system. The difference between the two states is defined as the *suppression* of the feedforward system for that frequency input.

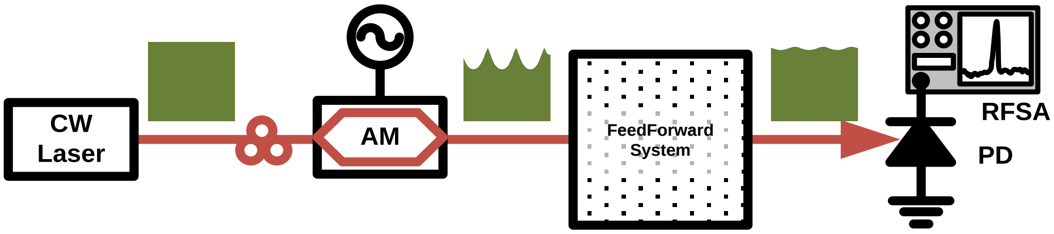

Figure 3.51: Setup for measuring the frequency response of the feedforward system. PD, photodetector; AM, electro-optic amplitude modulator; RFSA, radio frequency spectrum analyzer.

The system's suppression was optimized for 1 GHz operation, yielding a maximum suppression of 34 dB. Suppression was then measured for frequencies varying from 0.33 – 5 GHz. Figure 3.52 shows the results of the measurement superimposed with the gain of electrical amplifier used for an input of -15 dBm which is the power typically generated by the photodetector under the operating conditions of the conducted experiments.

The suppression at frequencies higher than 1 GHz is nearly constant at 18.5 dB, while at frequencies lower than 1 GHz, the suppression varies between 14 dB and 20 dB. Note the connection between the variation of the gain of the amplifier and the variation from nominal suppression.

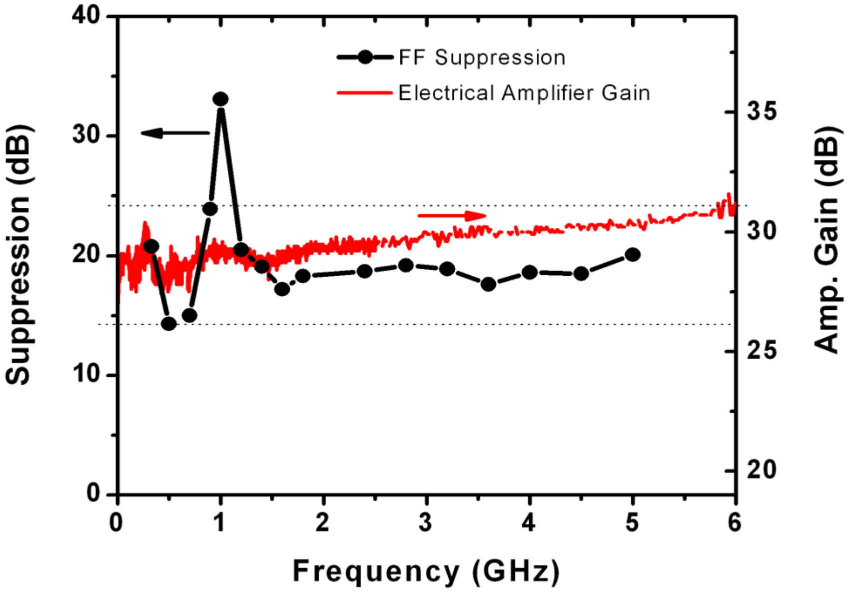

Figure 3.52: Frequency Response of the feedforward system and gain of the electrical amplifier used (Input power = -15 dBm). The system's response is optimized for 1 GHz.

As mentioned, the feedforward system is an electro-optic interferometer and for optimal performance, both the path length difference between the two arms (relative time delay) has to be minimized and the voltage applied to the amplitude modulator must be precisely adjusted. Moreover, the system's suppression is a logarithmic function of a vanishing function of both the voltage applied to the amplitude modulator and the path length difference of the two arms of the system. Therefore a small variation of either parameter has a significant impact on the suppression. For the broadband feedforward system described in this work any variation of the voltage applied to the modulator or the time delay from that of the optimized frequency will lead to a decrease of the suppression compared to that of the optimized frequency. Variations of the voltage are due to the frequency dependence of the electrical amplifier's gain and RF cable loss, while variations of the path length difference can be attributed to dispersion of the signal at the different parts of the system. As a result, the system developed can suppress a certain frequency more effectively than others and has to be optimized for any given input signal. However, for a repetitive signal, similar to the experiments presented in this work, this optimization procedure is only required once.

Usually, the spectral shape input to the system has a dominant pattern of a certain period (or spectral width, $\Delta\lambda_{Dominant}$). Given that, the frequency response of the feedforward system ($f_{el,FF}$) can be adjusted, using the following relation derived from the time-to-frequency mapping of the signal:

$$f_{el.,FF} = f_{rep} \cdot \frac{\Delta\lambda_{FWHM}}{\Delta\lambda_{Dominant}}, \tag{3.19}$$

where $\Delta\lambda_{FWHM}$ is the full width half maximum of the optical spectrum that would fill the laser's period and f_{rep} is the pulse repetition rate of the laser.

Suppression of more than 30 dB was achieved for all tested frequencies by optimizing the variable optical attenuator that controls the voltage input to the modulator.

3.6.5 Conclusion on the Feedforward System

A dynamic electro-optic feedforward system is designed and implemented for equalizing the optical spectrum (temporal intensity profile) of a linearly chirped laser source. The output spectral uniformity was improved by reducing the temporal modulation from 51 % to 16 %, a reduction of over threefold. Broadband frequency response of the system is experimentally demonstrated enabling the equalization of uniform linearly chirped pulses that can be used as an alternative source for photonic ADC or for optical coherence tomography.

FUTURE WORK

This section describes the suggested paths that the student's work may lead in the near and long-term future.

- One approach that will be pursued is the incorporation of a Slab-Coupled Optical Waveguide Amplifier (SCOWA) in the Theta laser instead of the commercially available SOA used in the experiments of section 3.2. SCOWAs have been demonstrated with up to 20 times the saturation power compared to the SOA used. However, they show reduced small signal gain. The small signal gain of the SOA used is ~28dB, while the SCOWAs have been demonstrated with gains of up to ~23dB. Thus for a laser cavity architecture such as the Theta laser, the total loss of the cavity may be difficult to overcome with a SCOWA. The loss of the simplest implementation of the Theta laser is ~15 dB, as seen in Figure 3.6. Moreover, the incorporation of a saturable absorber in the Theta laser, possible based on SCOW technology, will significantly improve the quality of the laser pulses, and shorten their pulse duration.
- Another future direction for the Theta laser, is that of a coupled opto-electronic oscillator approach for the Theta laser. In this approach, the compressed port output of the laser is photodetected and that pulsed signal is used to drive the modulator. This may make the laser will be easier to align, but also may lead into the abandonment of the noise electrical comb generator used in the laser architecture so far.

- The modified intra-cavity Hänsch-Couillaud technique can be used for referencing the etalon to a laser with Erbium fiber gain laser operating at ~10 GHz. Although this laser design has been demonstrated [112], it lacked a long-term referencing mechanism. Without a long-term locking mechanism this laser could not be used for applications. The passive HC technique can provide a signal for long term referencing with minimal power consumption.
- The stretched dual port output of the Theta laser is ideal for studying the effect of mode partition noise on the optical pulses. Although the pulse-to-pulse energy fluctuation characterized by the AM noise of the compressed pulse train can be suppressed, the stretched port pulses have demonstrated increased intensity modulation.

  This can be explained by the mode partition noise effect, in which different spectral components are allowed to exchange power on a pulse-to-pulse basis, while maintaining a fixed total power. The intra-cavity etalon is expected to mitigate this effect and it will be further investigated.

- Another approach that should be pursued is the further improvement of the etalon characterization scheme. Etalons with ultra-high finesse ($>10^4$), correspond to resonance windows in the kHz range. Thus for the modified PDH setup to work, the narrow-linewidth laser center frequency must be accurately fixed. This can be attained by using a common laser in two different setups, both using opposite ports of one etalon. The laser frequency is stabilized to the etalon and the laser (frequency shifted using an AOM) can probe the resonance to achieve high precision in the FSR measurement.

- The Theta laser with the intra-cavity etalon is unique linearly chirped laser source with pulses filling the period of the laser. With the intra-cavity etalon, it becomes a robust laser that can be used in a multiplicity of applications, such as laser ranging, optical coherence tomography and photonic analog-to-digital conversion.

- Diode lasers usually have reduced intra-cavity (peak) power compared to their solid-state counter parts, due to the low saturation power of semiconductor gain media. Nonlinearities induced by pulses emitted by diode lasers cannot be attained due to their low peak power output. It should be noted that the efficiency of nonlinear processes increases quadratically with peak power. The power from diode lasers can be significantly enhanced when an intra-cavity etalon is used. Etalons act as energy storage mechanisms, enhancing the power within them, for any given input power. A finesse of 100, results in an enhancement of the electric field (peak power) by similar factor, which implies that the efficiency of nonlinear effects can be enhanced by 10,000 times. Nonlinear effects start to be significant in semiconductor media in the 1 kW power range. An average power in the order of 0.1 W for 10% duty cycle pulses can show nonlinearities, in semiconductor samples. Thus, placing the appropriate nonlinear material at the etalon beam waist (or anywhere within the fiberized etalon) can enable the use of a plethora of intra-cavity nonlinear effects. Spectral broadening can be attained through self-phase modulation, while saturable absorption can result in temporal pulse shortening.

APPENDIX A:

CHIRPED FIBER BRAGG GRATING SPECIFICATION

This section presents the performance characteristics of CFBGs and demonstrates the necessity for high quality CFBGs for X-CPA and applications. The differential temporal delay between the wavelength components, required for X-CPA for pulses stretched to the 10 ns period regime, using lasers with bandwidth in the order of 10 nm, is extremely large. The dispersion needed is in the order of 1 ns/ nm, which corresponds to a differential path length of 20 cm/nm in fiber.

Using single mode fiber (SMF), which has ~17 ps/nm/km dispersion, one would need 60 km to reach 10 ns in pulse duration. Moreover, most X-CPA applications also require availability for complimentary dispersion to that used for the stretching. To provide complimentary dispersion for SMF, dispersion compensating fiber (DCF) must be used, which has approximatelly -10 times the dispersion of SMF. However, the group delay spectral profile of DCF does not match SMF for all wavelength components, which makes complimentary stretching and compressing for X-CPA challenging. Thus, CFBGs arise as the prevailing technology for providing large dispersions and are essential components for extremely chirped pulse generation and appplications.

On the other hand, CFBG development faces its own challenges and the state of the art demonstrations of X-CPA are limited by the current CFBG technology. It should be noted that 1 ns/nm which can translate to a 10 ns differentail group delay for 10 nm of spectral separation, corresponds to 0.2 m of spatial separation in fiber. To attain broadband reflection, current vendors use combined narrowband gratings individually recorded using interferometric techniques. The detrimental results of this effect are depicted in Figure A.0.1, where typical performance for a commercially available CFBG is shown. Both the insertion loss (reflectance) and the group delay demostrate periodic modulation due to the grating stitching process.

The group delay ripple of a CFBG presented in Figure A.0.1 (b), is defined as the higher order group delay modulation, with the designed linear group delay reduced. Imperfections on the CFBG manufacturing result in residual group delay, which is the group delay sum of the two complimentary grating ports.

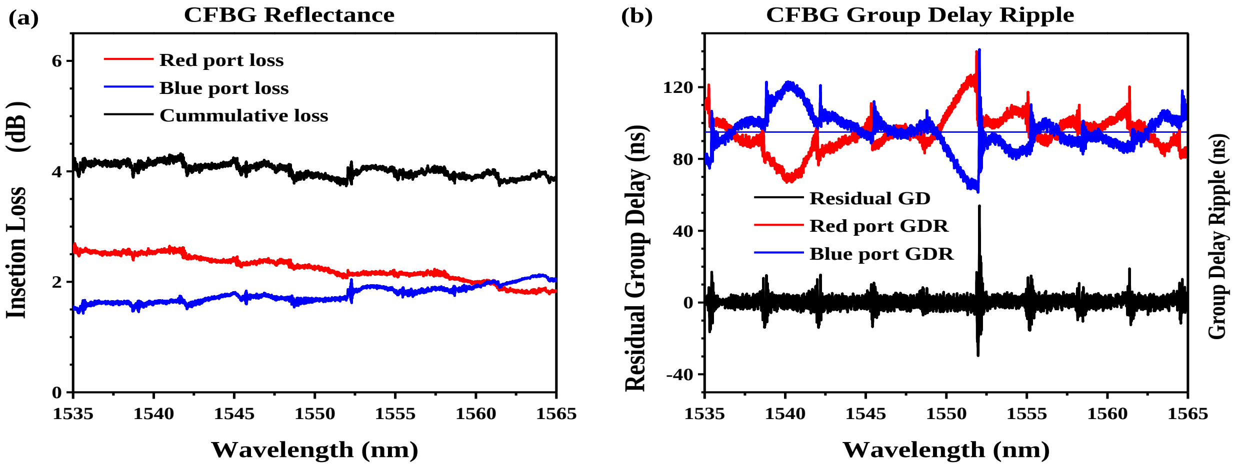

Figure A.0.1: Commercially available CFBG characterization. (a) Insertion loss. (b) Group delay ripple and round trip residual group delay. The GDR plots are also centered on zero and have been shifted for viewing purposes. Grating dispersion 991 ps/nm. The grating presented in this graph is used for the implementation of the Theta laser presented in section 3.2.

In the Theta laser, which operates in a breathing mode architecture, the residual group delay has essential contribution on the laser performance. It should be noted that in the Theta laser design, a pulse that propagates along the laser cavity accumulates the residual group delay for a single round-trip. The resulting phase (timing) noise imparted on the optical pulses results into the observed coherence spike of the laser second harmonic autocorellation trace. This effect is the timing analog of intensity modulation noise, as presented in [113]. It should be noted that when lasing bandwidth is confined to <<1 nm, the autocorellation traces do not show coherence spikes, which further prooves the concept. Moreover, pulse broadening for the compressed port output is due to the residual group delay of the CFBG used.

Future advances in CFBG technology can significantly improve on the performance of X-CPA oscillators and applications.

APPENDIX B:

VARIABLE OPTICAL DELAY BALANCING ROUTINE

In the work described in 3.2, where an etalon is inserted into a Theta laser, a balancing routine is required. The FSR of the etalon has to match an integer multiple of the laser's fundamental frequency, or vice versa, the optical path length of the laser cavity has to be an integer multiple of the etalon's optical path length. The fiberized etalon has an FSR ≈ 99.58 MHz which, assuming an index of refraction for the optical fiber n = 1.4682, corresponds to ~2.052 m of fiber (3.013 of optical path length). To be able to match the cavity length to an integer harmonic of the etalon length without changes, translates into having the ability to add one more pulse in the laser cavity. Although this is fairly easy for a 10 GHz laser, since 10 GHz corresponds to a dynamic range of ~2 cm, attaining 2 m of dynamic range from a high resolution optical variable delay is challenging. The details of the high resolution and high dynamic range optical delay built are described in 3.2.

As described in 3.2, the error signal generated for the long-term stabilization feedback mechanism is applied to the high speed optical phase shifter (OPS), purchased from General Photonics, which has a limited dynamic range (8-10 μm). The point of this routine is to extend the dynamic range of the OPS by balancing its delay with the piezo-controlled position of a retro-reflecting mirror. The program reads the voltage off the OPS's controller and translates the retro-reflecting mirror appropriately to balance the OPS's voltage if it falls towards either end of its dynamic range.

The balancing routine is implemented in LabVIEW™ and the front panel and the block diagram are presented in Figure B.0.1 and Figure B.0.2

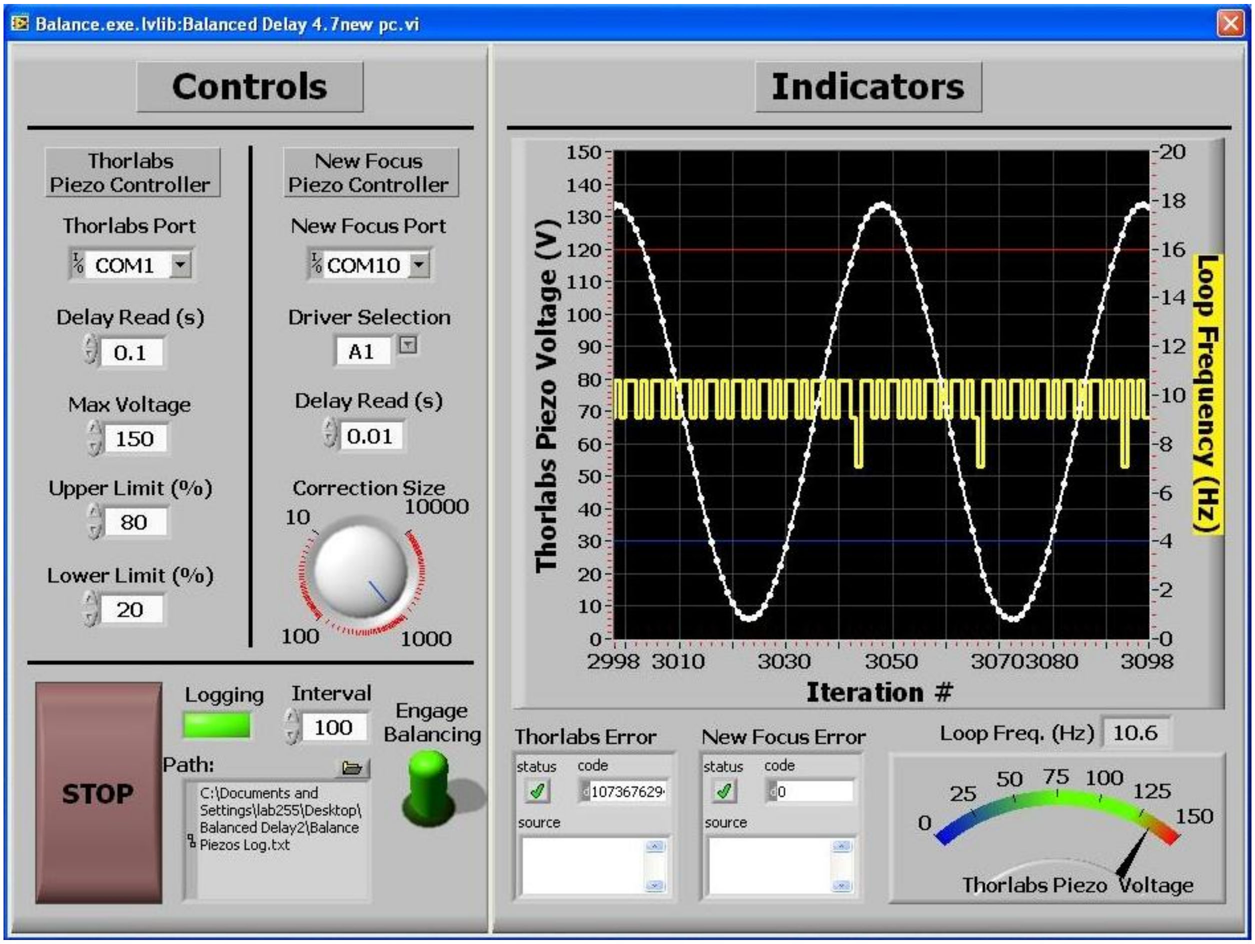
Balance.exe.lvlib:Balanced Delay 4.7new pc.vi

Thorlabs Port: COM1
Delay Read (s): 0.1
Max Voltage: 150
Upper Limit (%): 80
Lower Limit (%): 20
New Focus Port: COM10
Driver Selection: A1
Delay Read (s): 0.01
Interval: 100
Path: C:\Documents and Settings\lab255\Desktop\Balanced Delay2\Balance Piezos Log.txt
Thorlabs Error: status ✓ code 107367629
New Focus Error: status ✓ code 0
Loop Freq. (Hz): 10.6

Figure B.0.1: Front panel of balancing routine. For demonstrated purposed sinusoidal voltage is applied to the piezo driver of the OPS. The upper and lower limits of the dynamic range are user defined. The yellow trace is the refresh rate of the program in seconds.

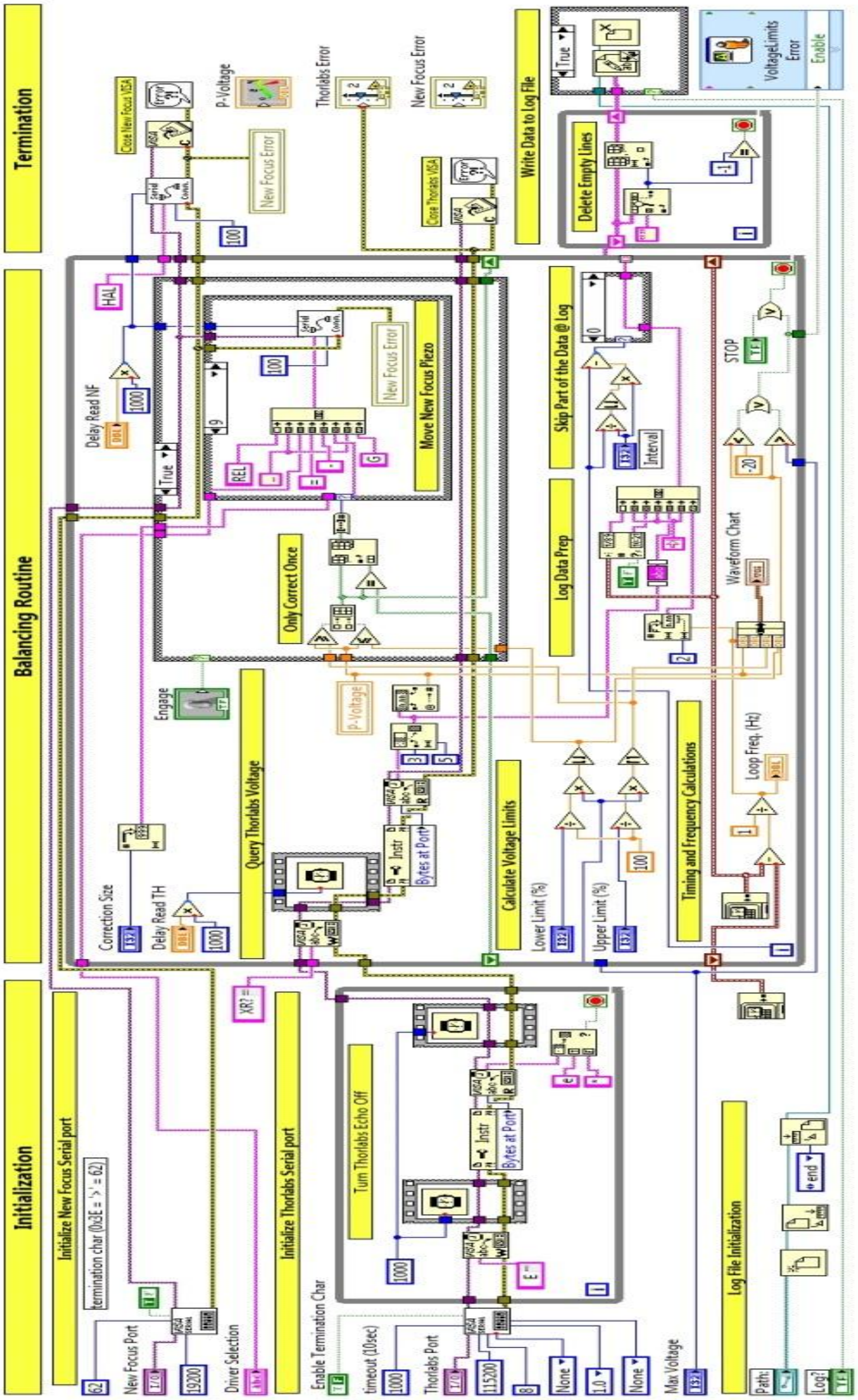

Figure B.0.2: Block diagram of the balancing routine.

APPENDIX C:

ADC CONSTRAINT CALCULATION & PLOTTING

In section 2.2.5 the constraints of ADC were presented as well as the equations that govern their behavior. Figure 2.8 and Figure 2.9 of section 2.2.5 were plotted using the MathCAD code that follows.

Photonic Analog-to-Digital Conversion Theoretical Limits

Based on: R. H. Walden, "Analog-to-digital converter survey and analysis," *Selected Areas in Communications, IEEE Journal on,* vol. 17, pp. 539-550, 1999.

H. Taylor, "An optical analog-to-digital converter--Design and analysis," *Quantum Electronics, IEEE Journal of,* vol. 15, pp. 210-216, 1979.

Created by Dimitrios Mandridis during Winter 2008-9
Ultrafast Photonics Group, CREOL: The college of
Optics and Photonics, University of Central Florida

Constants used throughout the program

V Full Scale is the full voltage swing of the ADC (a constant here) $\mathrm{Vfs} := 1$

fs is the sampling frequency in Hz (a variable here) $\mathrm{fstart} := 10\cdot 10^{6}$ $\mathrm{fstartlog} := \log(\mathrm{fstart})$ $\mathrm{fstop} := 10^{14}$ $\mathrm{fstoplog} := \log(\mathrm{fstop})$

Points per frequency decade: $\mathrm{points} := 20$ $i := 0, 1 .. (\mathrm{fstoplog} - \mathrm{fstartlog})\cdot\mathrm{points}$ $\mathrm{fs}_{i,0} := 10^{\left(\frac{i+\mathrm{fstartlog}\cdot\mathrm{points}}{\mathrm{points}}\right)}$

$\mathrm{Rresp} := 0.8$ $q := 1.602\cdot 10^{-19}$ $T := 300\,K$ $R := 50$ $\mathrm{hbar} := 1.056\cdot 10^{-34}$ $k := 1.3806503\cdot 10^{-23}$

A. Timing Jitter Error (Phase Noise)

$$\mathrm{Bjitter}(\mathrm{fs}, \tau j) := \log\left(\frac{2}{\sqrt{3}\cdot\pi\cdot\mathrm{fs}\cdot\tau j}, 2\right) - 1$$

Not dependent on Vfs

Find solution for 10bit system @ 10*GHz*

Given

$$\mathrm{Bjitter}\left(10^{10}, \tau j\right) = 10$$

$$\mathrm{Find}(\tau j) \rightarrow \frac{\sqrt{3}}{30720000000000\cdot\pi}$$

$$\frac{10^{15}}{10240000000000\cdot\pi} = 31.085\ \mathrm{fs}$$

$$\mathrm{Bjitter}\left(0.08\cdot 10^{9}, 8\cdot 10^{-15}\right) = 18.131$$

$$\mathrm{Bjitter}\left(2.56\cdot 10^{9}, 8\cdot 10^{-15}\right) = 13.131$$

B. Pulse Energy Error (AM Noise)

$$\mathrm{Benergy}(\mathrm{amp}, \mathrm{Vfs}) := \log\left(\frac{\mathrm{Vfs}}{\mathrm{amp}}, 2\right) - 1$$

Find solution for 10bit system @ 10*GHz*

Given

$$\mathrm{Benergy}(\mathrm{amp}, \mathrm{Vfs}) = 10$$

$$\mathrm{Find}(\mathrm{amp}) \rightarrow \frac{1}{2048}$$

$$\frac{1}{2048}\cdot 100 = 0.049\ \%$$

$$\mathrm{Benergy}(0.000125, 2) = 12.966$$

C. Pulse Duration Error

$$\mathrm{Bpulse}(fs, \tau p) := \log\left[\frac{12}{(\pi \cdot fs \cdot \tau p)^2}, 2\right] + 1$$

Not dependent on Vfs

$$\mathrm{Bpulse}\left(2.56 \cdot 10^{9}, 1.8 \cdot 10^{-12}\right) = 16.805$$

$$\mathrm{Bpulse}\left(0.08 \cdot 10^{9}, 1.8 \cdot 10^{-12}\right) = 26.805$$

Find solution for 10bit system @ 10*GHz*

Given

$$\mathrm{Bpulse}\left(10^{10}, \tau p\right) = 10$$

$$\mathrm{Find}(\tau p) \rightarrow \begin{pmatrix} -\frac{\sqrt{6}}{160000000000 \cdot \pi} & \frac{\sqrt{6}}{160000000000 \cdot \pi} \end{pmatrix}$$

$$\frac{\sqrt{6}}{160000000000 \cdot \pi} \cdot 10^{12} = 4.873 \quad \mathrm{ps}$$

D. Thermal Noise Floor

$$I(fs, T) := \int_0^{\frac{fs}{2}} \frac{4 \cdot \mathrm{hbar} \cdot \pi \cdot f}{\exp\left(\frac{4 \cdot \mathrm{hbar} \cdot \pi \cdot f}{k \cdot T}\right) - 1}\, df$$

This simplifies to [K * T * fsampling / 2] for f < 1THz at Room Temp

$$\mathrm{Bthermal}(fs, Vfs, T) := \log\left[\left(\frac{Vfs^2}{12 \cdot R \cdot I(fs, T)}\right)^{0.5}, 2\right] - 1$$

Simplified Expression for Low frequencies

$$\mathrm{Bthermal\_LowFreq}(fs, Vfs) := \log\left[\left(\frac{Vfs^2}{6 \cdot R \cdot k \cdot T \cdot fs}\right)^{0.5}, 2\right] - 1$$

Find solution for (10bit system) @ 10*GHz*

$$\mathrm{Bthermal}\left(10^{10}, Vfs, T\right) = 12.131 \quad \mathrm{bits}$$

D. Shot Noise

$$\mathrm{Bshot}(fs, Vfs) := \log\left[\left(\frac{Vfs}{6 \cdot R \cdot q \cdot fs}\right)^{0.5}, 2\right] - 1$$

Find solution for (10bit system) @ 10*GHz*

$$\mathrm{Bshot}\left(10^{10}, Vfs\right) = 9.494 \quad \mathrm{bits}$$

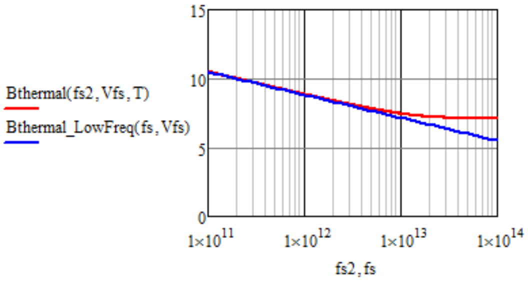

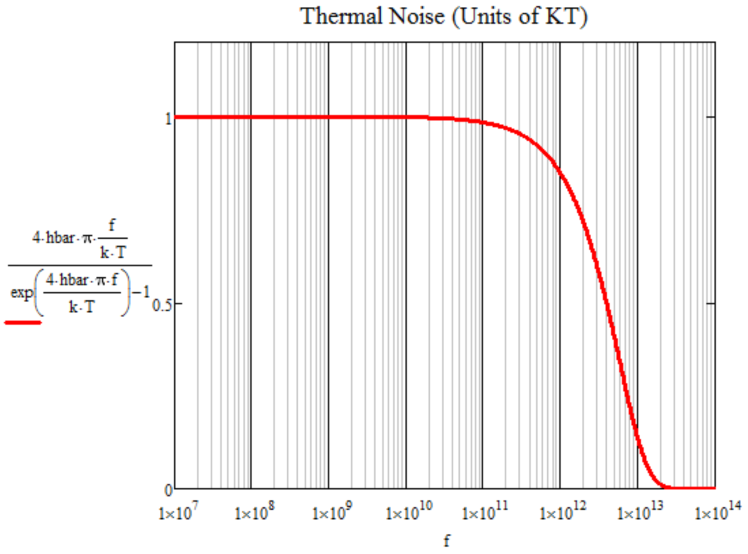

$$\mathrm{ThermalPower}(fs, T) := \frac{4\cdot hbar\cdot\pi\cdot\frac{fs}{k\cdot T}}{\exp\left(\frac{4\cdot hbar\cdot\pi\cdot fs}{k\cdot T}\right)-1}$$

Find frequency at which thermal noise becomes half

$f := 10^{12}$

$r9 := \mathrm{root}(\mathrm{ThermalPower}(f, T) - .5, f)$

$r9\cdot 10^{-12} = 3.922$ THz

Shot vs. Thermal Noise

$V := 0.001, 0.002 .. 10$

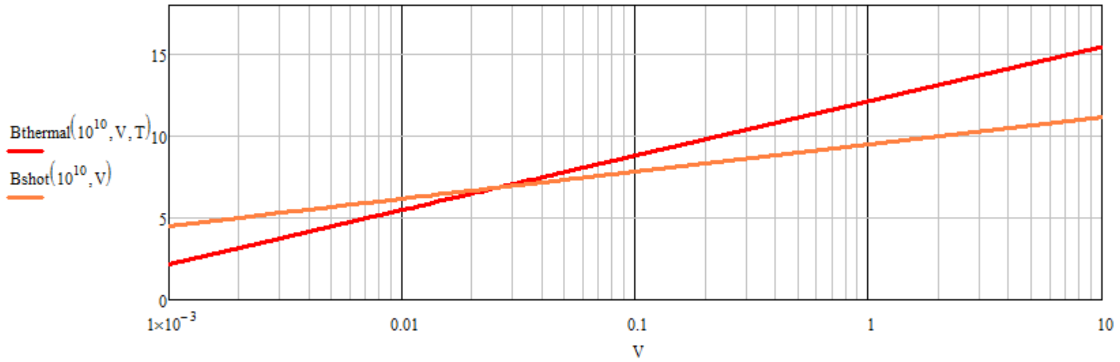

Find at which voltage the system becomes shot noise limited @ 10*GHz*

$f(x) := \mathrm{Bshot}(10^{10}, x) - \mathrm{Bthermal}(10^{10}, x, T)$

$V := .02$

$\mathrm{Vcross} := \mathrm{root}(f(V), V)$

$\mathrm{Vcross} = 0.026$ Volts

$\mathrm{Pel} := 10\cdot\log\left(\frac{\mathrm{Vcross}^2}{R}\right)$

$\mathrm{Popt} := \frac{\mathrm{Vcross}\cdot 10^3}{R\cdot\mathrm{Rresp}}$ $\mathrm{PoptLog} := 10\cdot\log(\mathrm{Popt})$

$\mathrm{Vcross} := \mathrm{root}(f(V), V)$

$\mathrm{Vcross} = 0.026$ Volts

$\mathrm{Pel} := 10 \cdot \log\left(\frac{\mathrm{Vcross}^2}{R}\right)$

$\mathrm{Pel} = -48.742$ dBm

$\mathrm{Popt} := \frac{\mathrm{Vcross} \cdot 10^3}{R \cdot \mathrm{Rresp}}$ $\mathrm{PoptLog} := 10 \cdot \log(\mathrm{Popt})$

$\mathrm{Popt} = 0.646$ mW $\mathrm{PoptLog} = -1.897$ dBm

E. Comparator Ambiguity

$\mathrm{Bambiguity}(fs, fT) := \left(\frac{\pi \cdot fT}{6.93 \cdot fs}\right) - 1.1$

Not dependent on Vfs

Find solution for 10bit system @ 10*GHz*

$g(x) := \mathrm{Bambiguity}\left(10^{10}, x\right) - 10$

$fT := 10^{11}$

$r1 := \mathrm{root}(g(fT), fT)$

$r1 \cdot 10^{-9} = 244.854$ GHz

F. Heisenberg Uncertainty

$\mathrm{Bheisen}(fs, Vfs) := \log\left(\frac{Vfs}{2 \cdot \sqrt{\mathrm{hbar} \cdot R \cdot fs}}, 2\right)$

Find solution for 10bit system @ 10*GHz*

$h(x) := \mathrm{Bheisen}\left(10^{10}, x\right) - 20$

$V := 2$

$r2 := \mathrm{root}(h(V), V)$

$r2 = 1.524$ Volts

	Full Span Voltage	AM Noise	Jitter	fT= 2.5/ππ/τreg	Pulse Duration	Temperature
Set those parameters for plotting	$Vfs := 2$	$amp := .001$	$\tau j := 20 \cdot 10^{-15}$	$fT := 250 \times 10^{9}$	$\tau p := 5 \cdot 10^{-12}$	$T := 300$

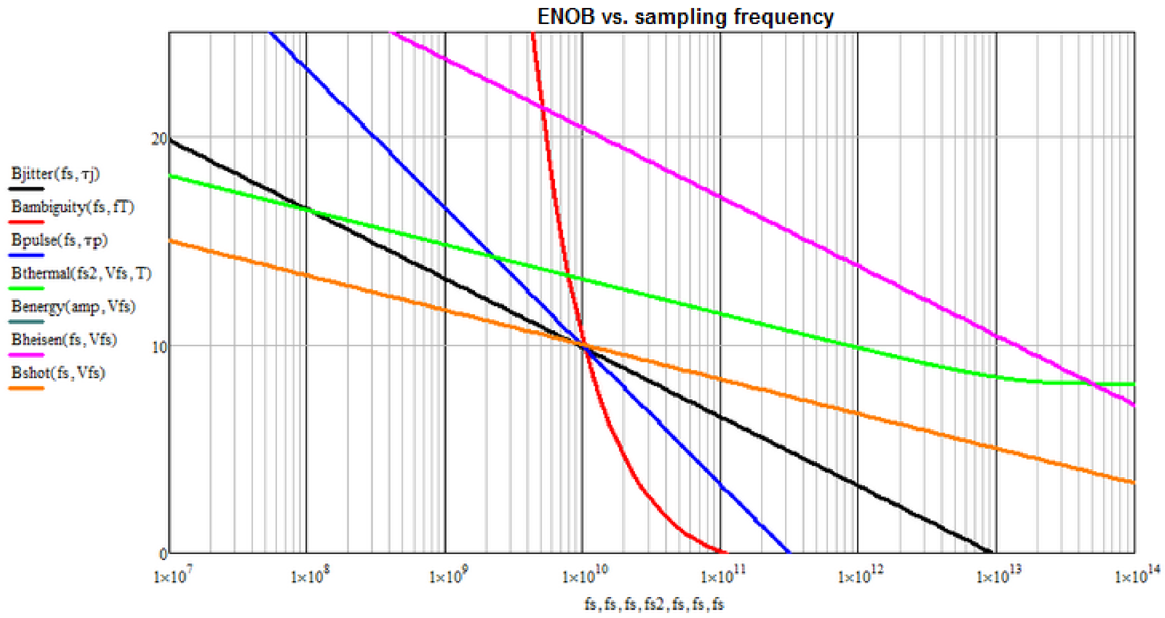

	Full Span Voltage	AM Noise	Jitter	fT= 2.5/ππ/τreg	Pulse Duration	Temperature
Set those parameters for plotting	$Vfs := 1$	$amp := .0005$	$\tau j := 25 \times 10^{-15}$	$fT := 600 \times 10^{9}$	$\tau p := 4 \cdot 10^{-12}$	$T := 300$

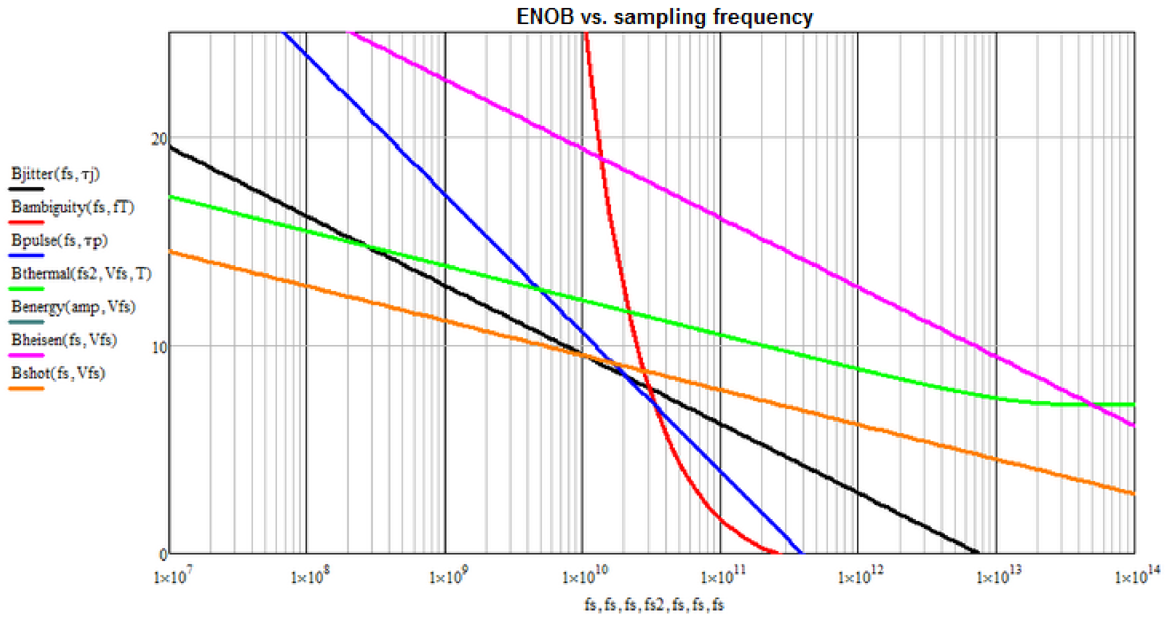

LIST OF REFERENCES

[1] B. H. Kolner, "Space-time duality and the theory of temporal imaging," *Quantum Electronics, IEEE Journal of,* vol. 30, pp. 1951-1963, 1994.

[2] P. J. Delfyett, L. T. Florez, N. Stoffel, T. Gmitter, N. C. Andreadakis, Y. Silberberg, J. P. Heritage, and G. A. Alphonse, "High-power ultrafast laser diodes," *Quantum Electronics, IEEE Journal of,* vol. 28, pp. 2203-2219, 1992.

[3] K. Goda, K. K. Tsia, and B. Jalali, "Serial time-encoded amplified imaging for real-time observation of fast dynamic phenomena," *Nature,* vol. 458, pp. 1145-1149, 2009.

[4] K. K. Tsia, K. Goda, D. Capewell, and B. Jalali, "Performance of serial time-encoded amplified microscope," *Opt. Express,* vol. 18, pp. 10016-10028, 2010.

[5] R. E. Saperstein, D. Panasenko, and Y. Fainman, "Demonstration of a microwave spectrum analyzer based on time-domain optical processing in fiber," *Opt. Lett.,* vol. 29, pp. 501-503, 2004.

[6] R. E. Saperstein and Y. Fainman, "Information processing with longitudinal spectral decomposition of ultrafast pulses," *Appl. Opt.,* vol. 47, pp. A21-A31, 2008.

[7] R. C. Youngquist, S. Carr, and D. E. N. Davies, "Optical coherence-domain reflectometry: a new optical evaluation technique," *Opt. Lett.,* vol. 12, pp. 158-160, 1987.

[8] K. Takada, I. Yokohama, K. Chida, and J. Noda, "New measurement system for fault location in optical waveguide devices based on an interferometric technique," *Appl. Opt.,* vol. 26, pp. 1603-1606, 1987.

[9] S. R. Chinn, E. A. Swanson, and J. G. Fujimoto, "Optical coherence tomography using a frequency-tunable optical source," *Opt. Lett.,* vol. 22, pp. 340-342, 1997.

[10] B. Golubovic, B. E. Bouma, G. J. Tearney, and J. G. Fujimoto, "Optical frequency-domain reflectometry using rapid wavelength tuning of a Cr4+:forsterite laser," *Opt. Lett.,* vol. 22, pp. 1704-1706, 1997.

[11] R. Huber, M. Wojtkowski, and J. G. Fujimoto, "Fourier Domain Mode Locking (FDML): A new laser operating regime and applications for optical coherence tomography," *Opt. Express,* vol. 14, pp. 3225-3237, 2006.

[12] S. T. Cundiff, W. H. Knox, and M. C. Nuss, "Active feed-forward channel equalisation for chirped pulse wavelength division multiplexing," *Electronics Letters,* vol. 33, pp. 10-11, 1997.

[13] D. Mandridis, I. Ozdur, and P. J. Delfyett, "An Electrooptic Feedforward System for Dynamic Control of a Quasi-Continuous-Wave Chirped Laser Source," *Photonics Technology Letters, IEEE,* vol. 21, pp. 1226-1228, Sep 1 2009.

[14] S. Yamashita and M. Asano, "Wide and fast wavelength-tunable mode-locked fiber laser based on dispersion tuning," *Opt. Express,* vol. 14, pp. 9299-9306, 2006.

[15] R. Huber, M. Wojtkowski, K. Taira, J. Fujimoto, and K. Hsu, "Amplified, frequency swept lasers for frequency domain reflectometry and OCT imaging: design and scaling principles," *Opt. Express,* vol. 13, pp. 3513-3528, 2005.

[16] T.-H. Tsai, C. Zhou, D. C. Adler, and J. G. Fujimoto, "Frequency comb swept lasers," *Opt. Express,* vol. 17, pp. 21257-21270, 2009.

[17] Y. Zhou, K. K. Y. Cheung, Q. Li, S. Yang, P. C. Chui, and K. K. Y. Wong, "Fast and wide tuning wavelength-swept source based on dispersion-tuned fiber optical parametric oscillator," *Opt. Lett.,* vol. 35, pp. 2427-2429, 2010.

[18] S. H. Yun, D. J. Richardson, and B. Y. Kim, "Interrogation of fiber grating sensor arrays with a wavelength-swept fiber laser," *Opt. Lett.,* vol. 23, pp. 843-845, 1998.

[19] K. Hsu, P. Meemon, K.-S. Lee, P. Delfyett, and J. Rolland, "Broadband Fourier-domain mode-locked lasers," *Photonic Sensors,* pp. 1-6, 2010.

[20] G. J. Tearney, B. E. Bouma, and J. G. Fujimoto, "High-speed phase- and group-delay scanning with a grating-based phase control delay line," *Opt. Lett.,* vol. 22, pp. 1811-1813, 1997.

[21] R. Huber, M. Wojtkowski, J. G. Fujimoto, J. Y. Jiang, and A. E. Cable, "Three-dimensional and C-mode OCT imaging with a compact, frequency swept laser source at 1300 nm," *Opt. Express,* vol. 13, pp. 10523-10538, 2005.

[22] Thorlabs. (February 2011). Available: http://www.thorlabs.com/

[23] S. H. Yun, C. Boudoux, G. J. Tearney, and B. E. Bouma, "High-speed wavelength-swept semiconductor laser with a polygon-scanner-based wavelength filter," *Opt. Lett.,* vol. 28, pp. 1981-1983, 2003.

[24] Micron Optics Inc. (February 2011). Available: http://www.micronoptics.com/fl_technology.php

[25] (2008, 22-10). *Analog signal*. Available: http://en.wikipedia.org/wiki/Analog_signal

[26] B. Shoop, *Photonic analog-to-digital conversion*. Berlin & New York: Springer, 2001.

[27] B. Razavi, *Principles of data conversion system design*. New York: IEEE Press, 1995.

[28] G. C. Valley, "Photonic analog-to-digital converters," *Opt. Express,* vol. 15, pp. 1955-1982, 2007.

[29] R. H. Walden, "Analog-to-digital converter survey and analysis," *IEEE J. Sel. Areas Commun.,* vol. 17, pp. 539-550, 1999.

[30] B. L. S. a. D. M. L. Pankaj K. Das, "High-Speed A/D Conversion Using a Photonic Implementation of an Error Diffusion Neural Network and Oversampling Techniques," in *IEEE Electro/Information Technology Conference*, Chicago.

[31] R. H. Walden, "Wiley Encyclopedia of Computer Science and Engineering," B. W. Wah, Ed., ed: Wiley-Interscience, John Wiley & Sons Inc,, 2008.

[32] M. Steyaert, J. H. Huijsing, and A. H. M. v. Roermund, *Analog circuit design : RF circuits : wide band, front-ends, DACs, design methodology and verification for RF and mixed-signal systems, low power and low voltage*. Netherlands;: Springer, 2005.

[33] E. N. Toughlian and H. Zmuda, "A photonic wide-band analog to digital converter," in *Microwave Photonics, 2000. MWP 2000. International Topical Meeting on*, 2000, pp. 248-250.

[34] H. Zmuda, E. N. Toughlian, G. Li, and P. LiKamWa, "A photonic wideband analog-to-digital converter," in *Aerospace Conference, 2001, IEEE Proceedings.*, 2001, pp. 3/1461-3/1472 vol.3.

[35] J. Stigwall and S. Galt, "Analysis of the resolution-bandwidth-noise trade-off in wavelength-based photonic analog-to-digital converters," *Appl. Opt.,* vol. 45, pp. 4310-4318, 2006.

[36] M. Johansson, B. Löfving, S. Hård, L. Thylén, M. Mokhtari, U. Westergren, and C. Pala, "Study of an Ultrafast Analog-to-Digital Conversion Scheme Based on Diffractive Optics," *Appl. Opt.,* vol. 39, pp. 2881-2887, 2000.

[37] H. F. Taylor, "An electrooptic analog-to-digital converter," *Proceedings of the IEEE,* vol. 63, pp. 1524-1525, 1975.

[38] H. F. Taylor, M. J. Taylor, and P. W. Bauer, "Electro-optic analog-to-digital conversion using channel waveguide modulators," *Applied Physics Letters,* vol. 32, pp. 559-561, 1978.

[39] T. R. Clark, Jr. and M. L. Dennis, "Toward a 100-Gsample/s photonic A-D converter," *Photonics Technology Letters, IEEE,* vol. 13, pp. 236-238, 2001.

[40] I. A. Goncharenko, A. K. Esman, V. K. Kuleshov, and V. A. Pilipovich, "Optical broadband analog-digital conversion on the base of microring resonator," *Optics Communications,* vol. 257, pp. 54-61, 2006.

[41] R. H. Walden, "Analog-to-digital converter survey and analysis," *Selected Areas in Communications, IEEE Journal on,* vol. 17, pp. 539-550, 1999.

[42] G. E. Betts, "Linearized modulator for suboctave-bandpass optical analog links," *Microwave Theory and Techniques, IEEE Transactions on,* vol. 42, pp. 2642-2649, 1994.

[43] J. A. Bell, M. C. Hamilton, D. A. Leep, T. D. Moran, H. F. Taylor, and Y. H. Lee, "Extension of electronic A/D converters to multi-gigahertz sampling rates using optical sampling and demultiplexing techniques," in *Signals, Systems and Computers, 1989. Twenty-Third Asilomar Conference on*, 1989, pp. 289-293.

[44] I. Nitta, J. Abeles, and P. J. Delfyett, "Hybrid Wavelength-Division and Optical Time-Division Multiplexed Multiwavelength Mode-Locked Semiconductor Laser," *Appl. Opt.,* vol. 39, pp. 6799-6805, 2000.

[45] H. Shi, I. Nitta, G. Alphonse, J. Connolly, and P. J. Delfyett, "Timing jitter performance of multiwavelength modelocked semiconductor laser," *Electronics Letters,* vol. 34, pp. 2250-2252, 1998.

[46] C. M. DePriest, T. Yilmaz, A. Braun, J. Abeles, and P. J. Delfyett, Jr., "High-quality photonic sampling streams from a semiconductor diode ring laser," *Quantum Electronics, IEEE Journal of,* vol. 38, pp. 380-389, 2002.

[47] P. J. Delfyett, C. DePriest, and T. Yilmaz, "Signal processing at the speed of lightwaves [photonic ADCs]," *Circuits and Devices Magazine, IEEE,* vol. 18, pp. 28-35, 2002.

[48] J. B. Johnson, "Thermal Agitation of Electricity in Conductors," *Physical Review,* vol. 32, p. 97, 1928.

[49] H. Nyquist, "Thermal Agitation of Electric Charge in Conductors," *Physical Review,* vol. 32, p. 110, 1928.

[50] E. W. Jacobs, J. B. Sobti, V. F. Vella, R. Nguyen, D. J. Albares, R. B. Olsen, C. T. Chang, S. K. Sun, M. J. Choe, S. Beccue, R. Yu, and J. P. A. van der Wagt, "Optically clocked track-and-hold for high-speed high-resolution analog-to-digital conversion," in *Microwave Photonics, 2004. MWP'04. 2004 IEEE International Topical Meeting on*, 2004, pp. 190-192.

[51] L. Y. Nathawad, R. Urata, B. A. Wooley, and D. A. B. Miller, "A 40-GHz-bandwidth, 4-bit, time-interleaved A/D converter using photoconductive sampling," *Solid-State Circuits, IEEE Journal of,* vol. 38, pp. 2021-2030, 2003.

[52] R. Urata, R. Takahashi, V. A. Sabnis, D. A. B. Miller, and J.S. Harris, Jr., "Ultrafast optoelectronic sample-and-hold using low-temperature-grown GaAs MSM," *Photonics Technology Letters, IEEE,* vol. 15, pp. 724-726, 2003.

[53] R. F. Pease, K. Ioakeimidi, R. Aldana, and R. Leheny, "Photoelectronic analog-to-digital conversion using miniature electron optics: Basic design considerations," *Journal of Vacuum Science & Technology B: Microelectronics and Nanometer Structures,* vol. 21, pp. 2826-2829, 2003.

[54] K. Ioakeimidi, R. F. Leheny, S. Gradinaru, P. R. Bolton, R. Aldana, M. Kai, J. E. Clendenin, J. S. Harris, Jr., and R. F. W. Pease, "Photoelectronic analog-to-digital conversion: sampling and

quantizing at 100 Gs/s," *Microwave Theory and Techniques, IEEE Transactions on,* vol. 53, pp. 336-342, 2005.

[55] A. S. Bhushan, F. Coppinger, and B. Jalali, "Time-stretched analogue-to-digital conversion," *Electronics Letters,* vol. 34, pp. 839-841, 1998.

[56] Y. Han and B. Jalali, "Photonic Time-Stretched Analog-to-Digital Converter: Fundamental Concepts and Practical Considerations," *J. Lightwave Technol.,* vol. 21, p. 3085, 2003.

[57] J. Chou, O. Boyraz, D. Solli, and B. Jalali, "Femtosecond real-time single-shot digitizer," *Applied Physics Letters,* vol. 91, pp. 161105-3, 2007.

[58] J. Chou, J. A. Conway, G. A. Sefler, G. C. Valley, and B. Jalali, "Photonic Bandwidth Compression Front End for Digital Oscilloscopes," *J. Lightwave Technol.,* vol. 27, pp. 5073-5077, 2009.

[59] D. Strickland and G. Mourou, "Compression of amplified chirped optical pulses," *Optics Communications,* vol. 56, pp. 219-221, 1985.

[60] S. Gee, G. Alphonse, J. Connolly, and P. J. Delfyett, "High-power mode-locked external cavity semiconductor laser using inverse bow-tie semiconductor optical amplifiers," *Selected Topics in Quantum Electronics, IEEE Journal of,* vol. 4, pp. 209-215, 1998.

[61] A. Mar, R. Helkey, J. Bowers, D. Mehuys, and D. Welch, "Mode-locked operation of a master oscillator power amplifier," *Photonics Technology Letters, IEEE,* vol. 6, pp. 1067-1069, 1994.

[62] L. Goldberg, D. Mehuys, and D. Welch, "High power mode-locked compound laser using a tapered semiconductor amplifier," *Photonics Technology Letters, IEEE,* vol. 6, pp. 1070-1072, 1994.

[63] K. Kim, S. Lee, and P. J. Delfyett, "eXtreme chirped pulse amplification-beyond the fundamental energy storage limit of semiconductor optical amplifiers," *Selected Topics in Quantum Electronics, IEEE Journal of,* vol. 12, pp. 245-254, 2006.

[64] K. Kim, S. Lee, and P. J. Delfyett, "1.4kW high peak power generation from an all semiconductor mode-locked master oscillator power amplifier system based on eXtreme Chirped Pulse Amplification(X-CPA)," *Optics Express,* vol. 13, pp. 4600-4606, Jun 13 2005.

[65] C. H. Lee and P. J. Delfyett, "Limits on amplification of picosecond pulses by using semiconductor laser traveling-wave amplifiers," *Quantum Electronics, IEEE Journal of,* vol. 27, pp. 1110-1114, 1991.

[66] G. P. Agrawal and N. A. Olsson, "Self-phase modulation and spectral broadening of optical pulses in semiconductor laser amplifiers," *Quantum Electronics, IEEE Journal of,* vol. 25, pp. 2297-2306, 1989.

[67] S. Lee, D. Mandridis, and P. J. Delfyett, "eXtreme Chirped Pulse Oscillator Operating in the Nanosecond Stretched Pulse Regime," *Opt. Express,* vol. 16, pp. 4766-4773, 2008.

[68] S. Lee, K. Kim, and P. J. Delfyett, "Extreme chirped pulse oscillator (XCPO) using a theta cavity design," *Photonics Technology Letters, IEEE,* vol. 18, pp. 799-801, 2006.

[69] J. N. Walpole, J. P. Donnelly, P. J. Taylor, L. J. Missaggia, C. T. Harris, R. J. Bailey, A. Napoleone, S. H. Groves, S. R. Chinn, R. Huang, and J. Plant, "Slab-coupled 1.3-μm semiconductor laser with single-spatial large-diameter mode," *Photonics Technology Letters, IEEE,* vol. 14, pp. 756-758, 2002.

[70] P. W. Juodawlkis, J. J. Plant, R. K. Huang, L. J. Missaggia, and J. P. Donnelly, "High-power 1.5-μm InGaAsP-InP slab-coupled optical waveguide amplifier," *Photonics Technology Letters, IEEE,* vol. 17, pp. 279-281, 2005.

[71] F. Rana, H. L. T. Lee, R. J. Ram, M. E. Grein, L. A. Jiang, E. P. Ippen, and H. A. Haus, "Characterization of the noise and correlations in harmonically mode-locked lasers," *J. Opt. Soc. Am. B,* vol. 19, pp. 2609-2621, 2002.

[72] S. Gee, F. Quinlan, S. Ozharar, and P. J. Delfyett, "Simultaneous optical comb frequency stabilization and super-mode noise suppression of harmonically mode-locked semiconductor ring laser using an intracavity etalon," *Photonics Technology Letters, IEEE,* vol. 17, pp. 199-201, 2005.

[73] I. Ozdur, M. Akbulut, N. Hoghooghi, D. Mandridis, S. Ozharar, F. Quinlan, and P. J. Delfyett, "A Semiconductor-Based 10-GHz Optical Comb Source With Sub 3-fs Shot-Noise-Limited Timing Jitter and ~500-Hz Comb Linewidth," *Photonics Technology Letters, IEEE,* vol. 22, pp. 431-433, 2010.

[74] T. W. Hansch and B. Couillaud, "Laser frequency stabilization by polarization spectroscopy of a reflecting reference cavity," *Optics Communications,* vol. 35, pp. 441-444, 1980.

[75] R. W. P. Drever, J. L. Hall, F. V. Kowalski, J. Hough, G. M. Ford, A. J. Munley, and H. Ward, "Laser phase and frequency stabilization using an optical resonator," *Applied Physics B: Lasers and Optics,* vol. 31, pp. 97-105, 1983.

[76] E. D. Black, "An introduction to Pound--Drever--Hall laser frequency stabilization," *American Journal of Physics,* vol. 69, pp. 79-87, 2001.

[77] M. Ostermeyer, T. Waltinger, and M. Gregor, "Frequency stabilization of a Q-switched Nd:YAG laser oscillator with stability better 300 kHz following an rf-sideband scheme," *Optics Communications,* vol. 282, pp. 3302-3307, 2009.

[78] D. Mandridis, I. Ozdur, M. Bagnell, and P. J. Delfyett, "Free spectral range measurement of a fiberized Fabry-Perot etalon with sub-Hz accuracy," *Optics Express,* vol. 18, pp. 11264-11269, May 24 2010.

[79] D. K. Armani, T. J. Kippenberg, S. M. Spillane, and K. J. Vahala, "Ultra-high-Q toroid microcavity on a chip," *Nature,* vol. 421, pp. 925-928, Feb 27 2003.

[80] B. C. Young, F. C. Cruz, W. M. Itano, and J. C. Bergquist, "Visible Lasers with Subhertz Linewidths," *Physical Review Letters,* vol. 82, p. 3799, 1999.

[81] J. Chen, J. W. Sickler, P. Fendel, E. P. Ippen, F. X. Kartner, T. Wilken, R. Holzwarth, and T. W. Hansch, "Generation of low-timing-jitter femtosecond pulse trains with 2 GHz repetition rate via external repetition rate multiplication," *Optics Letters,* vol. 33, pp. 959-961, May 1 2008.

[82] C. H. Li, A. J. Benedick, P. Fendel, A. G. Glenday, F. X. Kartner, D. F. Phillips, D. Sasselov, A. Szentgyorgyi, and R. L. Walsworth, "A laser frequency comb that enables radial velocity measurements with a precision of 1 cm s(-1)," *Nature,* vol. 452, pp. 610-612, Apr 3 2008.

[83] F. Quinlan, S. Ozharar, S. Gee, and P. J. Delfyett, "Harmonically mode-locked semiconductor-based lasers as high repetition rate ultralow noise pulse train and optical frequency comb sources," *Journal of Optics a-Pure and Applied Optics,* vol. 11, pp. -, Oct 2009.

[84] I. Ozdur, M. Akbulut, N. Hoghooghi, D. Mandridis, M. U. Piracha, and P. J. Delfyett, "Optoelectronic loop design with 1000 finesse Fabry-Perot etalon," *Optics Letters,* vol. 35, pp. 799-801, Mar 15 2010.

[85] Y. Honda, H. Shimizu, M. Fukuda, T. Omori, J. Urakawa, K. Sakaue, H. Sakai, and N. Sasao, "Stabilization of a non-planar optical cavity using its polarization property," *Optics Communications,* vol. 282, pp. 3108-3112, Aug 1 2009.

[86] D. A. Shaddock, M. B. Gray, and D. E. McClelland, "Frequency locking a laser to an optical cavity by use of spatial mode interference," *Optics Letters,* vol. 24, pp. 1499-1501, Nov 1 1999.

[87] R. W. P. Drever, J. L. Hall, F. V. Kowalski, J. Hough, G. M. Ford, A. J. Munley, and H. Ward, "Laser Phase and Frequency Stabilization Using an Optical-Resonator," *Applied Physics B-Photophysics and Laser Chemistry,* vol. 31, pp. 97-105, 1983.

[88] E. D. Black, "An introduction to Pound-Drever-Hall laser frequency stabilization," *American Journal of Physics,* vol. 69, pp. 79-87, Jan 2001.

[89] C. R. Locke, D. Stuart, E. N. Ivanov, and A. N. Luiten, "A simple technique for accurate and complete characterisation of a Fabry-Perot cavity," *Optics Express,* vol. 17, pp. 21935-21943, Nov 23 2009.

[90] Y. Yeh, D. Park, and S. H. Park, "High-speed measurement of free spectral range voltage of tunable filters," *Optics Letters,* vol. 34, pp. 52-54, Jan 1 2009.

[91] S. Gee, S. Ozharar, F. Quinlan, and P. J. Delfyett, "High-precision measurement of free spectral range of etalon," *Electronics Letters,* vol. 42, pp. 715-716, 2006.

[92] M. Y. Frankel and R. D. Esman, "Optical single-sideband suppressed-carrier modulator for wide-band signal processing," *Journal of Lightwave Technology,* vol. 16, pp. 859-863, May 1998.

[93] P. J. Delfyett, S. Gee, C. Myoung-Taek, H. Izadpanah, L. Wangkuen, S. Ozharar, F. Quinlan, and T. Yilmaz, "Optical frequency combs from semiconductor lasers and applications in ultrawideband signal processing and communications," *Lightwave Technology, Journal of,* vol. 24, pp. 2701-2719, 2006.

[94] F. Quinlan, S. Ozharar, S. Gee, and P. J. Delfyett, "Harmonically mode-locked semiconductor-based lasers as high repetition rate ultralow noise pulse train and optical frequency comb sources," *Journal of Optics A: Pure and Applied Optics,* vol. 11, p. 103001, 2009.

[95] P. W. Juodawlkis, J. C. Twichell, G. E. Betts, J. J. Hargreaves, R. D. Younger, J. L. Wasserman, F. J. O'Donnell, K. G. Ray, and R. C. Williamson, "Optically sampled analog-to-digital converters," *Microwave Theory and Techniques, IEEE Transactions on,* vol. 49, pp. 1840-1853, 2001.

[96] N. Storkfelt, B. Mikkelsen, D. S. Olesen, M. Yamaguchi, and K. E. Stubkjaer, "Measurement of carrier lifetime and linewidth enhancement factor for 1.5- mu m ridge-waveguide laser amplifier," *Photonics Technology Letters, IEEE,* vol. 3, pp. 632-634, 1991.

[97] A. E. Siegman, *Lasers*. Mill Valley, CA: University Science, 1986.

[98] T. R. Clark, J. U. Kang, and R. D. Esman, "Performance of a time- and wavelength-interleaved photonic sampler for analog-digital conversion," *Photonics Technology Letters, IEEE,* vol. 11, pp. 1168-1170, 1999.

[99] S. Gee, S. Ozharar, J. J. Plant, P. W. Juodawlkis, and P. J. Delfyett, "Intracavity dispersion effect on timing jitter of ultralow noise mode-locked semiconductor based external-cavity laser," *Optics Letters,* vol. 34, p. 238, February 1, 2009 2009.

[100] D. von der Linde, "Characterization of the noise in continuously operating mode-locked lasers," *Applied Physics B: Lasers and Optics,* vol. 39, pp. 201-217, 1986.

[101] V. Hansen, F. Beuker, and Goethe-Museum Düsseldorf Anton-und-Katharina-Kippenberg-Stiftung., *Europäische Zeichnungen zur Zeit Goethes : Katalog der Ausstellung im Goethe-Museum Düsseldorf*. Düsseldorf: Goethe-Museum Düsseldorf, 2005.

[102] P. W. Juodawlkis and J. J. Plant, "Gain-Power Trade-Off in Low-Confinement Semiconductor Optical Amplifiers," in *Numerical Simulation of Optoelectronic Devices, 2007. NUSOD '07. International Conference on*, 2007, pp. 97-98.

[103] E. Treacy, "Optical pulse compression with diffraction gratings," *Quantum Electronics, IEEE Journal of,* vol. 5, pp. 454-458, 1969.

[104] S. Gee, E. Quinlan, S. Ozharar, P. J. Delfyett, J. J. Plant, and P. W. Juodawlkis, "Ultralow-noise mode-locked optical pulse trains from an external cavity laser based on a slab coupled optical waveguide amplifier (SCOWA)," *Optics Letters,* vol. 30, pp. 2742-2744, Oct 15 2005.

[105] I. Ozdur, S. Ozharar, F. Quinlan, D. Mandridis, and P. J. Delfyett, "An Interferometric Method for High Extinction Ratio Measurements With 60-dB Dynamic Range," *Ieee Photonics Technology Letters,* vol. 20, pp. 2075-2077, Nov-Dec 2008.

[106] S. Gupta and B. Jalali, "Time-warp correction and calibration in photonic time-stretch analog-to-digital converter," *Opt. Lett.,* vol. 33, pp. 2674-2676, 2008.

[107] M. U. Piracha, D. Nguyen, D. Mandridis, T. Yilmaz, I. Ozdur, S. Ozharar, and P. J. Delfyett, "Range resolved lidar for long distance ranging with sub-millimeter resolution," *Optics Express,* vol. 18, pp. 7184-7189, Mar 29 2010.

[108] C. E. Shannon, "A mathematical theory of communication," *Bell Syst. Tech. J.,* vol. 27, pp. 379-423, 623-656, 1948.

[109] F. Quinlan, S. Gee, S. Ozharar, and P. J. Delfyett, "Ultralow-jitter and -amplitude-noise semiconductor-based actively mode-locked laser," *Optics Letters,* vol. 31, p. 2870, 2006.

[110] S. Lee, D. Mandridis, and P. J. Delfyett, "eXtreme Chirped Pulse Oscillator Operating in the Nanosecond Stretched Pulse Regime," *Optics Express,* vol. 16, p. 4766, March 31, 2008 2008.

[111] A. Kippenberg and F. Michael, *Anton Kippenberg zum hundertsten Geburtstag*, 1. Aufl. ed. Frankfurt (am Main): Insel-Verlag, 1973.

[112] J. E. Malowicki, M. L. Fanto, M. J. Hayduk, and P. J. Delfyett, "Harmonically mode-locked glass waveguide laser with 21-fs timing jitter," *Ieee Photonics Technology Letters,* vol. 17, pp. 40-42, Jan 2005.

[113] R. Trebino, *Frequency-Resolved Optical Gating: The Measurement of Ultrashort Laser Pulses*, 1 edition (August 1, 2002) ed.: Springer, 2002.